学位論文

Generation mechanism of flickering aurora

（フリッカリングオーロラの発生メカニズム）

平成 28 年 10 月　博士（理学）申請

東京大学大学院理学系研究科

地球惑星科学専攻

福田　陽子

Generation mechanism of flickering aurora

Yoko Fukuda

FOR THE DEGREE OF DOCTOR OF PHILOSOPHY

October 2016

Department of Earth and Planetary Science

Graduate School of Science

The University of Tokyo

Acknowledgements

My time as a PhD student were very special, although I had various challenges, because there are many people to whom I am deeply grateful. During this six-year period, including a two-year absence from university for participation in JARE (Japanese Antarctic Research Expedition) 54, I had three respected supervisors: Dr. Ryuho Kataoka of National Institute of Polar Research (NIPR), Prof. Kanako Seki and Prof. Naomoto Iwagami of the University of Tokyo (UTokyo).

I owe a deep debt of gratitude to Dr. Ryuho Kataoka who willingly provided me with guidance at NIPR. He taught me many techniques for data analysis and observation and gave adequate time to discuss problems, constructive advice, and new ideas that I had never previously considered. If I had not met him, this thesis would not exist. I could learn a great deal from him, since he has always tried new things and comprehensively enjoyed science. Since he also gave me so many wonderful opportunities, I could spend memorable times at NIPR.

I would like to thank Prof. Kanako Seki, who provided direction during the most important final year of a doctoral program at university. She always provided me with theoretical considerations and down-to-earth advices based on her deep insight. She also constantly encouraged me in weekly meetings.

I want to express my greatest appreciation to Prof. Naomoto Iwagami, who willingly joined in the discussions, and always made pithy comments even though he was already retired. He always taught me the importance of valuable studies and achievements. My only regret is that I could not graduate before his retirement.

I would like to express my gratitude to Dr. Yoshizumi Miyoshi of Nagoya University, who made time for constructive discussions about wave-particle interaction, as well as useful suggestions on analyses. His technical supports and observational works also enabled the cooperative observations.

I am very grateful to Dr. Yusuke Ebihara of Kyoto University for developing the basic observational system. I also wish to thank Dr. Koji Nishimura of NIPR and Ms. Risa Suzuki of Japan Science Foundation, who provided technical assistance by fabricating the GPS and trigger circuit.

Prof. Kazuo Shiokawa of Nagoya University, Dr. Yuto Katoh of Tohoku University, and Dr. Takanori Nishiyama of NIPR provided me with incisive comments and concrete suggestions on the results of this thesis. I am also grateful to Dr. Masayuki Tanaka of Tokyo Institute of Technology and Dr. Atsushi Yamashita of UTokyo, who taught me about a machine learning technique from scratch and gave me behind-the-scenes support for an auroral auto-detection system.

I want to thank Dr. Donald Hampton of the University of Alaska Fairbanks for permission to use the observational site of the Poker Plat Research Range, as well as for his assistance with technical problems. He also provided all-sky data and meridian spectrograph data from this site for complementary results. I would like to express my deepest appreciation to Dr. Daniel Whiter and Dr. Hanna Dahlgren of the University of Southampton, who provided a new idea and technique, and enthusiastically enjoyed and encouraged my thesis.

I want to thank all of my friends who have been engaged in polar science over the last several years. They always made college life pleasant, and frequently gave me sweets. The enjoyable times that I shared with them were important in assisting me to complete this thesis. Finally, I would also like to express my gratitude to my parents for their moral and financial support over a long period. Their understanding has encouraged me, and this thesis could not have been achieved without it.

Yoko Fukuda

Abstract

At the altitude of the ionosphere, the brightest auroral phenomena are driven by a substorm triggered in the Earth's magnetosphere through field-aligned currents. The spatiotemporal auroral variation reflects not only the magnetospheric disturbance but also dynamic physical processes at the magnetosphere and ionosphere (M-I) coupling region. Auroras formed at the M-I coupling region are characterized by fine-scale structures on the order of a few kilometers, and it is often suggested that dispersive Alfvén waves (DAWs) play an important role in the formation mechanism. Flickering auroras, which are known to have the fastest temporal variation among the auroral phenomena, may be generated by electromagnetic ion cyclotron (EMIC) waves, which are one type of DAWs, and they often appear before or during the auroral breakup. Open questions about flickering auroras are a upper limit of the flickering frequency and what conditions are needed to form flickering auroras. This thesis has the purpose of answering these questions by determining their generation mechanisms using high-speed fine-scale imaging observations.

First, we designed a continuous observational system with a high spatiotemporal resolution, which was automatically controlled by a real-time auroral auto-detection system based on a machine learning technique. It was found that the accuracy of the auroral auto-detection was approximately 80% by comparison with the results judged by auto-detection and eye. It was also found that the amount of data was decreased by 75% using the auroral auto-detection system. We were finally able to obtain a continuous observational system with a spatial resolution of ~50 m at the 100 km altitude and a temporal resolution of 320 frames per second (fps) over three winter seasons.

In order to clarify the necessary conditions for flickering auroras, we statistically investigated the basic property of flickering auroras using the automatic detection of flickering auroras. It is found that the occurrence rate is basically proportional to the background non-flickering auroral intensity and that the bright auroras without the flickering modulation occasionally appears as the isolated arc. These results indicate that it is hard to excite EMIC waves within a weak and narrow acceleration region. It is also found that the flickering frequency is narrowband and has no correlation with the background auroral intensity and the substorm phase. These signatures suggest that the flickering aurora occurs at the low-altitude acceleration region. This result shows that the low-altitude acceleration region would play an important role in the excitation of EIMC waves. For the first time, it was also found that the flickering amplitude (%) decreases with the background non-flickering intensity. This variation would be formed by the difference between the electron velocity determined by the parallel potential drop and the phase velocity of EMIC waves.

We also found the first evidence that flickering auroras may be modulated by H^+-band EMIC waves, based on 160 fps optical observations. The fastest flickering aurora of 40–80 Hz transiently coexisted with the typical 10 Hz flickering as a result of O^+-band EMIC waves within the brightest aurora around the magnetic zenith. This result is strong evidence that flickering auroras are generated by multi-ion EMIC waves.

As an application of the high-speed imaging observations, we focused on the rapidly moving features of the pulsating aurora. A pulsating aurora has modulations of a few hertz embedded in the main pulsation. During a pulsation ON-phase, repetitive expansions are often observed around the edges of pulsating patches. Approximately 80% of all the deduced expansion speeds were less than 70 km s^{-1} at ionospheric altitudes, which is less than the projected Alfvén speed from the magnetospheric equator to the ionosphere. The rapid motions with speeds of tens of kilometers per second are unlikely to be explained by obliquely propagating chorus elements, which are known to cause 3 Hz modulation, because the perpendicular speed of the oblique chorus waves is faster than the Alfvén speed. One of candidates to generate the rapid spatial motions is the slow-mode Alfvén wave.

Our high-speed fine-scale imaging observation is helpful to visualize wave-particle interactions and to monitor plasma environments in the M-I coupling region.

Contents

Acknowledgements i

Contents v

1 Introduction 1

1.1 Large-Scale Auroral Activity: Auroral Substorm 1
1.2 Earth's Ionosphere 6
1.3 Type of Aurora 8
1.4 Acceleration Mechanisms of Discrete Aurora 9
1.4.1 Quasi-static Acceleration 9
1.4.2 Alfvénic Acceleration 13
1.5 Flickering Aurora 19
1.5.1 General Property 19
1.5.2 Generation Model 19
1.5.3 Recent Observations 26
1.6 Purpose 29

2 Observations 33

2.1 Instrumentation 33
2.1.1 sCMOS Camera 33
2.1.2 Calibration 34
2.1.3 Optical Filter 39
2.2 Observational System 40
2.2.1 First Winter Season (February 2014–April 2014) 42

2.2.2 Second Winter Season (November 2014–April 2015) 43

2.2.3 Third Winter Season (January 2015–April 2015) 45

2.3 Auroral Auto-detection System 48

2.3.1 System Overview 48

2.3.2 Performance Evaluation....................51

2.3.3 Possibility of Auroral Auto-detection....................52

3 Basic Property of Flickering Aurora 55

3.1 Occurrence Property....................55

3.1.1 Analysis 55

3.1.2 Observations 60

3.2 Flickering Amplitude 78

3.2.1 Observations 78

3.3 Discussion and Conclusions 81

4 Fastest Flickering Aurora 85

4.1 Method of Analysis....................85

4.2 Observational Results....................87

4.2.1 Event Description....................87

4.2.2 Spatiotemporal Variations 89

4.3 Discussion....................95

4.4 Conclusions 101

5 Application of High-speed Imaging Observations....................103

5.1 Introduction 103

5.2 Observations 104

5.3 Discussion....................111

5.4 Conclusions 115

6 General Discussion 117
7 General Conclusions..123
7.1 Summary of this thesis 123
7.2 Future Work..124

Appendix: EMIC wave in Multicomponent Plasma 127

References 133

1 Introduction

The subject of this thesis is auroras. This phenomenon is not only marvelously beautiful, but also a scientifically interesting phenomenon which is visible on Earth. Long ago, some believed that auroras were omens of disasters, or signs from deceased relatives or of war. As comprehension of the Earth and space sciences progressed, the aurora became an exciting research topic for scientists. In this chapter, a general introduction to the aurora and related phenomena in the Earth's magnetosphere and ionosphere system are presented.

1.1 Large-Scale Auroral Activity: Auroral Substorm

One of the most important breakthroughs in understanding auroral phenomena is a model of large-scale auroral oval activity, a so-called auroral substorm, first established by *Akasofu* [1964]. Although the characteristic features of auroral displays are dependent on the local time and magnetic latitudes, the time sequences of the auroral features over the entire polar cap were investigated using globally distributed ground-based observations. The lifetime of each auroral substorm is 1–3 hours and is divided into three phases depending on the time sequence: the quiet phase, expansive phase, and recovery phase. **Figure 1.1** shows the development of the auroral substorm at each stage. The quiet phase (T = 0 min) starts from quiet arcs elongated in the east-west direction. The expansive phase follows, with the sudden brightening of the quiet arcs from 0–5 min, and the arcs rapidly moves in the poleward direction. Because of the bulge expansion in the midnight sector, folds are formed in the evening sector and rapidly move westward within 10–30 min, which is called a westward traveling surge. At this stage, cloud-like patches appear and drift westward or eastward in the evening sector or the morning sector, respectively. The recovery phase starts with the equatorward motion of the arc within 30 min to 1 hour. In the morning sector, the patches spread extensively and drift eastward. After the reestablishment and the equatorward motion of the faint auroral arcs, the auroral oval activity returns to the quiet phase.

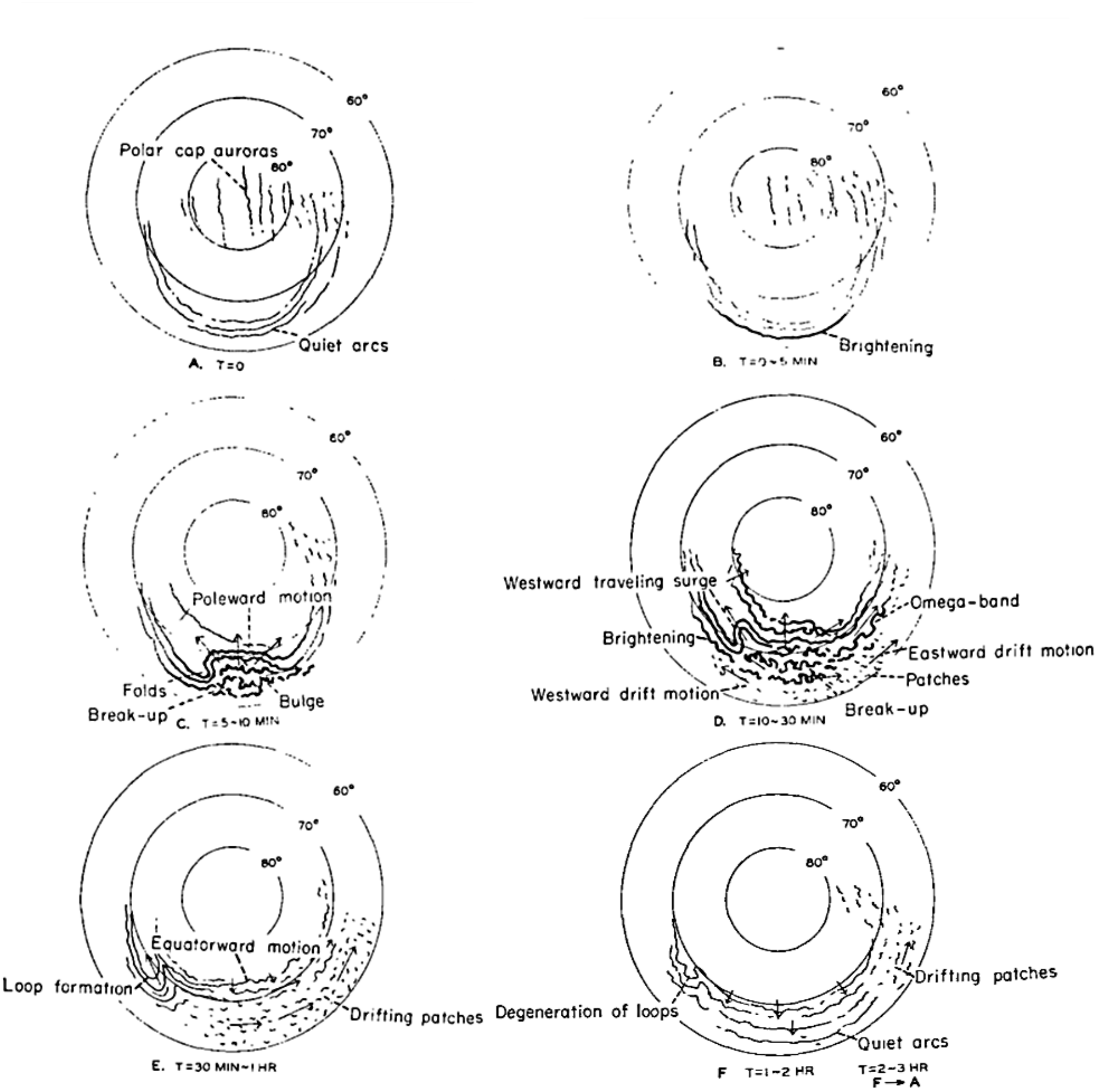

Figure 1.1: Schematic of the development of the auroral substorm (From *Akasofu* [1964]).

In order to understand the development processes of the auroral substorm, what triggers the substorm and how the magnetospheric structure changes during the substorm need to be resolved. The most crucial problems are the generation mechanism of the quiet arc and the initial brightening of the arc before and at the substorm onset in terms of a discontinuous phenomenon in the Earth's magnetosphere and ionosphere system. Convection of the magnetospheric plasmas has been recognized to play an important role in understanding the substorm. The most traditional model was proposed by *Dungey* [1961] who introduced magnetic reconnections to drive the magnetospheric convection, as shown in the left panel of **Figure 1.2**. When interplanetary magnetic fields (IMF) have a southward component, the energy of the solar wind, which is an origin of auroral particles, is thought to be stored by the magnetic reconnection at the dayside magnetopause. After the reconnection, the injected solar wind is dragged toward the midnight sector by flowing open field lines connected with the IMF under a "frozen-in" condition. This process forms a tail lobe region, which extends from the polar cap for hundreds of R_e (Earth radius, $1R_e$ = 6370 km) tailwards and has antiparallel open magnetic fields on the boundary of the plasma sheet region. With the thinning of the plasma sheet, the magnetic reconnection occurs around -20 R_e, at the so-called near earth neutral line (NENL), and enhances the plasma convection. The reversal convection toward the Earth caused by the reconnection flows toward both the dawn and dusk sides. By assuming the frozen-in condition, we see that plasma flows in the northern ionosphere are driven by the magnetospheric convection and result in a two-cell convection pattern as illustrated in the right panel of **Figure 1.2**. **Figure 1.3** indicates the magnetospheric structure and the sub structures mentioned above, which are divided by some boundaries.

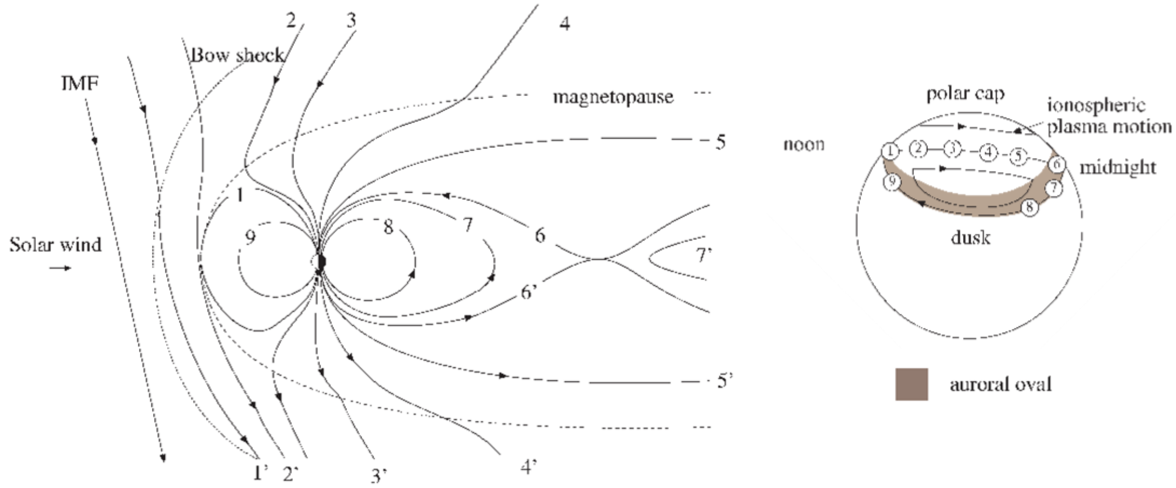

Figure 1.2: An illustration of the Dungey model for the convection pattern of the geomagnetic field lines connected to the IMF (left) by magnetic reconnections. The convection is carried by the field lines in the order indicated by the numbers. Ionospheric plasma motions driven by the convection are called two-cell convection (right) (From *Kivelson and Russell* [1995]).

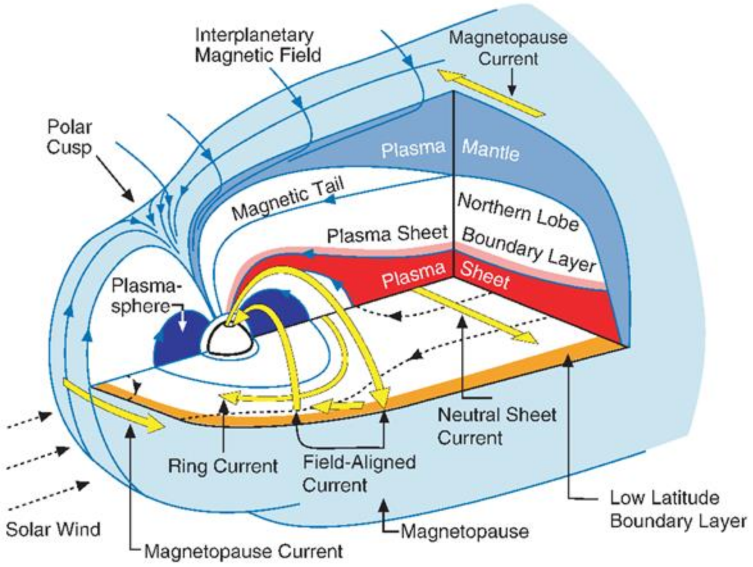

Figure 1.3: An illustration of the three-dimensional cross-section diagram of the magnetosphere representing magnetic field lines, plasma regions, and current systems (From *Kivelson and Russell* [1995]).

If the ionospheric convection exists, field-aligned currents (FACs), which are coupled to the magnetosphere, are necessary according to a conservation law for steady currents. *Iijima and Potemra* [1976] revealed spatial distributions of the large-scale FACs by statistical analyses of magnetometer observations obtained from a low-latitude satellite, as shown in **Figure 1.4**. The FAC system is traditionally divided into two groups: region 1 currents mostly connected to the magnetospheric boundaries, and region 2 currents closed in the inner magnetosphere. The high-latitude region 1 currents flow into the ionosphere in the morning sector and flow out from the ionosphere in the evening sector. The low-latitude region 2 currents flow in the opposite direction of the region 1 currents in each sector. Since the main dissipation region in the magnetosphere-ionosphere (M-I) coupling system is the ionosphere, the FAC plays an important role as a carrier of energy. Therefore, it is important to elucidate the processes which drive the FAC system.

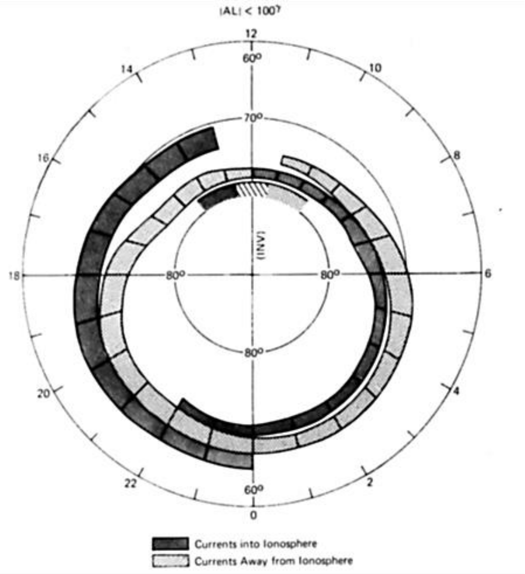

Figure 1.4: Distributions and flow directions of large-scale field-aligned currents in the northern high-latitude region during weakly disturbed conditions (From *Iijima and Potemra* [1976]).

The Dungey model is plausible only when the electric field of the ionosphere, which is projected from the magnetosphere along the magnetic field, is thought to be equipotential. However, it is becoming clear that many observational results and simulation studies conflict with the model. *Tanaka et al.* [2010] showed that a global M-I coupling simulation reproduced the primary observed signatures of the 3-D substorm structure and clarified the dynamical mechanisms. **Figure 1.5** shows magnetohydrodynamics (MHD) simulation results for energy conversions in the convection flow system during the expansion phase of the substorm; the separate panels show work done by the flow motional energy (E_v), electromagnetic energy (E_b), thermal energy (E_p), and convection flow ($-V_x$). This figure indicates that there are two dynamos ($J{\cdot}E < 0$) driven by the enhanced pressure at the cusp-mantle region and inside the plasma sheet. It was also found that the region 1 FAC connects to the cusp-mantle dynamo and the region 2 FAC connects to the plasma sheet dynamo by current line tracing, and that all of the FACs are driven by magnetizing currents (grad P currents). The simulation study also provides new insight indicating that the substorm represents the development and transition of the convection system, rather than extraordinary plasma processes in the magnetosphere such as reconnection or instability.

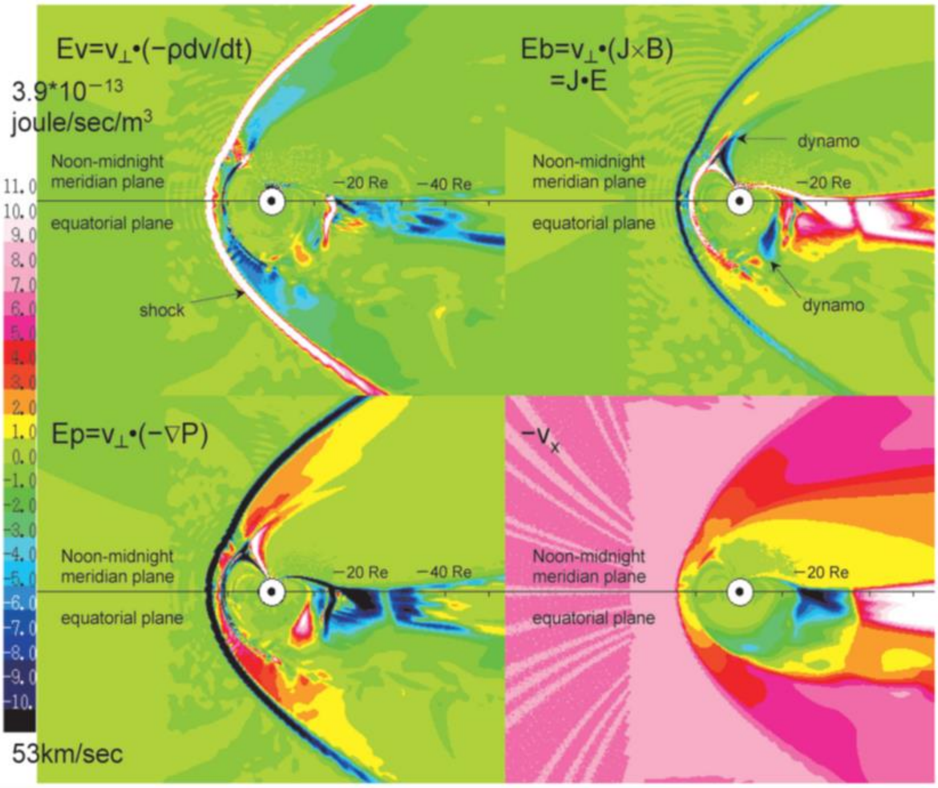

Figure 1.5: Simulation result for energy conversion in the convection systems (-V_x) during the expansion phase of the substorm. Three panels show work done by the flow motional energy (E_v), electromagnetic energy (E_b), and thermal energy (E_p). In each panel, the upper half shows the noon-midnight meridian plane, and the lower half shows the equatorial plane (From *Tanaka* [2014]).

It is worth noting that the global simulation is an extremely useful method to investigate the formation mechanisms of macroscale- and mesoscale- auroral phenomena (> tens of kilometers in scale) in the M-I coupling system, such as the quiet arc, initial brightening, and the westward traveling surge [*Ebihara et al.*, 2015a; 2015b; 2016]. Studies of fast and microscale auroral morphologies with less than a few kilometers in scale are beyond the scope of the global simulations. A valuable way to seek microscale auroral structure is via ground-based observation using imaging devices with a high spatiotemporal resolution.

1.2 Earth's Ionosphere

Before showing detailed auroral phenomena, such as the auroral type or the acceleration mechanisms, an introduction to the Earth's ionosphere is given in this section. Auroral phenomena occur when an accelerated electron is injected into the Earth's upper atmosphere and excites the atmospheric molecules or atoms. Almost all auroral light consists of emission lines and bands of neutral or ionized N_2, O, O_2, and N. **Figure 1.6** shows number density profiles of the neutral species and electrons for the day (solid) and night (dashed). Although O has the largest number density in the gas above about 200 km, O_2 overtakes it near 110 km in altitude. Below and near 100 km in altitude, N_2 and O_2 are dominant.

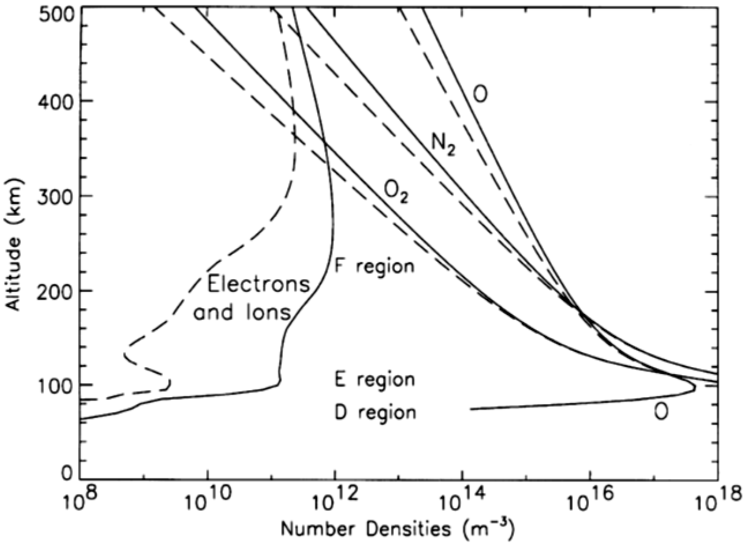

Figure 1.6: Typical density profile of the neutral species and the electrons for both day (solid) and night (dashed) for medium solar activity and low magnetic activity, calculated from the 1990 International Reference Ionosphere and the MSISE-90 neutral-density model (From *Richmond and Lu* [2000]).

The auroral emission occurs approximately at an altitude between 80 km and 500 km; the altitude depends on the energy of the electrons injected into the ionosphere. The typical electron energy that occurs the aurora ranges from a few hundred eV to tens of keV. The electrons effectively ionize the atmospheric molecules or atoms at a stopping height dependent on the electron energy as shown in **Figure 1.7**.

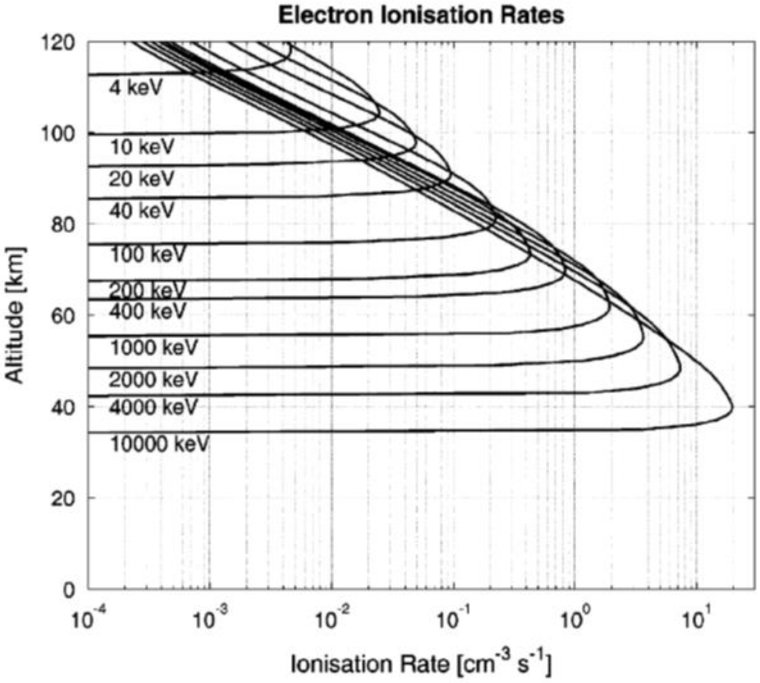

Figure 1.7: Ionization rate by electrons with various energies when the electron number flux is 100 cm^{-2} s^{-1} sr^{-1} (From *Turunen et al.* [2009]).

1.3 Type of Aurora

The auroras significantly change their shape and intensity depending on the phase of the auroral substorm and the magnetic local time, as shown in **Figure 1.1**. They are mainly divided into two categories, discrete auroras and diffuse auroras, based on their different auroral intensities, structures, and formation processes.

The discrete aurora is often visible to the naked eye and has various discrete forms depending on the relative distances between the observers and occurrence points such as auroral arcs, curtain-like auroras, and coronal auroras. The auroral arc is generally located along the east-west direction, and its longitudinal length ranges from several hundred kilometers to more than a thousand kilometers. The arc thickness varies from hundreds of meters to tens of kilometers. The discrete aurora appears on the high-latitude auroral oval, as shown by the lines in **Figure 1.8**. The acceleration mechanisms of the discrete aurora have been investigated in detail by in-situ satellite observations and ground-based observations. Nowadays it is thought that not only a quasi-static acceleration by a parallel potential drop, but also an Alfvén wave acceleration, are important factors, as described in detail in the next chapter. Both mechanisms accelerate electrons coming from the plasma-sheet boundary layer into the ionosphere along the magnetic field line, using the parallel electric field.

The diffuse aurora is characterized by weak auroral emissions and consists of patches, veils, or pulsations. It often appears on the low-latitude side of the discrete aurora over a wide region for 1–2 hours, as shown by the shaded region in **Figure 1.8**. The electrons producing the diffuse aurora come from either the central plasma sheet or the near-Earth plasma sheet, and undergo pitch angle scatters by whistler waves around the magnetic equator. Since the electron energies used to produce the pulsating aurora are so high (on the scale of hundreds keV), it is thought that the electrons would have significant impact on the variation of the upper atmosphere throughout the process.

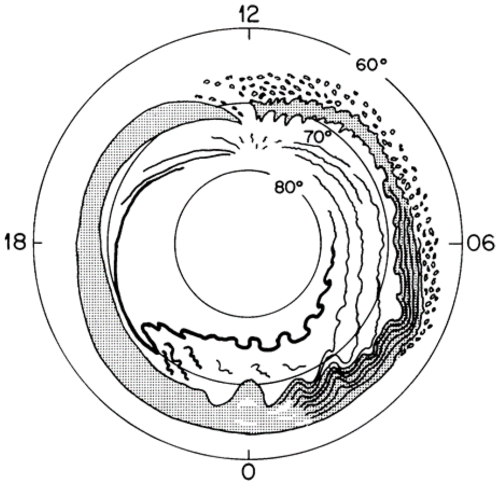

Figure 1.8: Schematic diagram showing the occurrence locations of the discrete aurora and the diffuse aurora shown by lines and shaded regions, respectively (From *Akasofu* [1976]).

1.4 Acceleration Mechanisms of Discrete Aurora

1.4.1 Quasi-static Acceleration

From rocket and satellite observations, the characteristic structures of precipitating electrons have been observed on the energy-time (E-T) spectrogram within the auroral arcs. These electrons have a monoenergetic peak between 1 and 10 keV and show variations in the peak energy flux, whose peak energy first increases then decreases in the so-called inverted-V structure [e.g., *Frank and Ackerson*, 1971]. **Figure 1.9** shows conjugate observational results using the FAST satellite to observe particle properties and an aircraft to capture all-sky images. When the satellite passed over the multiple arcs elongated in the east-west direction, a number of inverted-V electrons were observed. This result denotes an apparent one-to-one correspondence between the presence of the inverted-V structure and the auroral arc.

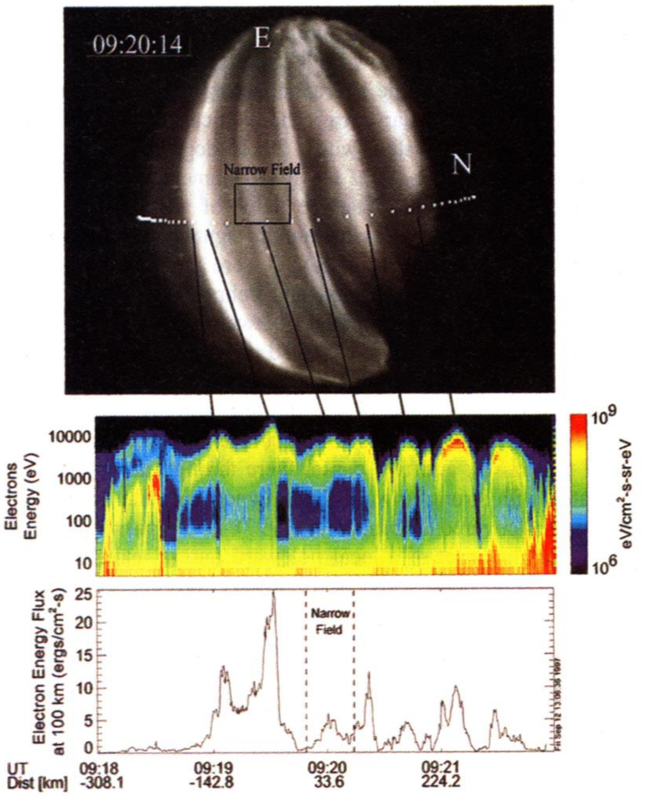

Figure 1.9: Snapshot of the multiple arcs captured from an aircraft (top). A number of inverted-V structures (middle) and a variation of the precipitated energy flux (bottom) obtained from the FAST observations when the satellite passed over the multiple arcs (From *Stenbaek-Nielsen et al.* [1998]).

Another characteristic feature of the quasi-static acceleration is the large electric field (500–1000 mV m^{-1}) discovered by S3-3 satellite observations [*Mozer et al.*, 1977]. This electric field is thought to be the source of the discrete auroral arcs [*Torbert and Mozer*, 1978]. **Figure 1.10** shows the electric field and the particle observations done within the region of the auroral magnetic field line by the FAST satellite [*Ergun et al.*, 2000]. Panel (a) shows the electric field perpendicular to the ambient magnetic field around and inside the acceleration region, with large positive and negative changes. This result represents the convergence of the electric field structure and implies the existence of a parallel electric field to accelerate electrons. Panels (c–d) display the energy-time diagrams for electrons and ions, respectively; downward-accelerated electrons and upward-moving ion beams were simultaneously observed. This result indicates that upward parallel electric fields exist both below and above the satellite. Panel (b) displays the plasma density profile within the acceleration region; a depletion of the plasma density, the so-called plasma cavity, is clearly seen. It is found that the plasma cavity is dominated by plasma sheet electrons with temperatures over 100 eV and that the density inside the cavity region is often less than 1 cm^{-3}.

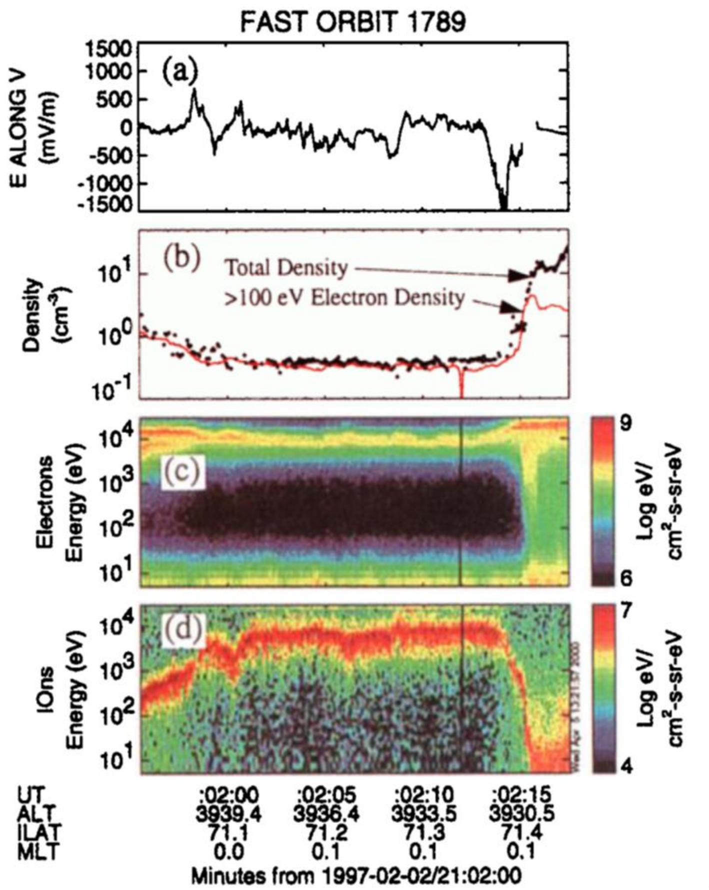

Figure 1.10: Variations of the electric field perpendicular to the magnetic field, the electron density, and E-T diagrams for the electron and ion inside the quasi-static acceleration region observed by the FAST satellite (From *Ergun et al.* [2000]).

Theoretical investigation of the quasi-static potential drop has been addressed. *Knight* [1973] established a current-voltage relation, the so-called ‘Knight relation’, which is written by a simple proportional relation between the field-aligned current in the ionosphere ($j_{/\!/ion}$) and the parallel potential drop ($\Delta\Phi_{/\!/}$) over a broad range $1 \ll e\Delta\Phi_{/\!/}/k_B T_e \ll R_M$ as follows:

$$j_{\parallel ion} = K\Delta\Phi_{\parallel}$$

where T_e and R_M are electron temperature, and the mirror ratio, and K is the Knight conductance given by

$$K = \frac{e^2 n}{\sqrt{2\pi m_e k_B T_e}},$$

where m_e and n are electron mass and density.

This relationship shows that the parallel electric field can drive the field-aligned current against the magnetic mirror force, although Knight did not give a theoretical description of how the parallel electric fields are supported and how they are distributed. *Morooka et al.* [2003] illustrated the seasonal dependence of the altitude profile of the parallel acceleration region by using the Akebono satellite. They reported that most of the electron acceleration region is located at lower altitudes (3000–6000 km) in the winter season, although there is no apparent dependence of the altitude profile over a 3000–11000 km range in the summer. They suggest that the seasonal changes to the acceleration region are likely controlled by the seasonal changes of the ambient plasma density on the auroral field line. Auroral kilometric radiation (AKR) has also been used for the altitude estimation of the auroral acceleration region, because it is emitted from the density cavity region through wave-particle interactions. *Morioka et al.* [2007] found two sources of AKR which develop prior to and during the substorm. The low-altitude source region appears during the substorm growth phase in the altitude range from 4000–5000 km. On the other hand, the high-altitude source region abruptly appears at the substorm onset in the altitude range from 6000–12000 km, due to either the current-driven instability or the Alfvénic acceleration.

Detailed altitude distributions for the quasi-static potential drop have been investigated by various rocket and satellite observations. **Figure 1.11** is a schematic illustration of the altitude distribution of the parallel potential drop in the upward current region [*Ergun et al.*, 2004] derived from satellite observations and simulation studies. The location of the auroral potential is generally between ~1/2 and 2 R_E in altitude, and the parallel electric fields are concentrated in at least two locations along the magnetic field line. A low-latitude potential drop generally carries ~10% to ~50% of the total potential drop at the boundary layer between the ionospheric plasma and the cavity region and is characterized by a strong ($e\Delta\Phi > T_{e,i}$, where $T_{e,i}$ are the electron and the ion temperature) oblique double layer. Density cavities are confined by two layers of the electric field. Inside the auroral cavity, the majority of the population is made up of electrons of magnetospheric origin and, often, ions of ionospheric origin, and the quasi-neutrality is required by the electric field.

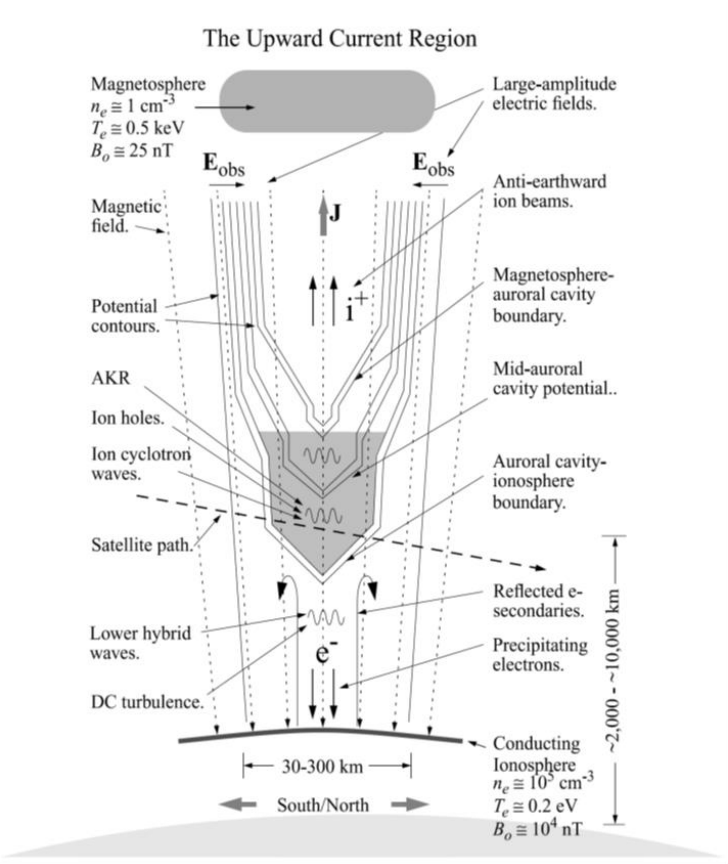

Figure 1.11: A schematic illustration of the parallel potential drop of the upward current region. Dashed lines and solid lines indicate the magnetic field line and the equipotential line, respectively (From *Ergun et al.* [2004]).

1.4.2 Alfvénic Acceleration

Although the inverted-V acceleration is a prevailing mechanism behind large auroral structures with sizes ranging from a few kilometers to tens of kilometers, how small-scale auroral structures are created has remained an open question for over half a century [e.g., *Maggs and Davis*, 1968]. *Borovsky* [1993] reviewed 22 mechanisms behind auroral arcs and concluded that there is no process to explain widths on the order of 100 m. The acceleration by Alfvén waves, the so-called Alfvénic acceleration, has been proposed for the smallest scale of the aurora [e.g., *Stasiewicz et al.*, 2000].

The Alfvén wave is a low-frequency electromagnetic wave in a conducting fluid. Assuming that the Alfvén wave propagates obliquely with an angle θ to the magnetic field line, which is oriented along the z-axis, it is possible to obtain three wave modes under the linear analysis of MHD equations for a wave with frequencies below the ion gyrofrequency: a shear Alfvén wave, and fast and slow magnetosonic waves. The shear Alfvén wave has a frequency

$$\omega = \pm k V_A cos\theta$$

$$V_A = \frac{B}{\sqrt{\mu_0 \rho_i}}$$

where V_A is the Alfvén velocity, and B, μ_0, and ρ_i are the strength of the magnetic field, the permeability of free space, and the mass density of ions and electrons, respectively. The wave is purely transverse (incompressible), and does not propagate at $\theta = \pi/2$, because the magnetic tension force vanishes at this value. The fast and slow magnetosonic waves have the frequency

$$\left(\frac{\omega}{k}\right)^2 = \frac{1}{2}\left\{V_A^2 + C_A^2 \pm \left[(V_A^2 + C_s^2)^2 - 4V_A^2 C_s^2 \cos^2\theta\right]^{\frac{1}{2}}\right\},$$

where

$$C_s = \sqrt{\frac{\gamma P_0}{\rho_0}}$$

where Cs is the speed of sound and P_0, ρ_0, and γ are the unperturbed thermal pressure, the mass density, and the ratio of specific heats, respectively. These two magnetosonic waves are compressible and correspond to the fast (+ sign) and slow (- sign) modes. The fast mode propagates in all directions, and the phase speed in the perpendicular direction ($\theta = \pi/2$) is faster that the Alfvén speed mode. However, the slow mode cannot propagate perpendicular to B. The fast mode arises from the in-phase oscillation of the magnetic and plasma perturbations, and the slow mode arises from their out-of-phase oscillations.

An ideal MHD wave cannot generate a parallel electric field and thus the wave does not contribute particle accelerations to form the auroral emission. There is, however, a domain that is changed by the dispersion relation of the Alfvén waves, where the wave can produce a parallel electric field. This happens when the wavelength perpendicular to the magnetic field becomes comparable either to the ion gyroradius at the electron temperature, $\rho_s = (T_e/m_i)^{1/2}/\omega_{c,i}$, the ion thermal gyroradius, $\rho_i = (T_i/m_i)^{1/2}/\omega_{c,i}$ [*Hasegawa*, 1976], or the collisionless electron skin depth, $\lambda_e = c/\omega_{p,e}$ [*Goertz and Boswell*, 1979], where $\omega_{c,i}$ is the ion cyclotron frequency and $\omega_{p,e}$ is the electron plasma frequency given by

$$\omega_{c,i} = \frac{q_i B}{m_i}$$

$$\omega_{p,e} = \sqrt{\frac{n_e e^2}{m_e \varepsilon_0}}.$$

There are two different forms of dispersive Alfvén waves (DAWs) with frequencies less than $\omega_{c,i}$ which have a field-aligned electric field depending on the altitude. They are traditionally categorized into inertial Alfvén waves (IAWs) and kinetic Alfvén waves (KAWs). At the magnetosphere, the shear Alfvén waves are launched through a sheared plasma flow during magnetic storms or reconnections, and propagate towards the ionosphere. At higher altitudes, the electrons are significantly hotter, and their thermal velocity, $V_{te}=(2T_e/m_e)^{1/2}$, is higher than V_A. In an intermediate β plasma region ($m_e/m_i < \beta < 1$), the wave is characterized as a KAW, and the parallel electric force is balanced by the parallel electron pressure gradient. The dispersion relation and the electric field of the KAW can be written as follow:

$$\omega^2 = k_\parallel^2 V_A^2 \left[1 + \left(\frac{ck_\perp V_{te}}{\omega_{pe} V_A}\right)^2\right]$$

$$\frac{E_\parallel}{E_\perp} = -\frac{k_\parallel k_\perp \rho_s^2}{1 + k_\perp^2 \rho_i^2}.$$

At lower altitude, however, where the plasma β is low ($\beta < m_e/m_i$) at only 2–3 R_e above the ground surface, V_{te} is less than V_A and thus the wave has the property of an IAW, whose parallel electric field is supported by the electron inertia. The dispersion relation and the electric field of the IAW is

$$\omega^2 = \frac{k_\parallel^2 V_A^2}{1 + k_\perp^2 \lambda_e^2}$$

$$\frac{E_\parallel}{E_\perp} = \frac{k_\parallel}{k_\perp} \frac{k_\perp^2 \lambda_e^2}{1 + k_\perp^2 \lambda_e^2}.$$

When $k_\perp^2 \lambda_e^2 \lll 1$, this relation is same as the relation of the MHD Alfvén waves.

The electrons accelerated by the Alfvén waves have broad energy ranges from tens of eVs to keVs, field-aligned distributions, and time-of-flight (TOF) energy dispersions [e.g., *Arnoldy et al.*, 1999; *Tung et al.*, 2002; *Chen et al.*, 2005]. **Figure 1.12** shows an example of simultaneous observations for the electrons and the auroral distribution obtained from the REIMEI satellite, which consecutively observed electrons accelerated by both Alfvén wave and quasi-static inverted-V potential. The discrepancy in the electron energy range is clearly seen during the first 10 s and the last 10s in **Figure 1.12a**. Wavenumbers perpendicular to B were estimated from the vorticity as shown in **Figure 1.12d-e**, which is calculated from the optical flow. The figure shows the different distributions of the wavenumbers between the two acceleration mechanisms, using a dispersion relation for the Alfvén wave and a current-voltage relation for the theoretical quasi-static acceleration model.

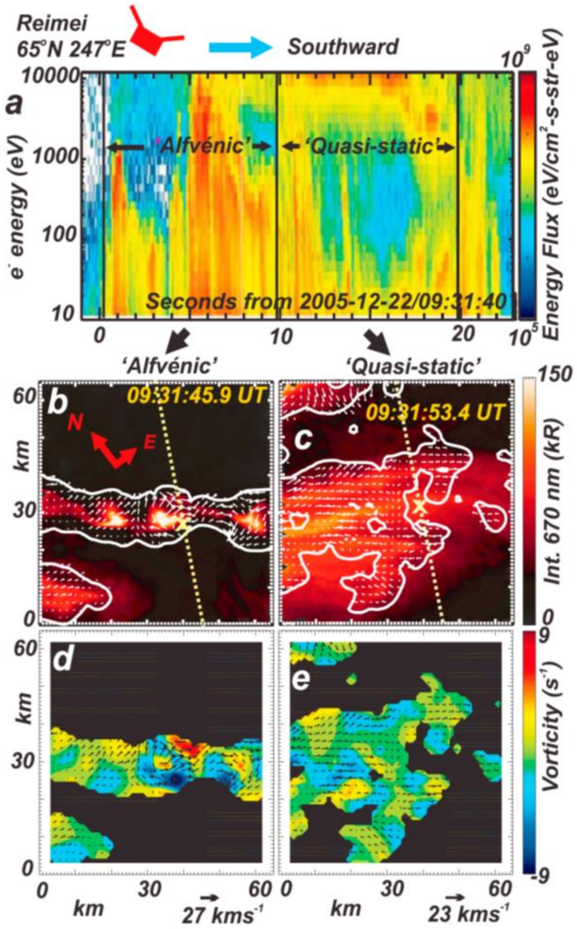

Figure 1.12: Simultaneous observation of electrons (a) and fine-scale auroral structures (b and c) accelerated by the Alfvén wave and the quasi-static potential obtained from the REIMEI satellite. Vorticity (d and e) derived from the optical flows is shown by the small arrows in Panel b-e (From *Chaston et al.* [2010]).

After detailed study of small-scale auroral morphology, *Semeter et al.* [2006; 2008] reported that breakup arcs consist of "arc packet" structures on the order of 100 m, which repeatedly propagate away from the center of the arc packet and then fade out at some distance like a cascade, as shown in the left panel of **Figure 1.13**. They proposed that the small-scale motion is formed by the upward parallel electric field of the inertial Alfvén wave propagating obliquely within a resonance cone, as shown in the right panel of **Figure 1.13**. A schematic illustration indicates that the auroral structures move with a group velocity perpendicular to B away from the center of the arc, when the inertial Alfvén wave propagates away from an apex of the resonance cone.

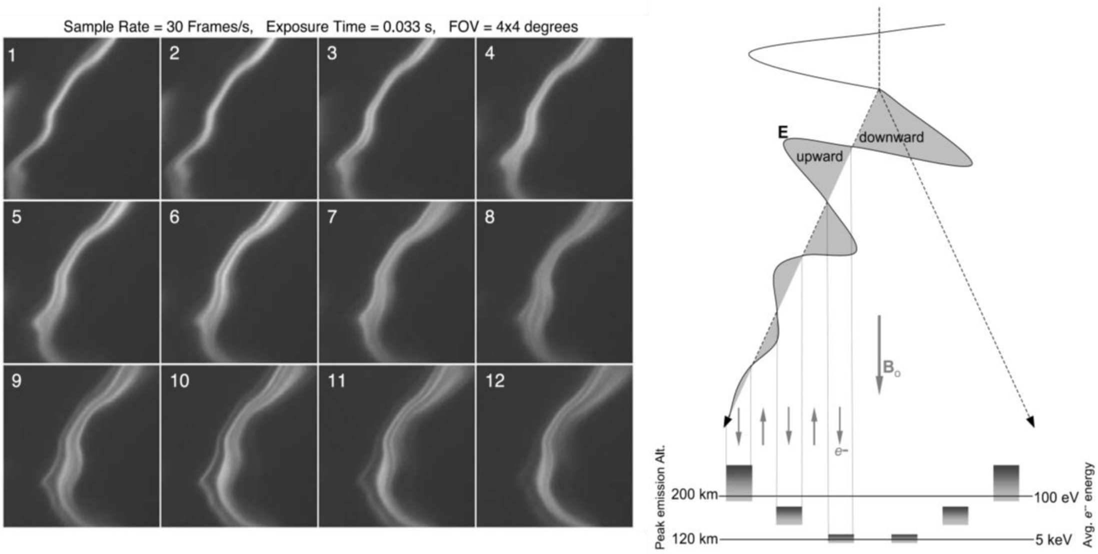

Figure 1.13: Schematic illustration of auroral structures formed in an inertial Alfvén resonance cone by the electron acceleration process through the parallel electric field of the dispersive Alfvén wave (From *Semeter et al.* [2008]).

Figure 1.14 also shows the simultaneous optical and electron observations obtained from the REIMEI satellite [*Asamura et al.*, 2009]. Electrons accelerated by the inertial Alfvén wave are embedded with the inverted-V electrons during two time periods shown by blue horizontal lines in the top panel of **Figure 1.14**. While these electrons are observed, there are four distinct arcs labeled A, B, C, and D in the bottom panel of **Figure 1.14**. These arcs have fine structures such as folds, vorticities, and shear flow motions with speeds between 14–18 km s^{-1}. *Asamura et al.* [2009] proposed that instabilities in the shear flow motion may drive the emission of the inertial Alfvén wave, which then accelerates electrons below the quasi-static acceleration region.

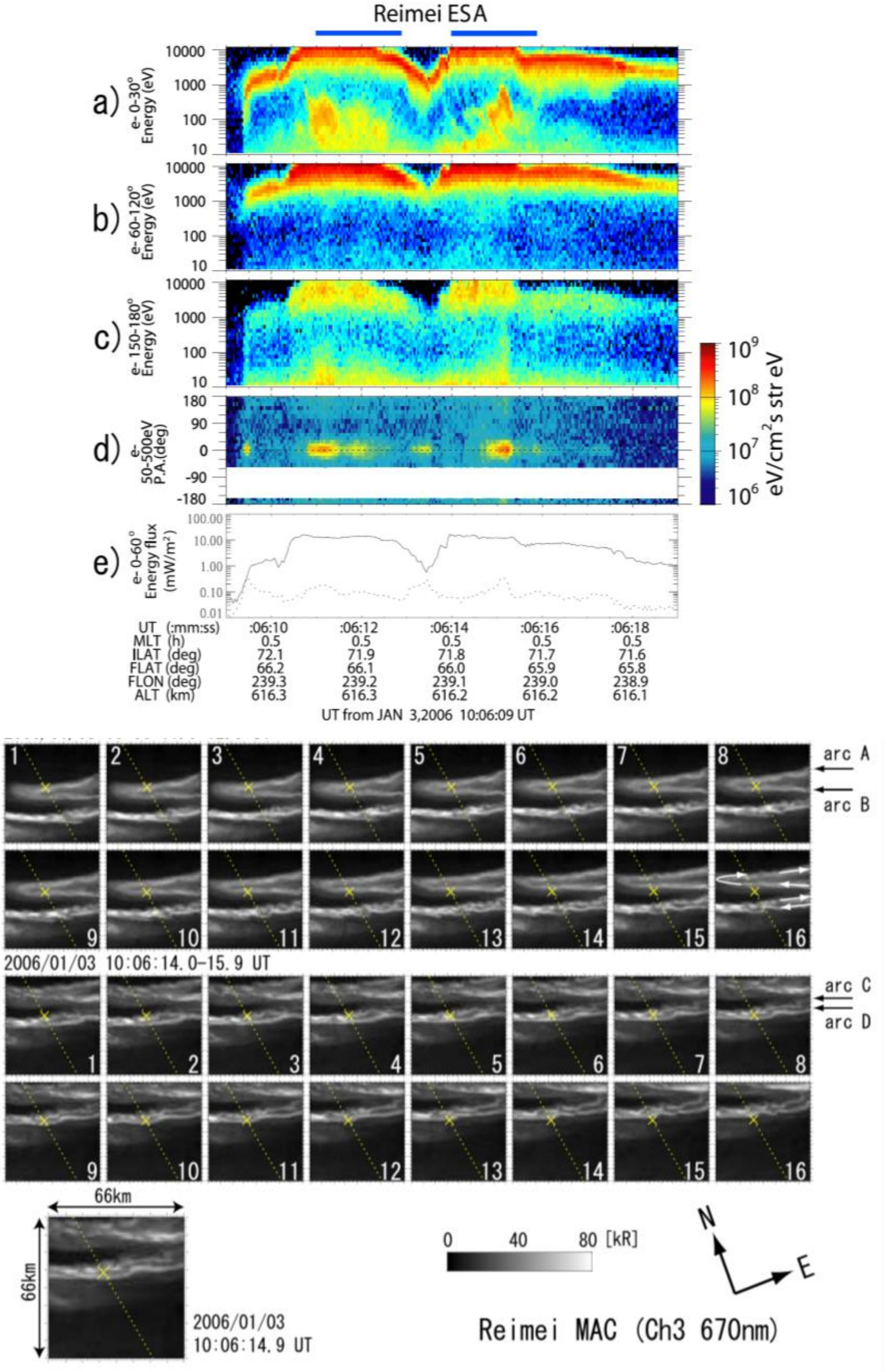

Figure 1.14: Simultaneous measurements of electrons (topl) and fine-scale auroral structures (bottom) obtained from the REIMEI satellite (From *Asamura et al.* [2009]).

1.5 Flickering Aurora

1.5.1 General Property

A flickering aurora is a type of discrete aurora with periodic luminosity oscillations, and has been observed by ground-based imaging observations since the 1960s [e.g., *Paulson and Shepherd*, 1966]. The flickering aurora was named by *Beach et al.* [1968] in distinction from pulsating auroras, which are classified under the diffuse aurora. It typically appears as small spots or patches within active and bright auroral arcs, or as surges just prior to and during auroral breakup [*Beach et al.*, 1968; *Berkey et al.*, 1980; *Kunitake and Oguti*, 1984; *Sakanoi and Fukunishi*, 2004]. When viewed along the magnetic field line, it forms clusters of rotating and drifting small spots or patches with 1–20 km diameters [e.g., *Beach et al.*, 1968; *Oguti*, 1978; *Kunitake and Oguti*, 1984; *Sakanoi and Fukunishi*, 2004; *Sakanoi et al.*, 2005]. When viewed from the perpendicular direction to the magnetic field line, on the other hand, it appears as vibrating columns of auroras vertically elongated up to 10–40 km [*Oguti*, 1978; *Kunitake and Oguti*, 1984; *Sakanoi and Fukunishi*, 2004]. The typical frequency is 3–15 Hz [e.g., *Paulson and Shepherd*, 1966; *Beach et al.*, 1968] which is comparable to oxygen ion cyclotron frequencies at altitudes of a few thousand kilometers. The flickering amplitude has often been reported as 10%–20% of the background auroral intensity [*Berkey et al.*, 1980; *Kunitake and Oguti*, 1984; *Sakanoi and Fukunishi*, 2004; *Gustavsson et al.*, 2008; *Grydeland et al.*, 2008; *Whiter et al.*, 2010].

1.5.2 Generation Model

Many satellites and sounding rockets have observed electron flux modulations in auroral arcs. These electrons are considered to form the flickering aurora. They usually appear as field-aligned electron bursts (FABs) with a repetitive frequency ranging from a few Hz up to the vicinity of 100 Hz [*Lin and Hoffman*, 1979; *Spiger and Anderson*, 1985; *McFadden et al.*, 1987], which are embedded into the inverted-V electrons. They also have energy dispersion structures over a wide range from a few tens of eV up to a few keV, which is comparable to inverted-V energies as shown in **Figure 1.15** [e.g., *Arnoldy et al.*, 1999; *Tung et al.*, 2002; *Chen et al.*, 2005]. On the other hand, some studies reported that the electron energy range was well above the inverted-V energy, reaching values up to 120 keV [e.g., *Evans*, 1967; *Arnoldy*, 1970], and that it was restricted to a narrow energy range below the peak energy, of only 10–20 keV [e.g., *Spiger and Anderson*, 1985; *McFadden et al.*, 1987]. The source altitudes of the FABs have been estimated at 2400–11000 km, which is comparable to the altitude range of the parallel potential drops, using three different methods: energy-time dispersions [*McFadden et al.*, 1987; *Arnoldy et al.*, 1999; *Tung et al.*, 2002], pitch angle-time dispersions [*Temerin et al.*, 1993; *Arnoldy et al.*, 1999], and the lag time of wave oscillations and electron flux modulations [*Lund et al.*, 1995].

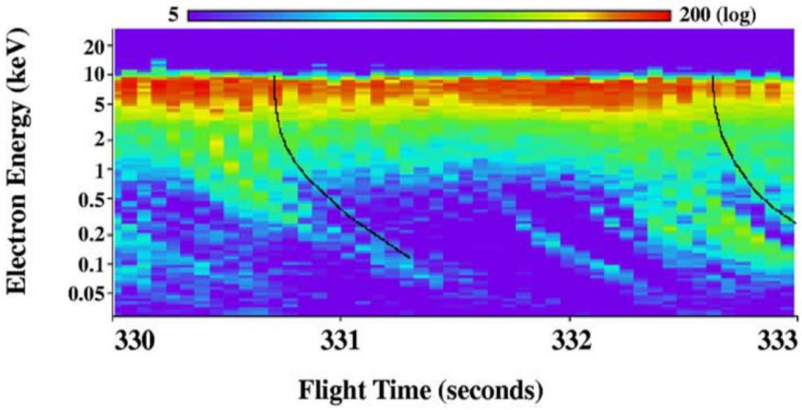

Figure 1.15: An example of field-aligned electron bursts observed by the PHAZE-II rocket. The color scale shows the count rate in units of 10^3 counts/s (From *Arnoldy et al.* [1999]).

There were several models postulated to explain the repetitive electron bursts. *Evans* [1967] suggested that the flux oscillations could be produced by wave-particle interaction. The plasma waves excited by a monoenergetic electron beam resonate with the electrons of a certain gyrofrequency and heat them up to high energy in a direction perpendicular to B. The flux oscillation is caused by the repetitive relaxation variation of the wave with a time constant from excitation to damping. *Perkins* [1968] quantitatively extended Evans' model to explain stochastic acceleration by electrostatic plasma waves due to beam-driven instability. They estimated a critical value of the monoenergetic electron flux (7×10^9 cm^{-2} s^{-1} str^{-1}) required to cause the stochastic acceleration, and found that the acceleration occurs on a time scale of 10^{-2} s. This model, however, could not form lower-energy field-aligned flux modulations.

To interpret the lower-energy field-aligned flux modulation, *Lin and Hoffman* [1979] suggested that the field-aligned fluxes were produced from cold secondary electrons heated parallel to B by Langmuir waves, which are assumed to be produced by instabilities in the primary inverted-V electrons although the large wave amplitudes required to cause the wave heating have not been observed. *Lotko* [1986] also suggested that the cold secondary electrons are trapped at the edge of the acceleration region through a turbulent process of E × B drift motion and are released by an ion cyclotron wave.

Arnoldy et al. [1999] reported FABs which have energy dispersion ranging from the order of an eV to a keV, and pitch angle-dispersions at energies equivalent to inverted-V electrons at the same time. In order to explain these signatures, they proposed another mechanism: a spatially limited inverted-V potential that turns on and off at ion cyclotron frequencies.

The most widely supported model is Landau resonance interactions between electrons and electromagnetic ion cyclotron (EMIC) waves, suggested by *Temerin et al.* [1986]. The equation of the resonance condition is given by

$$V_{\parallel p} = \frac{\omega}{k_{\parallel}} = V_{\parallel e},$$

where $V_{/\!/p}$ and $V_{/\!/e}$ are the parallel phase velocity of EMIC waves and the parallel velocity of the resonance electron, respectively. EMIC waves are dispersive Alfven waves with a dispersion relation given by

$$\frac{\omega^2}{k_{||}^2} = \frac{{V_A}^2\left(1 - \frac{\omega^2}{\omega_{ci}^2}\right)}{1 + k_{\perp}^2\lambda_e^2},$$

when $k_{\perp} \gg k_{/\!/}$, and electric fields can be written as follow:

$$\frac{E_{||}}{E_{\perp}} = \frac{\omega\left({}^{m_e}/_{M_i}\right)^{1/2}}{\left(\omega_{ci}^2 - \omega^2\right)^{1/2}\left(1 + {}^{1}/_{k_{\perp}^2\lambda_e^2}\right)^{1/2}}.$$

We get the dispersion relation of the IAW from that of EMIC waves using the low frequency limit $\omega \ll \omega_{ci}$. **Figure 1.16** represents altitudes profiles of the magnetic field strength, number densities of the electron and ions, cyclotron frequency, and electron inertia length, respectively. The magnetic field is calculated by the IGRF model in the magnetic zenith at the observational site. The height profiles of the proton and oxygen are given by

$$n_H = 1200/\,exp\left(\frac{z}{5000}\right)$$

$$n_O = \frac{2.64\times10^6}{exp\left(\frac{50.42\times z}{15000}\right)} + \frac{n_H}{1.5}$$

$$n_e = n_H + n_O,$$

where n_H, n_O, and n_e are number densities (cm^{-3}) of protons, oxygen ions, electrons at the altitude z (km), respectively. These relations were modified by *Sakanoi et al.* (2005) based on the altitude profiles used by *Temerin et al.* [1986] and represent the typical density in the auroral acceleration region except for the cavity region. The cyclotron frequencies and electron inertial length were calculated from the modelled magnetic field and electron density profiles, respectively.

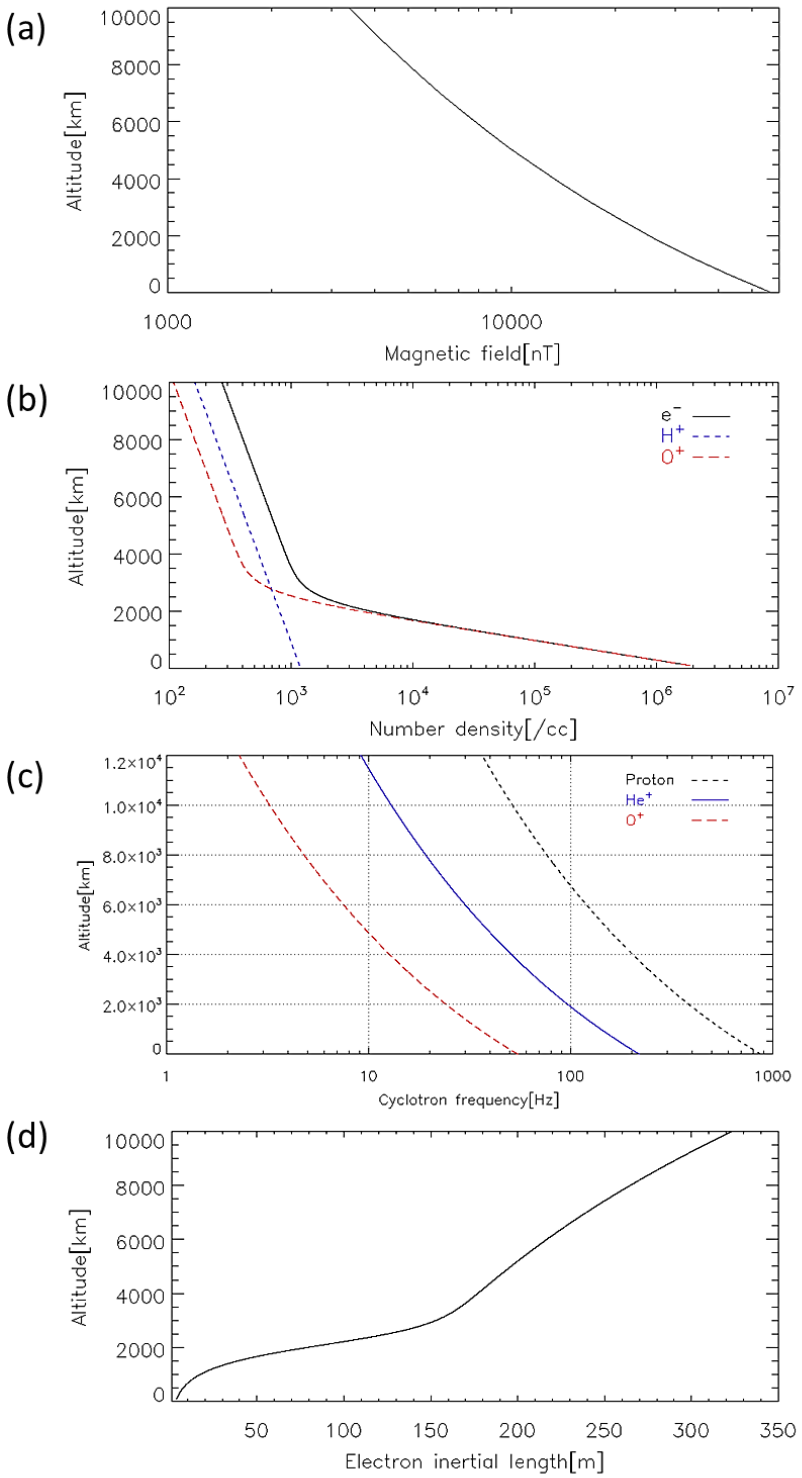

Figure 1.16: Altitudes profiles of the magnetic field strength (a), number densities of electrons, protons, and oxygen ions (b), cyclotron frequency of protons, helium and oxygen ions (c), and electron inertial length (d), respectively.

As shown in **Figure 1.17**, the parallel phase velocity of the wave increases as the wave propagates toward the ionosphere, but its amplitude decreases. They showed that some of the field-aligned electrons originated from the ionosphere (cold secondary electrons) and that the ionospheric electrons trapped or reflected by the wave were accelerated up to keV energies below the main auroral acceleration region by a test particle simulation. They also found that the electron flux was modulated at the wave frequency depending on a local cyclotron frequency. However, it is pointed out that in this model, the electrons were accelerated up to only a few keV by realistic wave amplitudes [*McFadden et al.*, 1987].

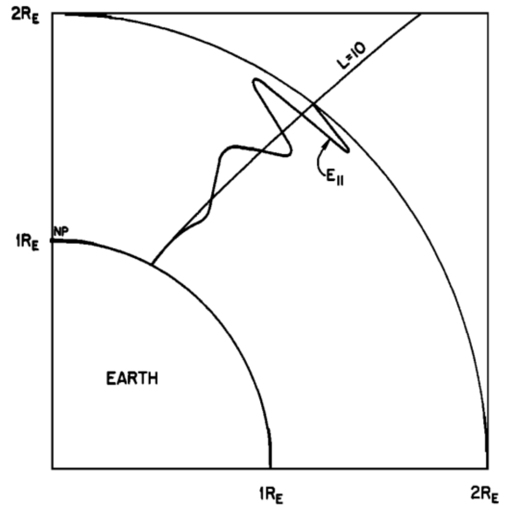

Figure 1.17: A schematic illustration of the amplitude and parallel phase velocity of the electromagnetic ion cyclotron wave (From *Temerin et al.* [1986]).

Lund et al. [1995] reported a first simultaneous observation of FABs and electromagnetic wave oscillations obtained by a sounding rocket launched into a strongly flickering auroral arc as shown in **Figure 1.18**. All the frequencies of the electron flux modulation, the wave oscillation, and the auroral intensity variation were approximately 10 Hz, which is comparable to the oxygen ion cyclotron frequency at an altitude of 4500 km. *Temerin et al.* [1993] showed in a simulation study that the H^+-band EMIC wave with frequencies between f_{He+} and f_{H+} could create flux modulations of field-aligned electrons with the same frequency; the result was supported by simultaneous observations of particles and waves obtained from the FAST satellite [*McFadden et al.,* 1998]. Other satellites and sounding rockets have identified H^+-band EMIC waves [e.g., *Gurnett and Frank*, 1972; *Temerin and Lysak*, 1984; *Gustafsson et al.*, 1990; *Erlandson and Zanetti*, 1998].

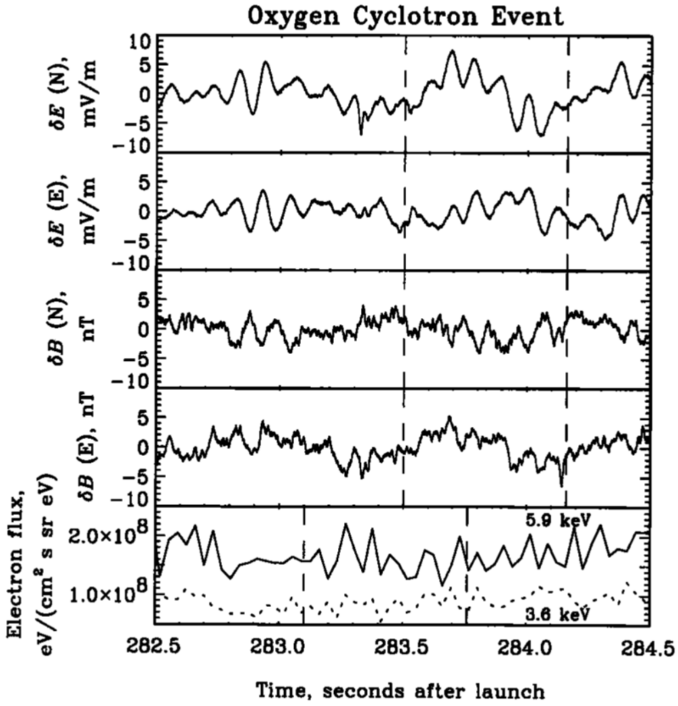

Figure 1.18: A simultaneous observation result of electromagnetic waves and electron flux fluctuations with oxygen ion cyclotron frequencies observed by the Auroral Turbulence sounding rocket launched into the flickering aurora (From *Lund et al.* [1995]).

Erlandson and Zanetti [1998] statistically investigated the occurrence property of EMIC waves using the Freja satellite and showed that the wave often occurs at auroral latitudes (68°–72° invariant latitudes) in the premidnight sector (1800–0100 MLT) with a seasonal dependence, whose properties are same as those of the inverted-V electron precipitation. They suggested that the free energy of EMIC waves is the auroral electron precipitation. The plausible candidate has been thought of as a beam-driven instability, which occur in or just below the auroral acceleration region [e.g., *Temerin and Lysak*, 1984]. Numerical studies on the growth rate of O^+ EMIC waves, however, could not explain the observation [*Lund and LaBelle,* 1997]. In order to increase the growth rate, the colder electron beam or the larger beam density relative to the total electron density, which means the auroral cavity region, than assumed model are required. These results also implying that nonlinear or inhomogeneous plasma effects must play an important role in the instability. In addition, the maximum convective growth rate is clearly proportional to the frequency except frequencies close to the cyclotron frequencies duo to the cyclotron damping effects. The excitation mechanisms of EMIC waves including the effects of the nonlinear inhomogeneous plasma with the finite temperature has remained an open question.

In a multi-ion species plasma, the propagation properties of EMIC waves in the multi-ion plasma are more complicated than those in a single species as shown in Appendix [*Smith and Brice*, 1964].

Gustafsson et al. [1990] also reported that He^+-band events at frequencies between the cyclotron frequency of oxygen ions, f_{O+}, and that of f_{He+} were observed by the Viking satellite, although it was revealed by ray tracing calculations that these waves are typically difficult to detect because the He^+-band wave tends to latitudinally spread out to an extent that exceeds those of the H^+-band and O^+-band waves with frequencies $<f_{O+}$ [*Lund and LaBelle,* 1997]. *McHarg et al.* [1998] found auroral intensity fluctuations with a broadband frequency in the range of 35–60 Hz and with a maximum frequency of 180 Hz by using a ground-based high-speed photometer, and these fluctuations were interpreted as lighter ions such as He^+ or H^+.

The generation mechanisms of the temporal and spatial structures of the flickering aurora have been considered. *Sakanoi et al.* [2005] suggested that the spatiotemporal variations of flickering patches can be formed by interference waves, which are consisting of an incident wave and a reflected wave, in a resonance cone as shown in the top left panel of **Figure 1.19**. The top right panel of **Figure 1.19** shows a schematic illustration of the dark (A) and bright (B) flickering patches which are formed by the downward (A') and upward (B') parallel electric field of a single wave with a perpendicular propagation angle. The scale of the flickering patch corresponds to half of the perpendicular wavelength ($\lambda_\perp$) of the wave mapped onto the auroral emission altitude, and the flickering frequency is reflected by the wave frequency. *Sakanoi et al.* [2005] also showed that the interference wave with opposite perpendicular wave vectors could form standing flickering patches (Case A) and drifting flickering patches in the horizontal direction with time (Case B), as shown in the bottom panel of **Figure 1.19**, using a simple equation given by

$$E_{\parallel} = E_{\parallel 1} \cos(k_{x1}x + k_{z1}z - \omega_1 t) + E_{\parallel 2} \cos(k_{x2}x + k_{z2}z - \omega_2 t),$$

where $E_{\parallel s}$, k_{xs}, k_{zs}, and ω_s are the parallel electric field, the horizontal and vertical wavenumbers, and the angular frequency of the s-th wave, respectively. In order to get a clear insight into the spatiotemporal patterns of the flickering patch, it is assumed that $E_1 = E_2 = E$ and k_z is constant at a given altitude z, and then the equation shown above can be rewrote as follow:

$$E_{\parallel} = \ 2E\, cos\left(\frac{1}{2}\{(k_{x1} + k_{x2})x - (\omega_1 + \omega_2)t)\}\right) \cdot cos\left(\frac{1}{2}\{(k_{x1} - k_{x2})x - (\omega_1 - \omega_2)t)\}\right).$$

This equation clearly shows that $E_{/\!/}$ has two modulated components of the wave frequency and the horizontal phase velocity: a high-frequency component with frequency $\omega_h = (\omega_1 + \omega_2)/2$, a low-frequency component with frequency $\omega_l = (\omega_1 - \omega_2)/2$, a large phase velocity $v_{ph} = 2\omega_h/|k_{x1} + k_{x2}|$, and a small phase velocity $v_{pl} = 2\omega_l/|k_{x1} - k_{x2}|$. The interference wave comprising two waves with two different frequencies and wavenumbers makes beat and moire patterns, determined by ω_h, ω_l, v_{ph}, and v_{pl}, in the spatial and temporal variation. *Gustavsson et al.* [2008] also showed that the rotating motion of the flickering patch could be formed by more than two waves, by extension of Sakanoi's model.

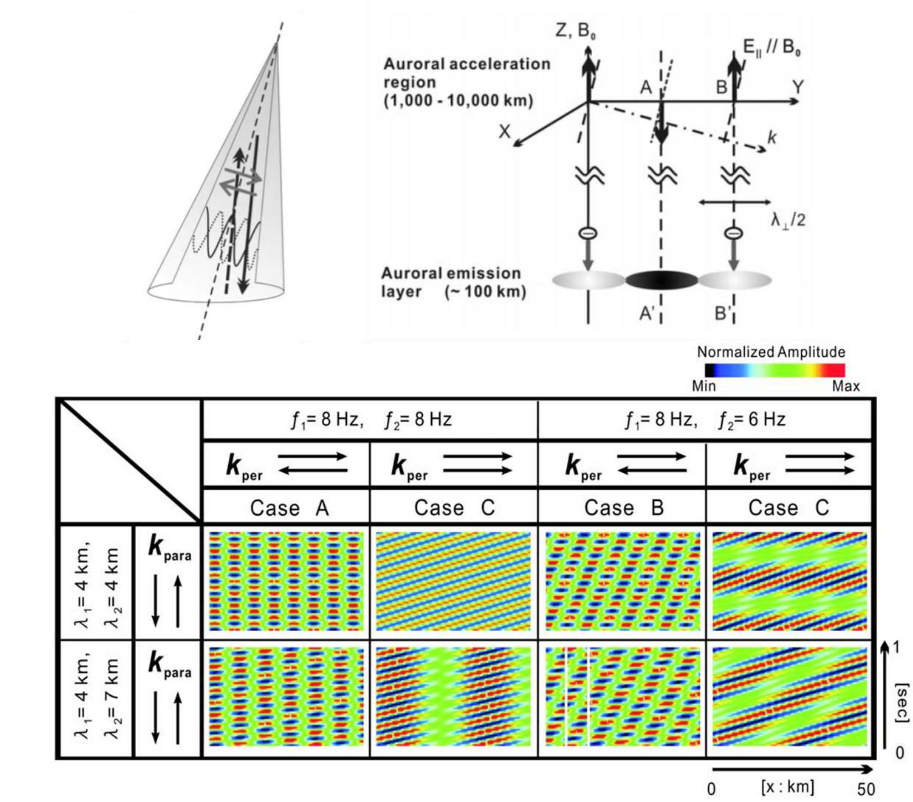

Figure 1.19: A schematic illustration of the generation mechanism of the flickering patch (above) and calculation results of time variations of the flickering patch formed by interference waves (bottom) (From *Sakanoi et al.* [2005]).

1.5.3 Recent Observations

A multispectral narrow FOV (3.1° × 3.1°) observation revealed that many examples of the smallest flickering structures as narrow as 160 m at the ionospheric altitude, which were four times larger than the spatial resolution of the camera [*Whiter et al.*, 2008]. In order to investigate the spatial characteristics, *Michell et al.* [2012] conducted 2D-spatial Fourier analyses of the flickering events. **Figure 1.20** shows power spectral densities of the flickering event in the north-south and east-west directions. They showed that an asymmetry of the flickering patch scale, whose east-west direction was twice as large as its north-south direction, and also that the perpendicular wavenumber does not extend larger than 2×10^{-3} m^{-1}. They suggested that the asymmetry of the patch structures is produced by interfering EMIC waves with different k and ω. The smallest scale of the flickering structure is comparable to the O^{+} ion gyroradius scale. They also suggest that the finite gyroradius effect makes a cutoff of the flickering patch size.

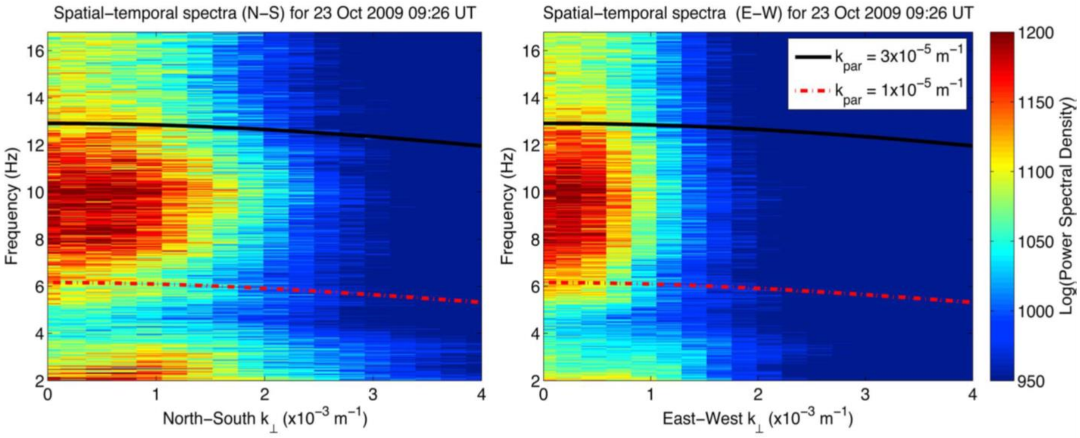

Figure 1.20: Spatial power spectral densities of the north-south and east-west directions (From *Michell et al.* [2012]).

Whiter et al. [2008] also reported that there is a temporal correlation between the flickering strength and the background auroral intensity, although there is no spatial correlation between the two on a small scale. They concluded that the spatial de-correlation is possible to be formed by EMIC waves rather than the on/off turning of the potential structure proposed by *Arnoldy et al.* [1999].

Whiter et al. [2010] found rise or fall signatures of the flickering frequency with short intervals (1–2 s), called chirps, in a few flickering events as shown **Figure 1.21**. They also found that the flickering electron energies are from 10 to 40 keV, which were estimated from a power spectral density ratio of OI and N_2 emissions, and that the flickering electron energies were higher than the background non-flickering electron energies estimated from the intensity ratio of OI and N_2. This results indicate that the wave acceleration occurs at altitudes above the potential drop and the flickering electron is accelerated by the potential drop again. *Kataoka et al.* [2011] reported that the precipitating electron energy at the leading front of the moving flickering patch is higher than that at the trailing part, by taking high-speed observations at wavelengths of 670.5 and 844.6 nm. They suggest that this signature probably associated with the Landau damping or TOF effect.

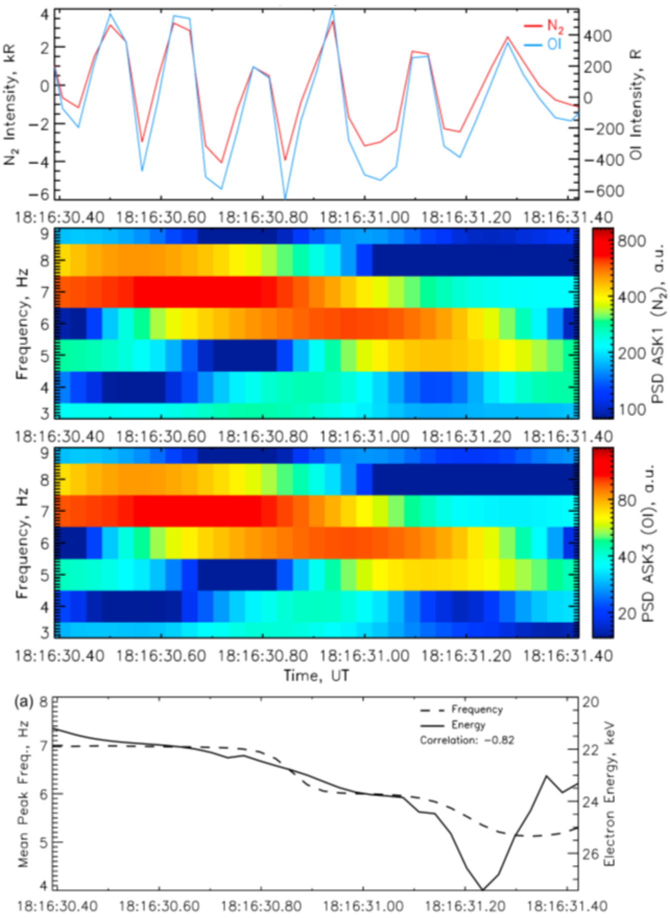

Figure 1.21: Intensity and frequency variations of two emissions when a down chirp was observed. Flickering electron energies were estimated from the power spectral density ratio of the two emissions (From *Whiter et al.* [2010]).

Recently, *Yaegashi et el.* [2011] determined that approximately one third of flickering events involved broadband frequencies in the range of 20–50 Hz by using high-speed imaging, as shown **Figure 1.22**. The flickering events could not be explained by O^+ EMIC waves, shown by a dashed line, because the frequency ranges and spatial scales estimated by the Fourier analysis were not consistent with the theoretical dispersion curve of the O^+ EMIC wave. These results indicate that He^+ and H^+ EMIC waves may also contribute to produce the high frequency flickering auroras. However, the time resolution of the imaging system was not sufficiently high to detect variations >50 Hz due to the 100 fps sampling.

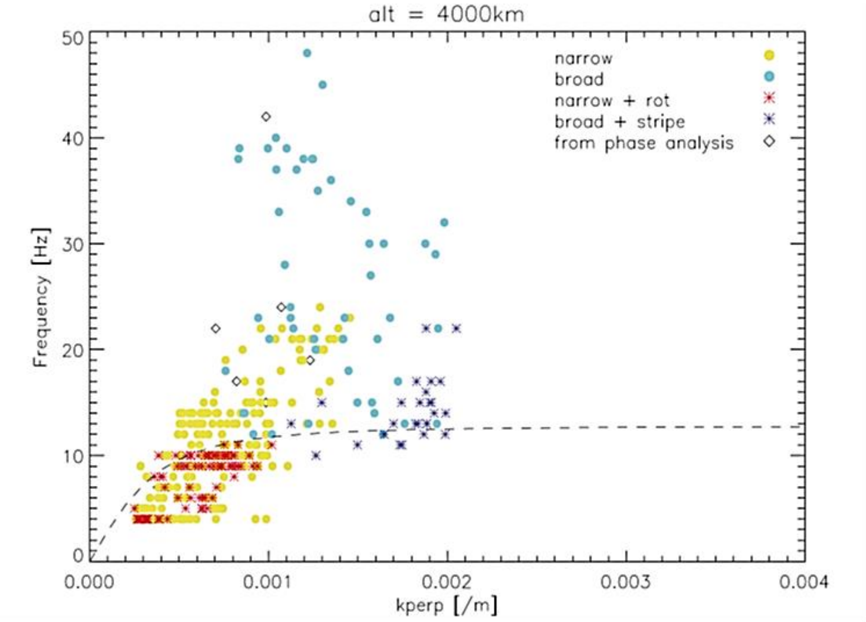

Figure 1.22: Dispersion relation estimated from the flickering frequencies and the patch sizes observed by the ground-based imaging of a 100 fps sampling (From *Yaegashi et al.* [2011]).

1.6 Purpose

The main purpose of this thesis is to elucidate the generation mechanisms of the flickering aurora. The flickering aurora has been thought to be generated near the auroral acceleration region where is corresponding to M-I coupling region and is required comprehensive understanding through the field-aligned current. The cavity region, which is also thought to be the source of the flickering aurora, is also regarded as an excitation source of many plasma waves. In order to understand the generation mechanisms of the fine-scale auroral morphology including the flickering aurora, it is necessary to clarify the wave excitation process and the wave interaction with electrons. In this study, we installed the ground-based high-speed imaging observation as a means of visualizing the M-I coupling region in detail. Understanding the generation mechanisms of the flickering aurora would contribute to our comprehension of the plasma physics for the wave-particle interaction within the auroral acceleration region.

In order to elucidate the generation mechanisms, this study focuses on the occurrence property and the frequency property of the flickering aurora. Many previous studies have reported that flickering auroras often occur just before and during the auroral breakup. However, there has also been a few reports on flickering auroras that were not associated with a breakup [e.g., Berkey et al., 1980; *Kunitake and Oguti*, 1984; *McHarg et al.*, 1998; *Sakanoi and Fukunishi*, 2004]. *Sakanoi* and *Fukunishi* [2004] pointed out that the flickering occurrence rate is not necessarily proportional to the auroral luminosities.

The characteristics of auroral with and without flickering structure has been remained unclear, since the statistical study on the flickering aurora is rare. In this study, statistical studies are conducted to investigate the relations between the flickering occurrence and the background auroral intensity and the background micro-scale shear motions by developing the continuous observational system.

Another basic property of the flickering aurora is flickering amplitudes. The flickering amplitude to the background auroral intensity has been reported to be 10%–20% in many previous studies [*Berkey et al.*, 1980; *Kunitake and Oguti*, 1984; *Sakanoi and Fukunishi*, 2004; *Gustavsson et al.*, 2008; *Grydeland et al.*, 2008; *Whiter et al.*, 2010]. However, the origin of this ratio is not yet understood. In this study, we statistically investigate the flickering amplitude and aim to clarify the meaning of the flickering amplitude.

In a multi-ion species plasma, H^+-band EMIC waves were identified by in situ satellite observations [e.g., *Gurnett and Frank*, 1972; *Temerin and Lysak*, 1984; *Gustafsson et al.*, 1990; *Erlandson et al.*, 1998]. *McFadden et al.* [1998] reported the simultaneous observation of H^+-band EMIC waves and the flux modulation of field-aligned electrons with the same frequency as the wave by using the FAST satellite, which was predicted based on a simulation study by *Temerin et al.* [1993]. *Gustafsson et al.* [1990] also reported that He^+-band events were observed by the Viking satellite, although it was revealed by ray tracing calculations that these waves are typically difficult to detect because the He^+-band wave tends to latitudinally spread out to an extent that exceeds those of the H^+-band and O^+-band waves [*Lund and LaBelle*, 1997]. These satellite observations imply the possibility that both He^+-band and H^+-band EMIC waves contribute to produce high-frequency flickering auroras.

McHarg et al. [1998] found auroral intensity fluctuations with a broadband frequency in the range of 35–60 Hz and with a maximum frequency of 180 Hz by using a ground-based high-speed photometer, and these fluctuations were interpreted as lighter ions such as He^+ or H^+. Recently, *Yaegashi et el.* [2011] found that approximately one third of flickering events involved broadband frequencies in the range of 20–50 Hz by using high-speed imaging. The flickering events were interpreted as He^+-band EMIC waves as opposed to O^+-band EMIC waves. However, the time resolution of the imaging system was not sufficiently high to detect variations >50 Hz due to the 100 fps sampling. In order to investigate the frequency property of the flickering aurora, we test the hypothesis that the flickering auroras are generated by multi-ion EMIC waves by realizing the ground-based high-speed imaging observation with a sampling rate of 160 fps.

As an application of the high-speed imaging observations, we focus on rapid spatial motions of the pulsating aurora. The pulsating aurora is characterized by an irregular ON-OFF switching of the auroral intensity and a quasi-periodic intensity modulation of 3 Hz. The complicated spatial and temporal motions of pulsating patches have been observed and classified into several types [e.g., *Oguti*, 1978; *Yamamoto and Oguti*, 1982]. However, spatial variation in pulsating patches associated with the 3 Hz intensity modulation has rarely been reported, except for *Nishiyama et al.* [2016]. In order to investigate the fundamental property of the pulsating aurora, such as the velocity and the direction for the motion, we investigate the rapid spatiotemporal motions of the pulsating aurora.

This thesis consists of 7 chapters. In Chapter 1, a general introduction of the Magnetosphere and the Ionosphere, an introduction of the flickering aurora, and purpose of this thesis are presented. In Chapter 2, high-speed imaging cameras used in this study and the new observational system with the auroral auto-detection system is described. In Chapter 3, in order to clarify the basic property of the flickering aurora, the statistical study on the occurrence property of the flickering aurora and on the flickering amplitude are described. In Chapter 4, an event study on the fastest flickering aurora was investigated to clarify the frequency property of the flickering aurora. In Chapter 5, I also investigate another aurora with quasi-periodic luminosity oscillation, that is the pulsating aurora, with the spatial motion accompanied with the 3 Hz modulation, as an application of the high-speed imaging observations. In Chapter 6, we comprehensively discuss the necessary condition and the generation mechanisms of the flickering aurora. General conclusions are given in Chapter 7.

2 Observations

In order to investigate the basic properties and the fastest modulation of the flickering aurora, our observational system needed to be designed so that the fine-scale structure on the order of 10 m with the fast motion at over 100 Hz can be continuously detected. To achieve the spatiotemporal resolution, an observational system had been developed by National Institute of Polar Research (NIPR) and Institute for Space-Earth Environmental Research (ISEE) at Nagoya University since 2014 as a collaborative project. The author was particularly involved with the development of a continuous observational system shown in Section 2.3. The observational system and the setting parameters to acquire images were updated every year. This chapter describes the specifics of the cameras used in this study, the configuration of the observation system and the data acquisition systems, for three winter seasons.

2.1 Instrumentation

2.1.1 sCMOS Camera

In order to reveal the high-speed and fine-scale auroral morphology, we introduced scientific complementary metal-oxide semiconductor (sCMOS) cameras (ORCA-Flash 4.0 V2, Hamamatsu Photonics, shown in **Figure 2.1**). The readout structure of CMOS image sensors is different from that of well-known charge coupled device (CCD) image sensors. Each pixel of the CCD image sensor consists of a photodiode and a container to convert the incident light into accumulated electric charges at each container. The electric charges are carried by the bucket brigade method and finally converted into an amplified voltage. In contrast, each pixel of the CMOS image sensor consists of a photodiode and an amplifier to convert the incident light into amplified voltages. The voltage is directly read out from each pixel by continuous switching. The CMOS image sensor can also read out only signals from the selected area, which is referred to as a sub-array function, using on-chip column analog-to digital converters. This function enables the high-speed read out, depending on the selected area size. In addition, correlated double samplings are adopted to suppress the generation of the noise. Due to these differences in the sensor structure, the CMOS image sensor is able to achieve a low-noise and high-speed readout. The sCMOS camera used in this study actually achieved the high-speed readout of up to 100 fps for the 2048 × 2048 pixel image, which could not be accomplished by other CCD cameras. For these reasons, it can be said that the greatest advantage of the sCMOS is the high spatiotemporal resolution.

Figure 2.1: sCMOS camera (ORCA-Flash 4.0 V2, Hamamatsu Photonics) equipped with a NIKKOR 50 mm/F1.2 lens.

2.1.2 Calibration

An important factor to determine the sensitivity of cameras is a quantum efficiency (*QE*), which is a conversion efficiency from incident light (*P*) to the electric charge. The quantum efficiency of the sCMOS camera used in this study is also adequately high; it is more than 80% at 600 nm. An input signal (*S*) detected in one pixel is expressed as follows:

$$S = P \times QE \times M$$

where M is a multiplication constant of the charge in EM-CCD (Electron Multiplying CCD) camera, which is referred to as EM gain, with a range from 1 to 1200. EM-CCD cameras are also one of the sensitive cameras widely used. The value of EM gain of the sCMOS camera is 1, since the sCMOS camera does not have the charge multiplication.

In order to know the performance of the sCMOS camera, it is important to quantitatively evaluate the noise level. A total noise detected in one pixel is given by:

$$N = \sqrt{N_s^2 + N_r^2 + N_e^2 + N_d^2 + N_b^2}$$

where N_s is the photon shot noise, N_r is the readout noise, N_e is the excess noise, N_d is the noise from the dark current, and N_b is the background light. The photon shot noise is caused by fluctuations of the conversion from the incident light to charge and is expressed as follows:

$$N_s \propto \sqrt{P \times QE}$$

The readout noise is caused by reset on the conversion amplifier from charge to voltage. The excess noise is produced by the charge multiplication in the EM-CCD camera, and the noise factor (*Fn*) is statistically calculated to be $\sqrt{2}$. The factor of the CMOS camera is 1. The others are noises that caused by the dark current occurring even without the incident light and by the background light when the background light is overlapped with the object light. The main factors to determine the detection limit of the camera are the readout noise and dark current of the sensor. According to the catalog values, a 2048 × 2048 pixel image acquired at the 100-fps sampling rate necessarily includes the readout noise of 1.0 electrons (the median value) and of 1.6 electrons (the root mean square (rms)). The dark current noise of 0.06 electrons/pixel/s is also included. The root sum square value of the readout noise (rms) and the dark current noise can be estimated as 3.5 count by using a coefficient conversion from count to electron corresponding to 0.46 electrons/count. The value corresponds well with the standard deviation obtained from the calibration experiment shown in **Figure 2.2**.

We conducted calibration experiments using an integrating sphere owned by NIPR before the observation. **Figure 2.2** shows the frequency distribution for a bias intensity which is likely to consist of the readout noise and the dark current in each pixel of two different images which were captured with the different exposure times of 1 ms and 100 ms, respectively. These images were obtained without binning option and shielded from the background light by using the lens cap. **Figure 2.2a** shows that the median values and the standard deviations of bias intensity of each image are approximately 100 count and 3.3 count, respectively, despite of the exposure time. The standard deviation is consistent with the catalog value. **Figure 2.2b** shows the frequency distributions when 4 × 4 binning is applied, the median values and the standard deviations are approximately 1600 count and 14 count, respectively. Since our observation was always conducted by using the 4 × 4 binning option to gain the intensity, the bias intensity of 1600 count was subtracted from the original auroral intensity data in advance, and the intensity variation less than ±7 count was regarded as the noise.

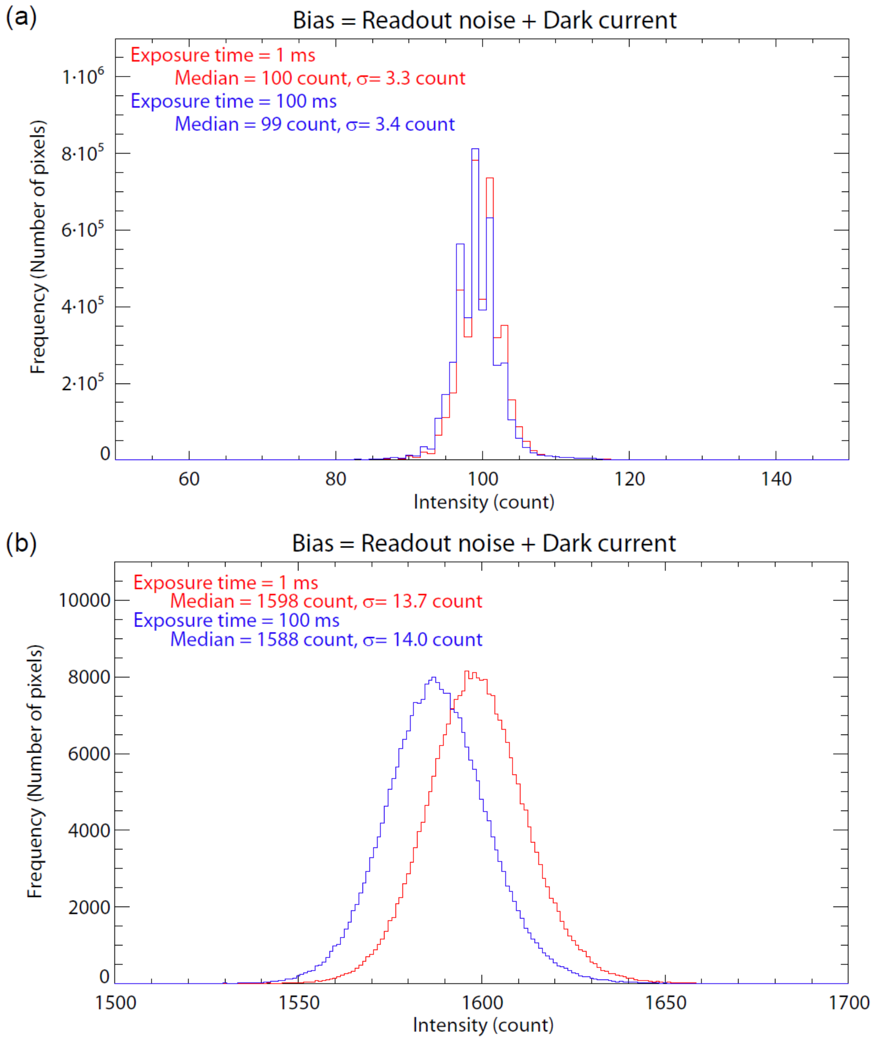

Figure 2.2: Frequency distributions of a bias intensity caused by the readout noise and the dark current in each pixel of two images which were captured with the different exposure times of 1 ms (red) and 100 ms (blue) by using no binning option (a) and the 4 × 4 binning option (b).

In order to quantitatively evaluate the signal-to-noise ratio (S/N) of the sCMOS camera, the following equation is defined:

$$\frac{S}{N} = \frac{\overline{Signal} - \overline{Bias}}{Standard\ \ deviation\ \ of\ \ Signal}$$

where *Signal* is the median value of the intensity of the incident light, and *Bias* is the median value of the bias intensity shown in **Figure 2.2**. **Figure 2.3** shows the S/N of the sCMOS camera with respect to the intensity of the incident light. Since the previous studies report that the flickering amplitude is 10%–20% of the background auroral intensity [*Berkey et al.*, 1980; *Kunitake and Oguti*, 1984; *Sakanoi and*

Fukunishi, 2004; *Gustavsson et al.*, 2008; *Grydeland et al.*, 2008; *Whiter et al.*, 2010], the incident light intensity is needed to exceed approximately 400 count, which satisfies the S/N >10, in order to detect the flickering aurora with the amplitude >10% using 4 × 4 binning option.

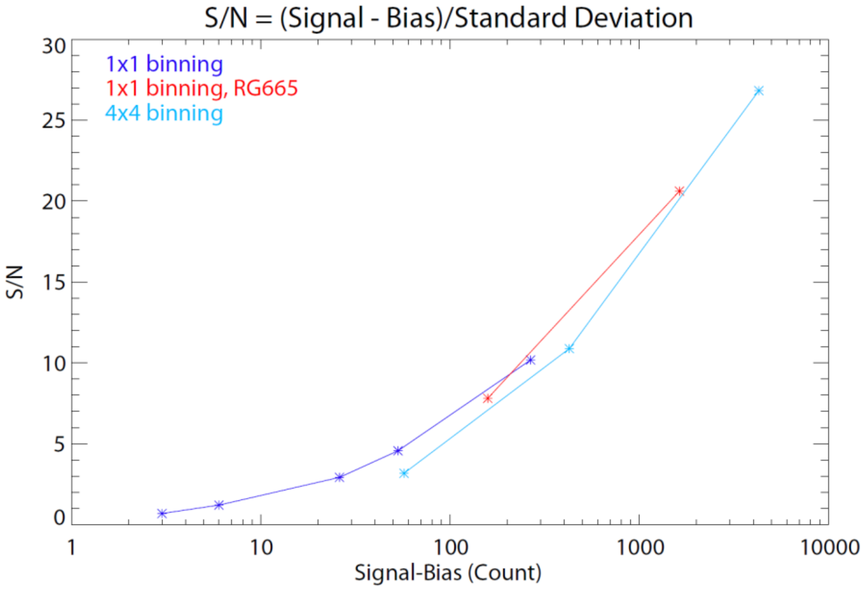

Figure 2.3: S/N values for the sCMOS camera with respect to the incident light intensity.

Recently, the EM-CCD camera is also used to investigate the fine-scale fast auroral variation [e.g., *Whiter et al.*, 2008; *Dahlgren et al.*, 2012; *Michell et al.*, 2012; *Yaegashi et al.*, 2011]. **Figure 2.4** shows the S/N values of our sCMOS camera and the typical EM-CCD camera (ImagEM) with respect to the incident light. The S/N shown here is relative to the value of a perfect device with 100% quantum efficiency and no noise. The setting condition to acquire the data are the following: EM gain × 1200, 30-ms exposure time, and the background light of 10 photons/pixel. The result shows that the S/N of the sCMOS camera always exceeds that of the EM-CCD camera, even though the amount of the incident light is low. The result also shows that the sCMOS camera is more suitable for the imaging of the bright object, such as the auroral breakup, than the EM-CCD camera, since the S/N of the sCMOS camera gradually increases with the increase of the incident light, although it reaches the peak at approximately 200 photons/pixel in this case.

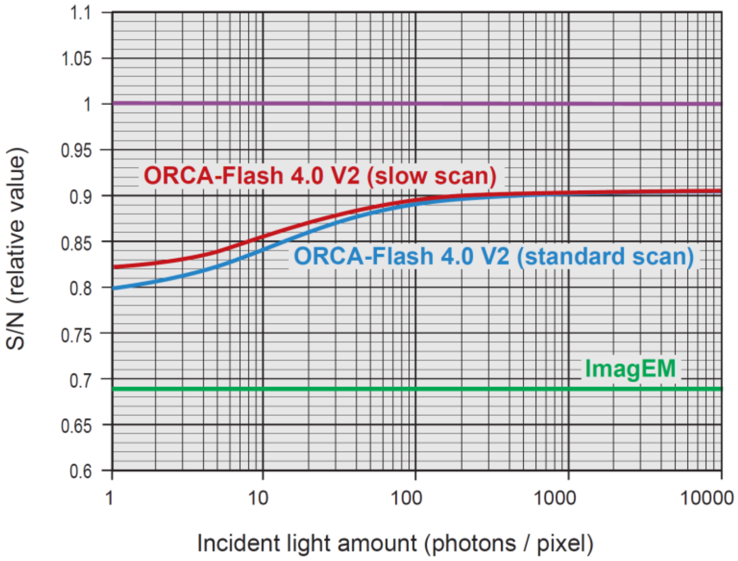

Figure 2.4: Relative S/N values for the sCMOS camera and the EM-CCD camera with respect to the incident light intensity (From *Technical Note for ORCA-Flash 4.0 V2* [2015]).

We conducted panchromatic observations without the optical filter, as shown in Section 2.2. In this case, count values obtained from the sCMOS camera cannot be converted into Rayleigh values. Fortunately, all-sky imaging observations using EM-CCD cameras equipped with three typical optical filters for emissions of 427.8 nm, 557.7 nm, and 630.0 nm have been performed by the University of Alaska at the same location. **Figure 2.5** shows the auroral intensity relations between our sCMOS camera and the all-sky cameras at three wavelengths. The vertical axis shows the calibrated Rayleigh value of the all-sky image, which is averaged over the FOV of the sCMOS camera. The horizontal axis represents the accumulated count values of the sCMOS camera during an exposure time of the all-sky observation. These relations enable rough estimations of the count Rayleigh conversion.

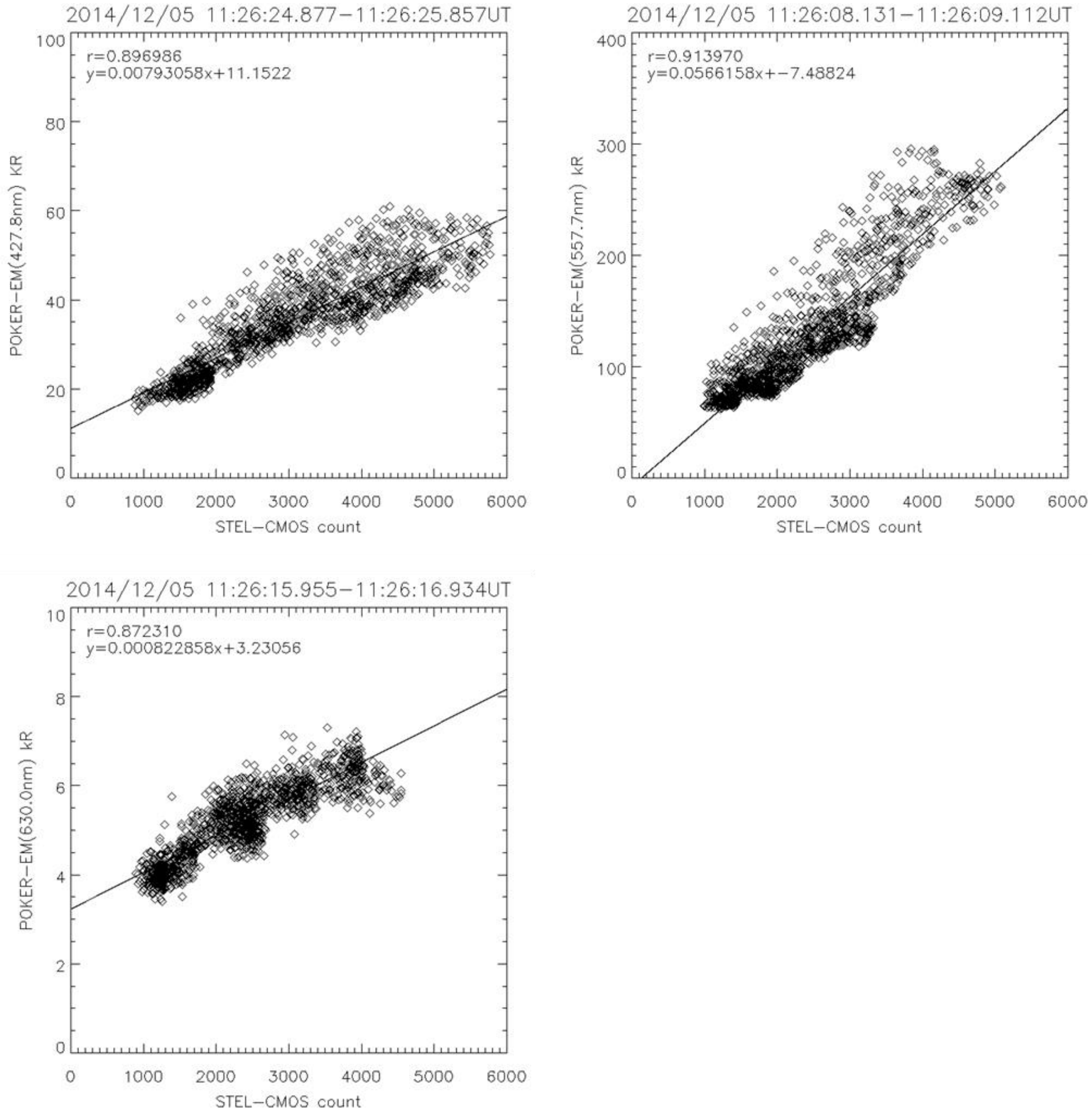

Figure 2.5: Auroral intensity relations between the count value of the sCMOS camera and the calibrated Rayleigh value of the all-sky camera owned by the University of Alaska at three wavelengths, 427.8 nm, 557.7 nm, and 630.0 nm, respectively.

2.1.3 Optical Filter

To observe the fast auroral motion, auroral emissions with shorter lifetimes are preferred, because these short-lived emissions are thought to be more clearly captured than the long lifetime emissions. To remove the long lifetime oxygen emissions, such as the 557.7 nm and 630.0 nm emissions corresponding to 0.7 s and 110 s, respectively, a SCHOTT RG665 optical filter was used. **Figure 2.6** indicates the internal transmittance spectrum of the optical filter. Using this filter, short lifetime emissions of 6 μs at

670.0 nm (N_2 1st positive band) are expected to be detected. The filter was equipped in front of a lens using a filter holder.

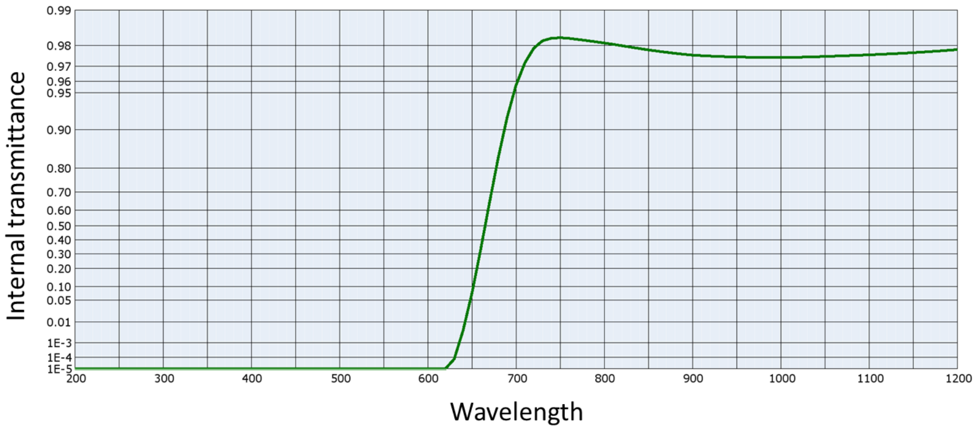

Figure 2.6: Transmittance spectrum of SCHOTT RG665 filter.

2.2 Observational System

The observations were performed using two identical sCMOS cameras owned by NIPR and ISEE, hereafter referred to as sCMOS 1 and sCMOS 2, respectively. Both cameras were installed next to each other at Poker Flat Research Range (PFRR) in Alaska. Our motivation for using the two cameras is to achieve extreme spatiotemporal resolution without sacrificing standard resolution (e.g., record-fast with not too narrow FOV), by using appropriate different lens and setting parameters as shown in Section 2.2.1–2.2.3. PFRR is just under the auroral zone and located at 65.11°N, 147.43°W (65.74° MLAT, L = 5.9). At this point, LT is shown by LT = UT–9, and MLT midnight approximately corresponds to 11:40 UT (MLT = UT–11:40). The geomagnetic declination and inclination are 18.5° and 77.5°, respectively. The center of the FOV of each camera was directed to the magnetic zenith in order to capture the fine auroral structure without perspective.

The observation was conducted using an automatic observational system and then remotely monitored and controlled. The observational system was originally developed for other auroral cameras of Hamamatsu Photonics by Yusuke Ebihara (Kyoto Univ.). The observational system is designed so that the camera automatically starts and stops capturing images at a given sampling rate and binning, based on astronomical twilight, that is, when the solar elevation angle is –12° below the horizon. An additional observational mode designed to capture images only at a specified recording time was introduced by Naoki Sunagawa (Nagoya Univ.).

The inner clock of the control PC for the sCMOS camera was regularly fixed by an NTP server. The data acquisition starts from 0 s every minute and continues for a given recording time less than 60 s. The obtained data is saved as a raw file every minute, and a tiff file averaged for 10 s is saved as a quicklook image every 10 s. Absolute times when each image was captured, which are based on the control PC, are written into a log file in addition to other setting parameters, such as the sampling rate, the binning, and the sub-array area.

One problem of the continuous high-speed fine-scale observation is the storage of a huge amount of data. Although the sCMOS camera has an imaging sensor with 2048 × 2048 pixels, in order to increase the sampling rate and the signal to noise ratio, the images were first reduced down to 512 × 512 pixel images by 4 × 4 binning. The size of one 512 × 512 pixel image is 0.52 MB when the color depth is 16 bit per pixel. If the image is captured at a sampling rate of 50 fps with a recording time of 10 s in 1 minute, the image size become 262 MB/minute, which correspond to 15.7 GB/hour. If the observation is continuously conducted for 10 hours every night during one winter season (120 days), the data amount will grow to 20 TB. For this reason, 40 TB (4 TB × 10) of external hard disk drives were prepared as a data storage medium for one camera every year, including spare storage. **Figure 2.7** shows an optical dome of PFRR and a schematic of the basic observational system inside the dome. **Figure 2.8** shows two pairs of control PCs and external HDDs for each sCMOS camera set up at the loft of the observatory.

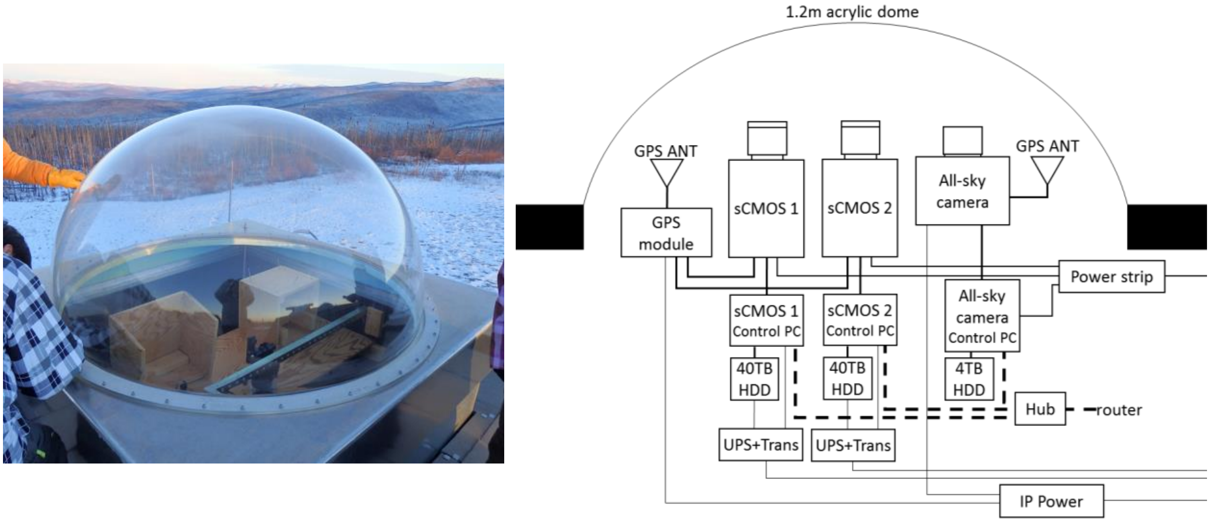

Figure 2.7: 1.2-m optical dome of PFRR (left) and schematic of the basic observational system (right).

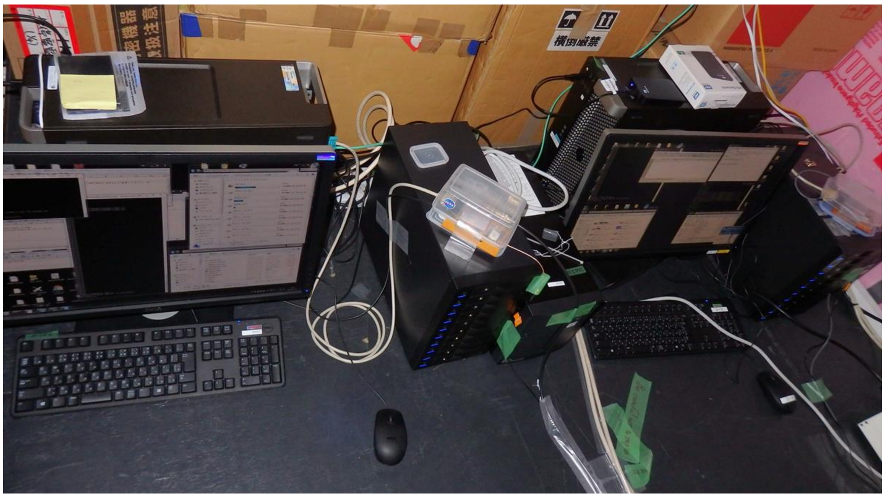

Figure 2.8: Two pairs of control PCs and external HDDs for each sCMOS camera set up at the loft of the observatory.

To obtain the auroral fine-scale structure, a narrow field-of-view (FOV) lens of NIKKOR 50 mm/F1.2 was equipped to one camera every year. From the size of the image sensor, the FOV is estimated to be approximately 14.8° × 14.8°, corresponding to an area of 26.0 km × 26.0 km at the altitude of 100 km. When the final image size is 512 × 512 pixels, the spatial resolution is approximately 51 m at the altitude of 100 km, which is enough to capture the flickering patch reported to occur on scales hundreds of meters to several tens of kilometers by previous studies.

2.2.1 First Winter Season (February 2014–April 2014)

The challenge of the high-speed imaging observation began from 2014. The main aim of the first winter season is to achieve the correct operation of the two cameras with the different sampling rates in order to simultaneously detect the flickering auroras with the traditional frequency and the higher frequency that have never been observed before. Each of the sampling rate of sCMOS 1 and sCMOS 2 was set at 50 fps and 200 fps, respectively. The image size of sCMOS 2 was downward converted to 512 × 128 pixels by using the sub-array function instead of increasing the sampling rate. Each camera equipped the same narrow FOV lens (NIKKOR 50 mm/F1.2). The observation was conducted for only the first 10 s in every minute. The RG665 filter was equipped with only sCMOS 2 because of the high sampling rate of 200 fps. In order to monitor the all-sky auroral morphology, a digital single-lens reflex (DSLR) camera (D4, Nikon) with a fisheye lens (8 mm/F2.8, NIKKOR) was installed at the same location, and took color images every 10 s.

For comparative studies of the two high-speed sCMOS cameras, both cameras needed to be synchronized by imposed signals, taking into consideration the poor accuracy of the inner clock of the control PC. During the first winter season, LED lights were used as the imposed signal, with a frequency of 1 Hz triggered by PPS (Pulse Per Second) signals from the GPS. The LED lights were equipped with each filter holder of the camera and flashed simultaneously. The flash covered approximately two-thirds of the FOV and was treated as a contaminant. **Figure 2.9** shows a configuration of two sCMOS cameras inside the optical dome. **Table 2.1** shows the summary of the setting parameters and lenses used during the first winter season.

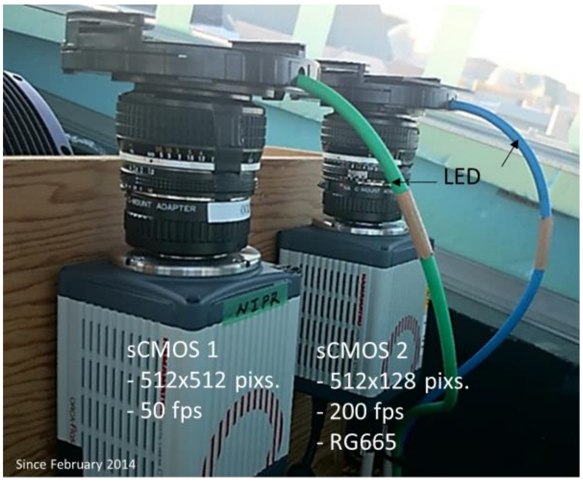

Figure 2.9: Two sCMOS cameras equipped with the identical NIKKOR 50 mm/F 1.2 lens and the LED light.

February 2014–April 2014 (First winter season)					
	Image size (pixels)	Sampling rate (fps)	Recording time (sec every min)	Lens	Filter
sCMOS 1	512 × 512	50	0–10	NIKKOR 50 mm/F 1.2	———
sCMOS 2	512 × 128 (sub-array)	200	0–10		RG665
DSLR camera D4	4928 × 3280	10 s interval (0, 10, 20, 30, 40, 50)		NIKKOR 8 mm/F 2.8 (Fisheye)	———

Table 2.1: List of setting parameters and used lens of each camera during the first winter season.

2.2.2 Second Winter Season (November 2014–April 2015)

During the first winter season, the recording time for the continuous observation was only 10 s of every minute. Data was not acquired for the remaining 50 s, even though the aurora remained and possibly dramatically changed its intensity or shape. The main purpose of the second winter season was to conduct continuous observation whenever the aurora appears. To achieve the continuous observation, I developed a new observational system using auroral automatic detection technique, which is described in Section 2.3. The new observational system was used for only sCMOS 1 with the sampling rate of 200 fps in order to avoid an overflow of data. The settings and the observational system of sCMOS 2 were basically the same as those of sCMOS 1 in the first winter; only the recording time was changed from 10 s to 30 s as a backup for sCMOS 1. For the all-sky imaging, a DSLR camera (D5300, Nikon) with a fisheye lens (SIGMA 4.5 mm/F 2.8) was installed. The time interval of the DSLR camera was 20 s. **Figure 2.10** and **Table 2.2** indicate the configuration and the setting parameters of the two sCMOS cameras and the DSLR camera during the second winter season.

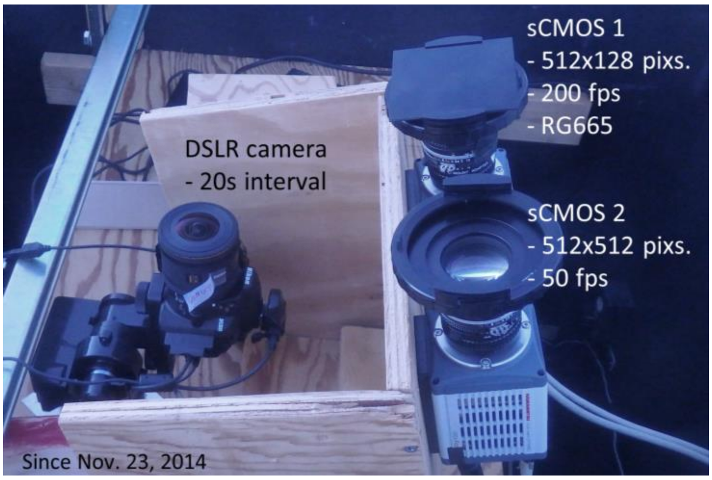

Figure 2.10: Configuration of the two sCMOS cameras with a NIKKOR 50 mm/F 1.2 lens and a DSLR camera (D5300, Nikon) with a fisheye lens (SIGMA 4.5 mm/F 2.8).

November 2014–April 2015 (Second winter season)					
	Image size (pixels)	Sampling rate (fps)	Recording time (sec every min)	Lens	Filter
sCMOS 1	512 × 128 (sub-array)	200	0–50 (Auto-detection system)	NIKKOR 50 mm/F 1.2	RG665
sCMOS 2	512 × 512	50	0–30		———
DSLR camera D5300	6000 × 4000	20 s interval (0, 20, 40)		SIGMA 4.5 mm/F 2.8 (Fisheye)	———

Table 2.2: List of setting parameters and used lens of each camera during the second winter season.

In this winter, the time synchronization system was also improved, since images contaminated by the LED could not be used for analyses. Instead of the LED, signals synchronized with the GPS were output, which were finally input into the sCMOS camera as external trigger signals to start the observation. Although PPS signals from the GPS are accurate, they can be used only when GPS satellite signals are captured. Two signals from the GPS were used to make an accurate external trigger signal: PPS signals, and minute signals, which are output at 0 s every minute. In order to keep the accurate output signals every minute, an electronic circuit, as shown in **Figure 2.11**, was designed by Koji Nishimura (NIPR) using an AND circuit between the PPS signal and the minute signal.

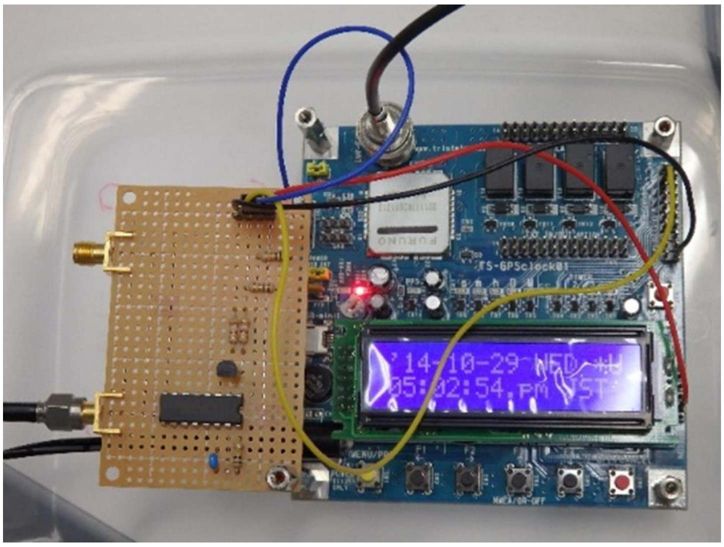

Figure 2.11: GPS (right part) and circuit board (left part) to make accurate external trigger signals every minute.

2.2.3 Third Winter Season (January 2015–April 2015)

The aim of the third winter season is to automatically operate both sCMOS 1 and sCMOS 2 by the auroral auto-detection system with the maximum recording time (60 s). To monitor the mesoscale auroral morphology, sCMOS 2 was equipped with a fisheye lens (NIKKOR 8 mm/F2.8). The FOV of sCMOS 2 corresponds to approximately 100° × 100° because the sensor size was smaller than the 35-mm full frame used for DSLR cameras. sCMOS 2 acquired the broad FOV images with the 512 × 512 pixel size at 40 or 80 fps. In order to capture the fine-scale morphology, sCMOS 1 was equipped with the usual narrow FOV lens (NIKKOR 50 mm/F 1.2) and acquired 512 × 512 pixel images at 80 fps. For the monitoring of the large-scale auroral morphology, THETA S (RICOH, 360° camera) was used, because an electronic shutter was adopted, and therefore the camera is not restricted by shutter numbers, in contrast to the DSLR camera with a mechanical shutter. THETA S also has an advantage in terms of cost than the usual DSLR cameras. The image obtained from THETA S every 20 s is used for the aurora auto detection.

During the last 1.5 months of the third winter season, the auto-detection system did not work due to a remote connection error between the control PC of THETA S and the other PCs. For this period, faster observations were conducted manually. Only partial images of 512 × 256 and 512 × 128 pixels were recorded at 160 and 320 fps, respectively, using the sub-array function. The sampling rates were designed to cover the typical cyclotron frequencies of three ion components (O^+, He^+, and H^+). **Figure 2.12** and **Table 2.3** indicate the configurations and the setting parameters of the two sCMOS cameras and THETA S during the third winter season.

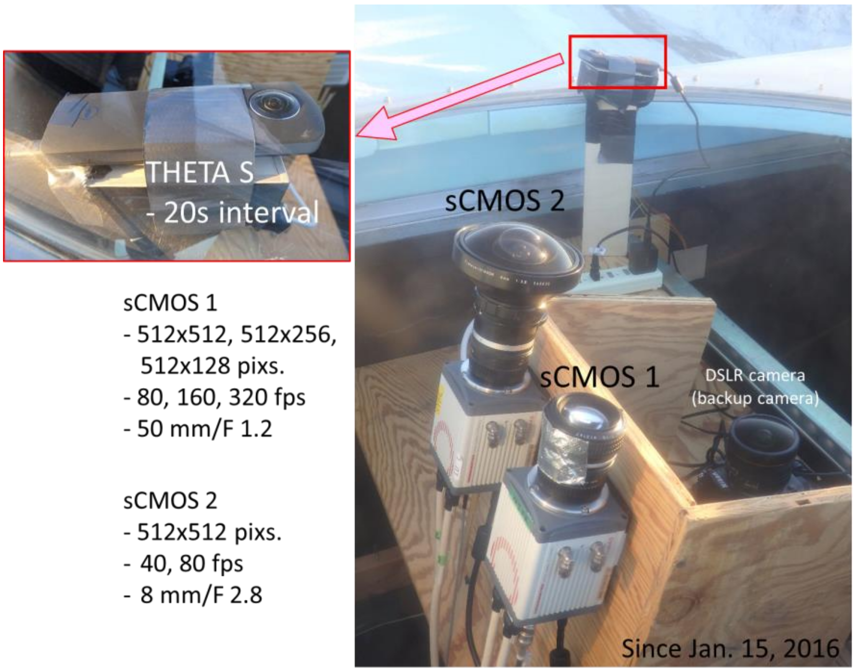

Figure 2.12: Configuration of two sCMOS cameras equipped with a fisheye lens (NIKKOR 8 mm/F 2.8) and a narrow FOV lens (NIKKOR 50 mm/F 1.2) and THETA S during the third winter season.

January 2016–April 2016 (Third winter season)

	Image size (pixels)	Sampling rate (fps)	Recording time (sec every min)	Lens	Filter
sCMOS 1	512 × 512 512 × 256 512 × 128 (sub-array)	80 160 320	0–60 (Auto-detection system)	NIKKOR 50 mm/F 1.2	———
sCMOS 2	512 × 512	40, 80		NIKKOR 8 mm/F 2.8 (Fisheye)	——
THETA S	5376 × 2688	20 s interval (0, 20, 40)		F2.0	——

Table 2.3: List of setting parameters and used lens of each camera during the third winter season.

The stability of the acquisition frame rate was improved in the winter of 2016 when compared with that of the former sCMOS camera systems presented in studies by *Kataoka et al.* [2015] and *Fukuda et al.* [2016]. A new circuit board, as shown in **Figure 2.13**, was designed by Herbert Akihito Uchida (NIPR) to generate trigger signals and release the shutter of the camera at a given fps, based on the GNSS time information. By using GNSS, the satellite signals from not only GPS, but also others such as GLONASS and GALILEO, are easily captured. Each camera system possessed its own circuit board with a micro processing unit (MPU) that was used to communicate with the PC, trigger the shutter signal, and control the LEA-M8F (u-blox) GNSS module. The GNSS module provides time information with a time pulse accuracy ≤20 ns and a frequency accuracy <5 ppb to synchronize the MPU.

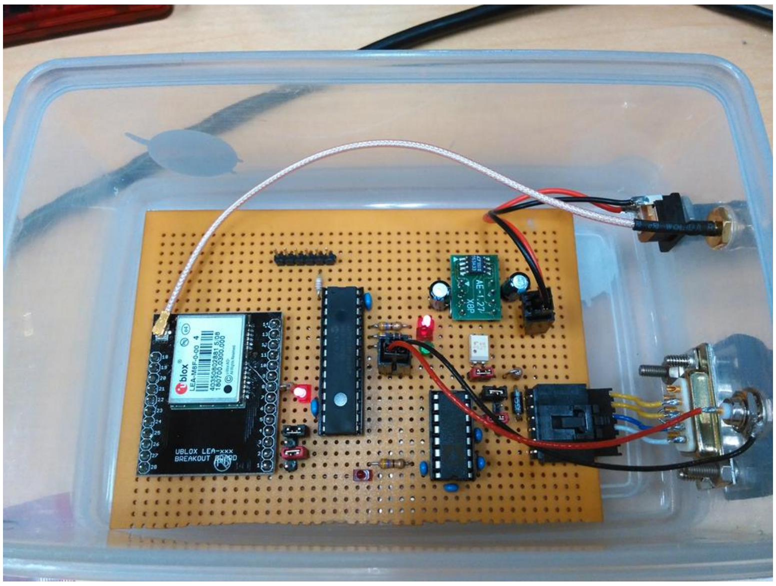

Figure 2.13: Circuit board to generate accurate trigger signals based on the GNSS time information.

2.3 Auroral Auto-detection System

Continuous auroral observations were difficult, since the high-speed fine-scale imaging acquires a huge amount of data in short time periods. I considered two ways to store only useful data in order to save the data storage medium. One is to automatically delete unnecessary data under certain conditions while operating the continuous observation. Since these operation processes are needed to be simultaneously executed on the control PC of sCMOS camera, the performance decrement of the data acquisition at the high-speed sampling rate cannot be avoided. The other way is to automatically control the observational system using an auroral automatic detection technique. An advantage of this system is that the performance of the high-speed imaging is not affected, since the auroral auto-detection is independently conducted on the control PC of the all-sky camera using color information. In this section, the overview and the performance evaluation of the new observational system with the auroral auto-detection technique are described.

2.3.1 System Overview

An auroral auto detection system was developed for self-regulation of the sCMOS camera. In order to detect the aurora, LIBSVM [*Chang and Lin*, 2011] is employed, which is a library for support vector machines (SVMs). SVMs are a popular machine learning algorithm used for classifications, and can differentiate data into two classes very well, which are scattered in n-dimensional space where n is number of parameters we have, by finding a hyperplane. In order to decide the right hyperplane, maximizing the distances between nearest data point of each class and the hyperplane is conducted.

In my study, three color information (red, green, and blue) obtained from the all-sky camera is used for auroral detection. In order to make a model, 582 color data of 194 all-sky images were used for training, which were acquired for approximately two weeks at PFRR after set up of the observational system and were classified into two groups in advance. **Figure 2.14** shows some examples of the data set for training of the auroral group (top panel) and non-auroral group (bottom panel). The auroral group consists of captured images of the discrete and the diffuse aurora with various auroral intensities and colors, because they were affected by the moon and the dusk and dawn sky. Although the auroras covered with clouds cannot actually be used for analyses, they are classified into the auroral group to prevent the dusky aurora, like the diffuse aurora, from being judged as part of the non-auroral group. The non-auroral group includes data of clear skies, cloudy skies, and snowy skies without the aurora.

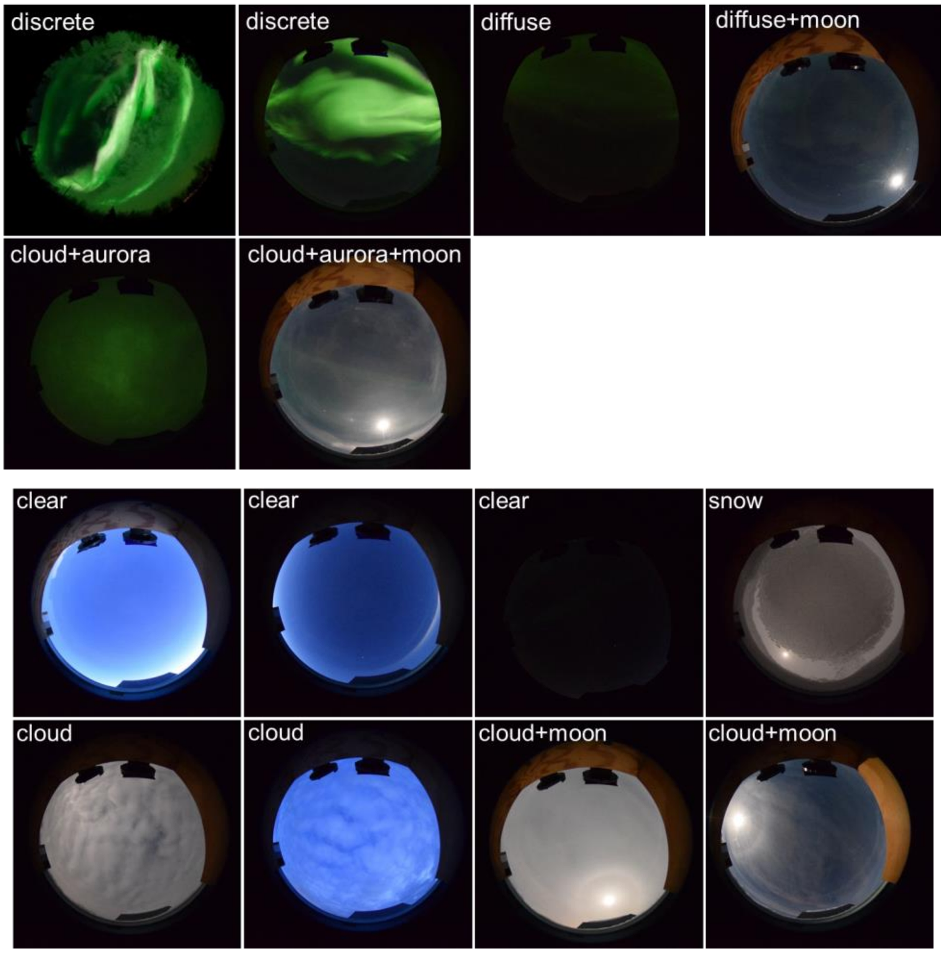

Figure 2.14: Examples of training data classified into two groups for the auroral detection: The auroral group (top panel) and non-auroral group (bottom panel).

The auroral detection was conducted every 20 s on the control PC of the all-sky camera in almost real time. A detection region is limited, which is 3 × 3 times larger than the usual FOV (14.8° × 14.8°) of the sCMOS camera centered at the magnetic zenith, in consideration of the auroral motions during the time interval of the all-sky camera as shown in **Figure 2.15**. Median values of each color calculated for the 3 × 3 regions are used as input data, and the detection results for each 3 × 3 region are output, which are obtained from the classification based on the model. If all the results show that the aurora does not exist, the control PC makes a STOP file in a particular directory of the sCMOS PC over a network. The STOP file is used to stop the data acquisition, and the presence of the file is checked by the sCMOS PC every 10 s. If one or more results show that the aurora exists, the STOP file is deleted, and then the observation is automatically entered in the standby state. **Figure 2.16** indicates an overview of the observation system, which links the control PC of the sCMOS camera with that of the all-sky camera via a switching hub.

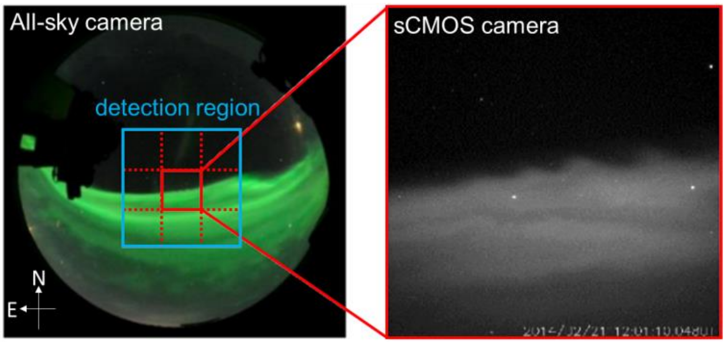

Figure 2.15: Snapshots of the all-sky camera (left) and the sCMOS camera (right) captured at almost the same time. The region used for the auroral automatic detection is indicated by a light blue square.

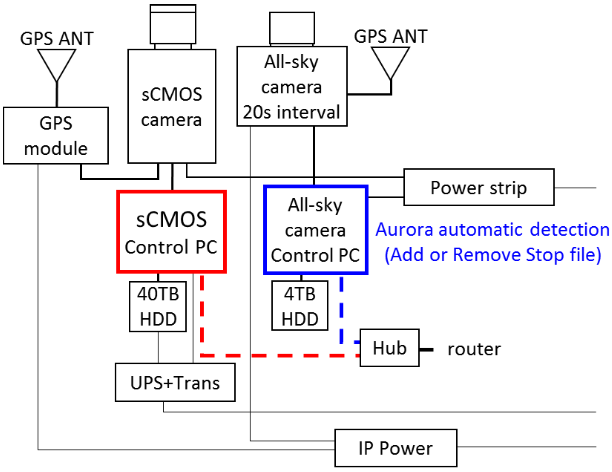

Figure 2.16: Schematic of the auroral automatic detection linking the control PC of the sCMOS camera with that of the all-sky camera via a switching hub.

The sCMOS camera records for a maximum of 60 s beginning from 0 s every minute depending on the results of the auroral detection, and then the raw data is saved every minute. If the STOP file exists at 0 s, the observation does not start during that minute. **Figure 2.17** presents an example of a process flow diagram for the automatic control of the sCMOS camera during 100 s. The trigger signal that is made by combining the PPS signal and the minute signal is output at 0 s every minute as shown in Section 2.2.2. The data acquisition of the sCMOS camera starts at times when the result of the auroral detection shows that the aurora exists, and then the trigger signal turns on. The data acquisition stops at times when the detection result shows the no aurora.

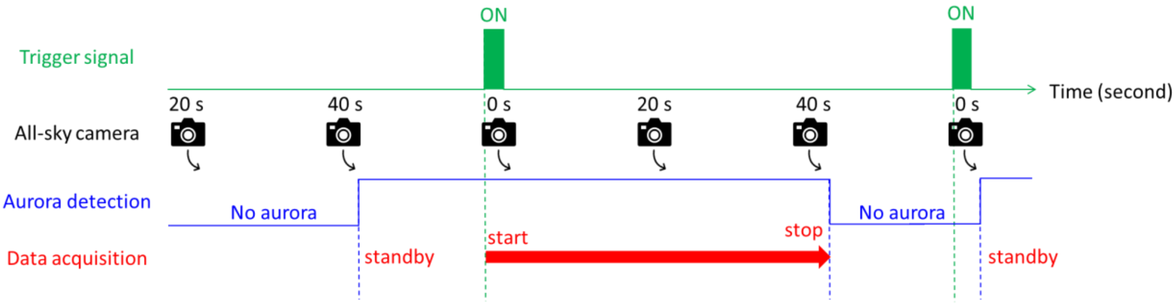

Figure 2.17: Process flow diagram for the automatic control of the sCMOS camera.

2.3.2 Performance Evaluation

The observational system implementing the auroral automatic detection was operated for four months in the second winter season and for two months in the third winter season. After using this system, the amount of data acquired during the second winter season was approximately 27 TB. In comparison with observation without the new system, the data amount would be 118 TB for four months with the same setting parameters. It is found that the data amount was decreased 75% by using the auroral auto-detection system.

For most of the observational period of the second winter season, however, the wrong region of the auroral detection was used, which was located at the east of the FOV of the sCMOS camera as shown in **Figure 2.18**. The mistake in the setting of the auroral detection region did not found for a long time since most of the detection results seemed to be correct. The reason is that the typical east-west extended auroral structures, such as the auroral arc and the auroral band, which appeared around the right detection region, fortunately overlapped with the wrong detection region and were often identified by the auto-detection. By using approximately 5000 all-sky images, the detection results taken in the wrong region were compared with those from the correct region. It was found that 90% of the former results corresponded to the latter results; this indicates that the setting error in the detection region did not have a fatal impact on the auroral detection.

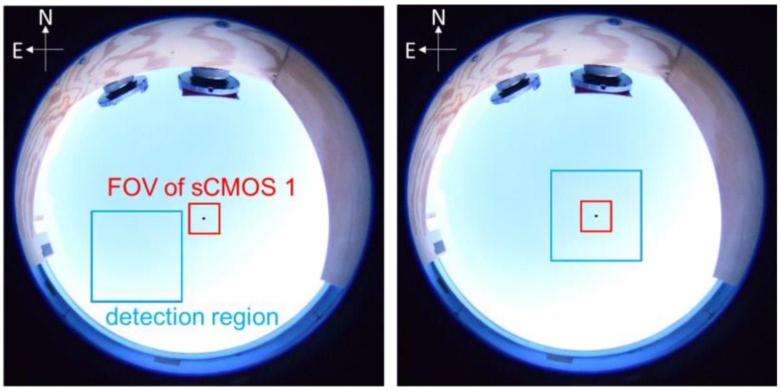

Before amendment After amendment

Figure 2.18: The false setting region of the auroral detection and the correct region after resetting.

In order to evaluate the performance of the auroral automatic detection, various images captured through the night for 7 days during the second winter season were randomly selected for unbiased evaluations, independent of the auroral activities and effects of the moon light, clouds, and snow. These images were judged by eye whether there is the aurora within the detection region or not, and then the results were compared to those by the auto-detection. **Table 2.4** shows the image numbers judged by the auroral automatic detection and by eye for the 16153 images. The ratio of the images with the aurora judged by the auto detection and by eye were approximately 39% (6257 = 3236 + 3021 images) and 21% (3375 = 3236 + 139 images), respectively. Many images judged as the aurora by the auto detection were too dark to identify by eye. This result is qualitatively consistent with the detection model, which is trained to acquire excessive data rather than risking missing actual data. An accuracy can be calculated as 80%, which is a ratio of the image number that both the auto-detection and eye give the same results (12993 = 3236 + 9757 images). The result shows that the auroral auto detection has enough performance to identify the aurora.

		Eye	
		Yes	No
Auto detection	Yes	3236	3021
	No	139	9757

Table 2.4: Results of image numbers judged by the auroral automatic detection and by eye.

2.3.3 Possibility of Auroral Auto-detection

The new observational system with the auroral automatic detection enabled the continuous high-speed fine-scale imaging observation for the first time. The system can record data efficiently, and is also favorable for the isolated observatory where people cannot visit regularly. The auroral auto-detection technique is helpful for event search, since the unnecessary data is removed in advance. The technique itself accelerates to statistical survey of the time, place, and duration of the auroral appearance. The statistical comparative studies between these parameters and associated phenomena with the auroral activity, such as the solar activity, the plasma sheet variation, the geomagnetic activity, and the ionospheric responses, would provide important clues to elucidate the auroral dynamics as a coupling process in the solar-terrestrial system.

Moreover, the auroral auto-detection system is useful to monitor the auroral activity in the night sky and is helpful to automatically operate other observational systems associated with the auroral phenomena, in order to start the observation or to change the observational mode. We hope our new approach to automatically and actively control the observation system itself would be an important start point for further advanced new styles of observations. Nowadays, advanced sciences using the artificial intelligence are progressing, and combined studies using the auroral auto-detection and the AI would explosively accelerate the auroral physics not only on the identification but also on the complicated real-time imaging analyses, such as the classification or the finding of new types of aurora, in the future.

3 Basic Property of Flickering Aurora

Many previous studies have reported that flickering auroras often occur just before and during the auroral breakup. However, there has also been a few reports on flickering auroras that were not associated with a breakup [e.g., *Berkey et al.*, 1980; *Kunitake and Oguti*, 1984; *McHarg et al.*, 1998; *Sakanoi and Fukunishi*, 2004]. *Sakanoi and Fukunishi* [2004] pointed out that the flickering occurrence rate is not necessarily proportional to the auroral luminosities. The difference between auroras with and without a flickering structure has been remained unclear. The modulation ratio of the flickering amplitude has been reported to be 10%–20%, the origin of this ratio is not yet understood. In this chapter, we aim to elucidate the necessary conditions for a flickering aurora based on a statistical study of the occurrence property and clarify the meaning of the flickering amplitude.

3.1 Occurrence Property

3.1.1 Analysis

For the statistical analysis, the sCMOS 2 data of the second winter season were used, which were recorded as 512 × 512 pixel images at a sampling rate of 50 fps from 0 s to 30 s of every minute, as described in Section 2.2.2, because the sCMOS 2 camera was more appropriate for identifying the flickering aurora event than the sCMOS 1 camera, which had one fourth of the FOV of the sCMOS 2 camera. **Figure 3.1** shows the *Dst* index and an overview of the flickering appearance from December 2014 to February 2015. The blue arrows are plotted on days when the flickering aurora was manually identified (an automatic detection technique for the flickering aurora is described in the next paragraph), and the orange arrows indicate storms that developed with values of less than -50 nT as a reference for the disturbance of the magnetosphere. The dark gray rectangles show nights when there were no auroras or only weak auroras were observed with emissions of less than approximately 5 kR at 557.7 nm. The bright gray rectangles show nights when the aurora was contaminated by clouds or snow on the optical dome. Nights with a full moon are indicated by yellow circles. In this study, even though many flickering auroras were identified in the data contaminated by moonlight, these were not used for analyses because the auroral luminosities were misleading. Six of the 18 nights on which flickering auroras were observed were utilized for the statistical analysis after removing the data containing moonlight. The dates and time periods of these six nights are summarized in **Table 3.1**.

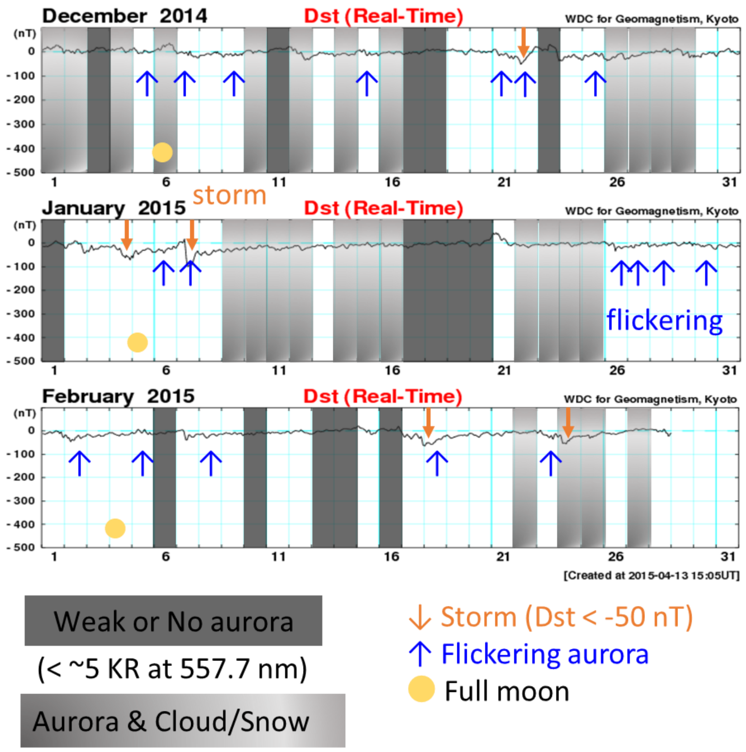

Figure 3.1: *Dst* index and overview of observations from December 2014 to February 2015 during second winter season. The dark gray and bright gray rectangles indicate nights when there were no auroras or weak auroras, and auroras contaminated by clouds or snow, respectively. The blue arrows and orange arrows are plotted on days with flickering and storms (*Dst* index < -50 nT), respectively.

Date	Period	Description
December 15, 2014	0750–0859 UT	Breakup at 0825 UT
December 22, 2014	0300–1420 UT	
December 25, 2014	1300–1716 UT	Breakup at 1335 UT
January 27, 2015	1050–1400 UT	Brightening at 1050 UT
February 18, 2015	0530–1149 UT	
February 23, 2015	0700–0843 UT	Brightening at 0831 UT

Table 3.1: Dataset used for the statistical analysis.

For the statistical investigation of flickering auroras, the time and place that the flickering appeared were automatically detected in the following way. As a first step, 512 × 512 pixel images of the auroral intensity were reduced down to 128 × 128 pixel images by 4 × 4 binning, and a 2D median filter with a 3 × 3-pixel width was used on each image to reduce the noise from stars. To extract the auroral luminosity of the non-flickering background aurora, the data were smoothed using a boxcar average width of 0.2 s (10 frames) for each pixel. The smoothed images resulted in low-pass filtered images with a cut-off frequency of 5 Hz. The flickering component was obtained from the difference between the original image and the low-pass filtered image, and resulted in high-pass filtered images with a cut-off frequency of 5 Hz. In order to calculate the flickering frequency, a 1D Fourier transform analysis was employed. The Fourier transform $\mathcal{F}(\omega)$ of a function $f(t)$ is denoted by

$$\mathcal{F}(\omega) = \int_{-\infty}^{\infty} f(t) e^{-i\omega t} dt,$$

and $f(t)$ is determined by $\mathcal{F}(\omega)$ through the inverse transform given by

$$f(t) = \int_{-\infty}^{\infty} \mathcal{F}(\omega) e^{i\omega t} d\omega.$$

In the case of a discrete N-point signal, a discrete Fourier transform (DFT) can be written as

$$F_k = \sum_{n=0}^{N-1} f_n \, exp(-i\frac{2\pi kn}{N}), k = 0, 1, 2, \cdots, N-1.$$

A fast Fourier transform (FFT) analysis is an algorithm for the rapid computation of the DFT. An FFT analysis using a 1.0 s window was performed for the high-pass filtered images, and the typical frequencies were calculated as a peak frequency with a maximum power spectral density. The calculations were repeated for each pixel (128 × 128 pixel) every 0.2 s for the 30 s dataset. The flickering signature is characterized by a spatial distribution of flickering patches with frequency coherence. The 2D frequency map was divided into 32 × 32 small regions, and an average frequency and a standard deviation were calculated at each small region.

For the statistical study, the criteria of the flickering aurora were empirically derived as follows: the average frequency was larger than 6.5 Hz, and the standard deviation was less than 4.5 Hz. The final results of the automatic detection were obtained after removing erroneous decisions using the 2D median filter with the 3 × 3-region width. **Figure 3.2** shows the results of the automatic detection of the flickering aurora, where the area of the flickering aurora is indicated by red dots on the original image (upper left panel) and white dots on the average frequency map (bottom left panel) and standard deviation map (bottom right panel). In addition to the results of the automatic detection of the flickering aurora, the average intensity of the background non-flickering aurora was also obtained with the same spatial and temporal resolutions.

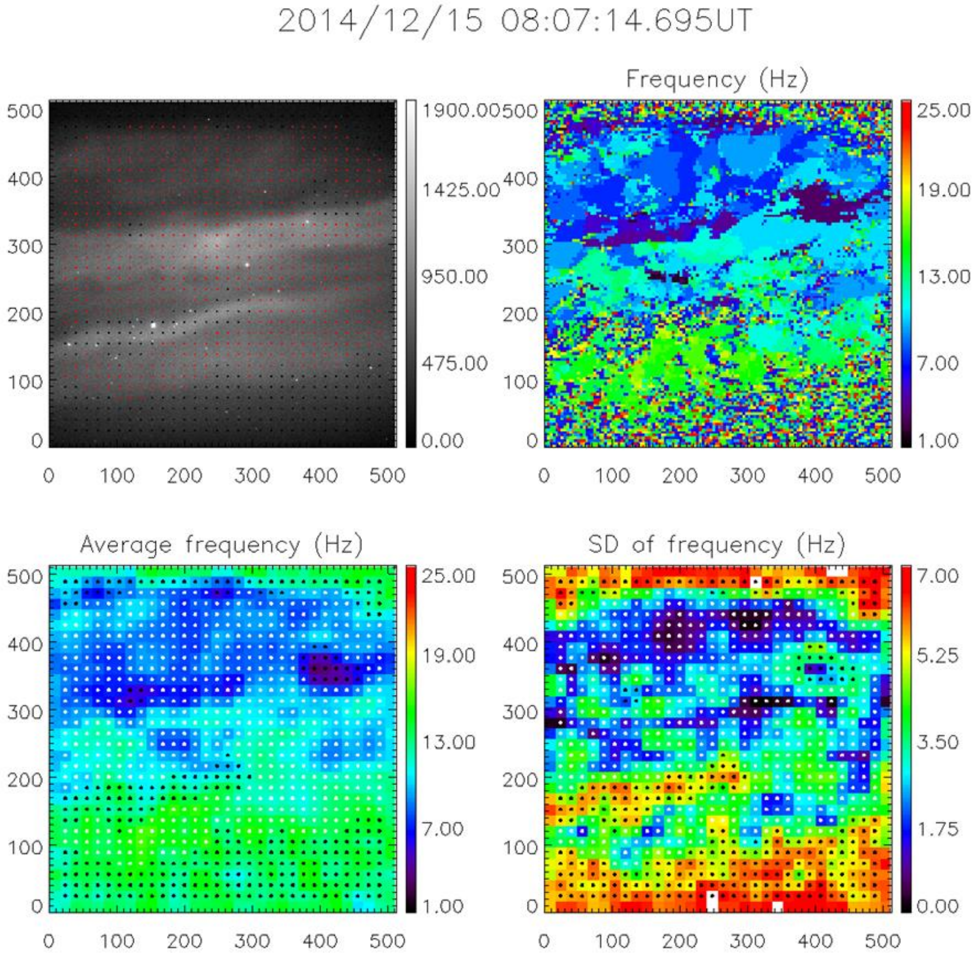

Figure 3.2: Results of automatic detection of flickering aurora plotted on original image using red (flickering) and black (non-flickering) dots (upper left panel). A 2D-frequency map calculated from the 1D FFT analysis (upper right panel). 2D-maps of the average frequency and standard deviation calculated from the frequency map, which was finally divided into 32 × 32 small regions (bottom panels). The results of the automatic detection are also plotted on the bottom panels using white (flickering) and black (non-flickering) dots.

In order to investigate the micro-scale auroral activity, the optical flow was calculated using a Fourier local correlation tracking (FLCT) technique [*Fisher and Welsch*, 2008]. The basic concept of the LCT technique consists of three advanced operations. First, a window function is applied to the input images to de-emphasize image regions that are far away from the pixel of interest. Second, a cross-correlation function between two images is computed. Third, a peak for the cross-correlation function is found. In the FLCT method, the window function uses a 2D Gaussian filter with width σ, which is a free parameter, centered at pixel location (x_i, y_j). The resulting images, which are called "sub-images" S_1 and S_2, are described as follows:

$$S_1^{(i,j)}(x,y) = I_1(x,y)e^{\frac{-\left[(x-x_i)^2+(y-y_j)^2\right]}{\sigma^2}}$$

$$S_2^{(i,j)}(x,y) = I_2(x,y)e^{\frac{-\left[(x-x_i)^2+(y-y_j)^2\right]}{\sigma^2}},$$

where $I_1(x,y)$ and $I_2(x,y)$ are two input images taken at two different times t_1 and t_2. The cross-correlation function $C^{i,j}$ of two sub-images at the (i, j)th pixel is defined by

$$C^{i,j}(\delta x, \delta y) = \iint dxdy\ \ S_1^{i,j^*}(-x,-y)\, S_2^{i,j}(\delta x - x, \delta y - y)$$

After finding the shifts δx and δy that maximize $C(\delta x, \delta y)$, the velocities at the (i, j)th pixel are determined to be $v_x = \delta x/\delta t$ and $v_y = \delta y/\delta t$ using the time difference between the two images $\delta t = t_2 – t_1$. In the FLCT method, a convolution theorem is used for computing $C(\delta x, \delta y)$ using the Fourier transforms. When $\mathcal{F}$ stands for the Fourier transform and the relations of S_1 and S_2 are given by $\mathcal{F}(S_1) = s_1(k_x, k_y)$ and $\mathcal{F}(S_2) = s_2(k_x, k_y)$, respectively, the cross-correlation function can be written as follows:

$$C^{i,j}(\delta x, \delta y) = \mathcal{F}^{-1}(s_1^* s_2),$$

where $\mathcal{F}^{-1}$ stands for the inverse Fourier transform. In order to find the peak of $f(\delta x, \delta y) = |C^{i,j}(\delta x, \delta y)|$ at the sub-pixel (less than 1 pixel) resolution, we used a Taylor series expansion of $f(\delta x, \delta y)$ to the second order about the point (x_m, y_n), where a pixel at the largest value of f, and a second-order finite difference method were used. These steps were repeated for all of the pixels.

The FLCT analysis was performed for the low-pass filtered images with a 128 × 128-pixel size every 0.2 s (10 frames), which were filtered using the Gaussian function with $\sigma = 6$ pixels. Using the obtained optical flow vector $\boldsymbol{v}$, a vorticity perpendicular to the flow motion Ω_z was calculated as follows:

$$\Omega_z = (\nabla \times \boldsymbol{v})_z = \frac{\partial v_y}{\partial x} - \frac{\partial v_x}{\partial y},$$

where x and y indicate the east-west and north-south directions, respectively. To investigate the correlation between the flickering occurrence and the background flow motion, the averaged flow speed and maximum vorticity were calculated at each 32 × 32 small region. **Figure 3.3** shows the results for the optical flow plotted on the original image and the vorticity calculated from the flow velocity.

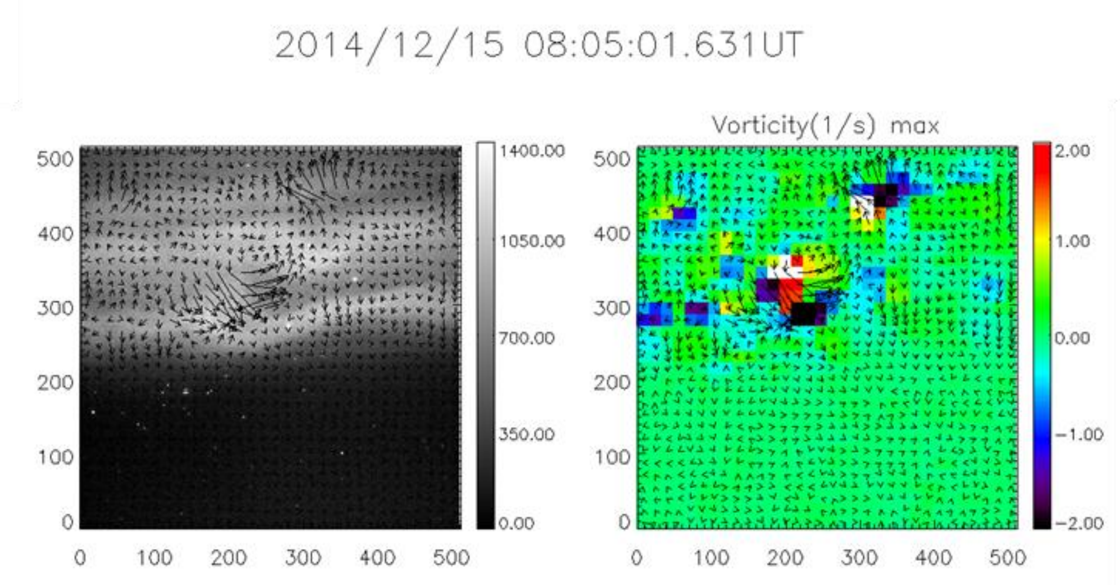

Figure 3.3: Results for flow velocity obtained using FLCT analysis and vorticity calculated from velocity field.

3.1.2 Observations

Figure 3.4 shows the occurrence rates of the flickering aurora in relation to the background of the auroral intensity, the flow speed, and the vorticity, which were summed up for six nights of data. The vertical axis of each upper panel shows the number of points where the auto-detection of the flickering aurora was conducted. The black line indicates the total number of points, and the red line indicates the total number of points where the flickering aurora is detected. Each bottom panel shows the occurrence rate, which is the ratio of the red to black lines.

It is found that the occurrence rate shows the complex variation with respect to the background auroral intensity. The flickering occurrence rate basically increases with the auroral intensity up to 1000 count of the background auroral intensity, and it reaches the constant value corresponding to approximately 50% for the range of 1000–3000 count. It reduces to ~10% at the range of 3000–5000 count, and it finally increases over 5000 count. In order to clarify the cause to produce such a complex variation of the occurrence rate, we focus on each occurrence property obtained at each night and discuss the situation to cause the occurrence rate variation. Three examples are represented from the following paragraphs, which clearly show the differences. It is also found that, on the other hand, the occurrence rates do not depend on the flow speed or the vorticity, and they are approximately 30%–40% regardless of the activity of the background non-flickering aurora.

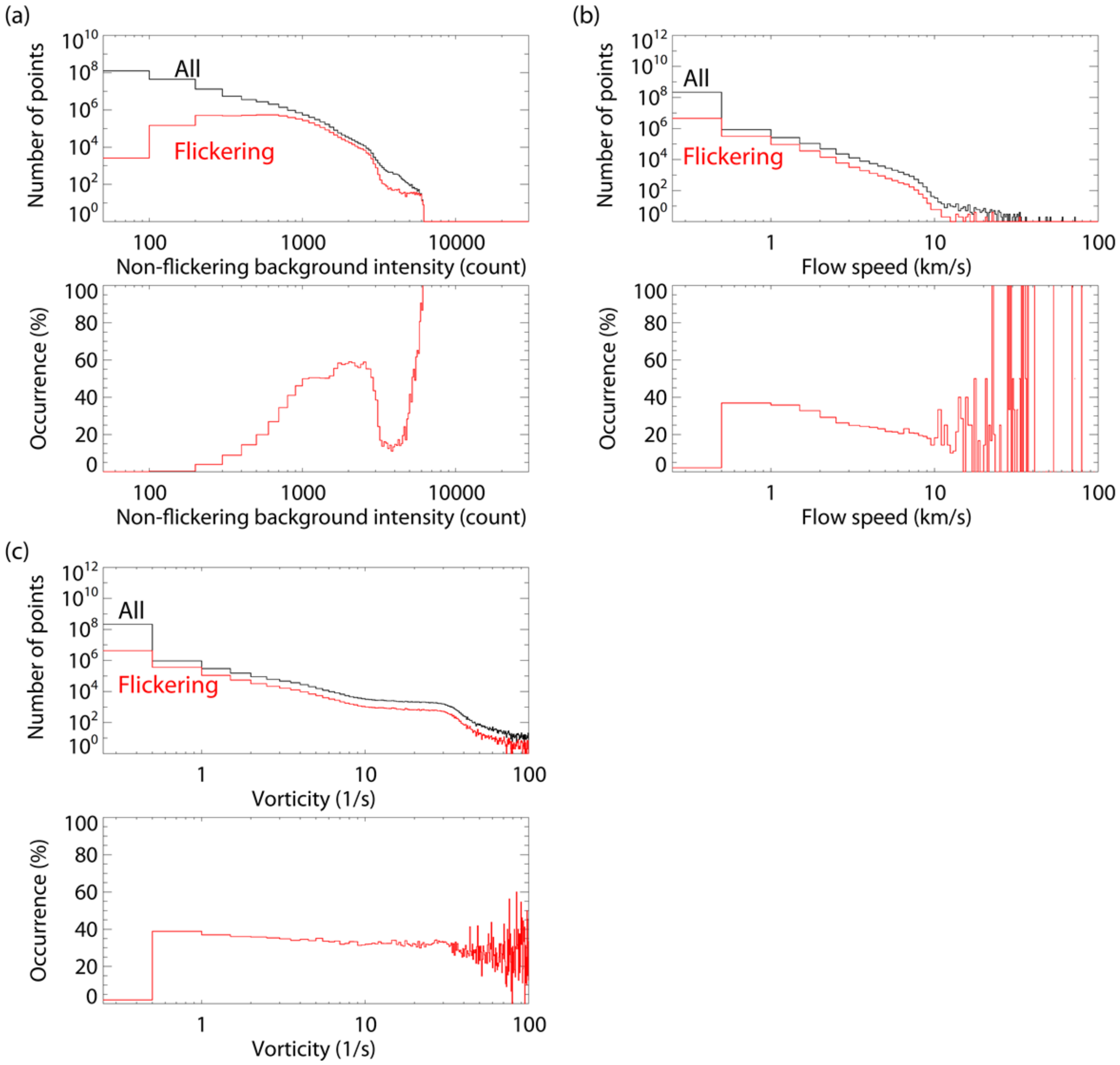

Figure 3.4: Occurrence rates of flickering aurora in relation to background of auroral intensity (a), flow speed (b), and vorticity (c), which were obtained from auto-detection of flickering aurora and summed up for six nights of data. The black lines show the total number of points, and the red lines show the total number of points where the flickering aurora is detected.

The first example is characterized by a typical breakup event observed on December 15, 2014, when the geomagnetic activity was quiet, and the *Dst* index slightly decreased to –16 nT at 11 UT. The equatorward motion of the arcs started at ~0730 UT, and the auroral breakup occurred at 0825 UT during the expansion phase of a substorm with an *AE* index of ~900 nT. The flickering aurora started to appear within the equatorward moving arcs at 0800 UT even before the onset of the breakup and was almost continuously observed until the breakup. The *Dst* index, *AE* index, and auroral activities along a north-south meridian line over PFRR observed at four different wavelengths are presented in **Figure 3.5**. The auto-detection was conducted for data observed from 0750 to 0859 UT to avoid contamination by moonlight and clouds.

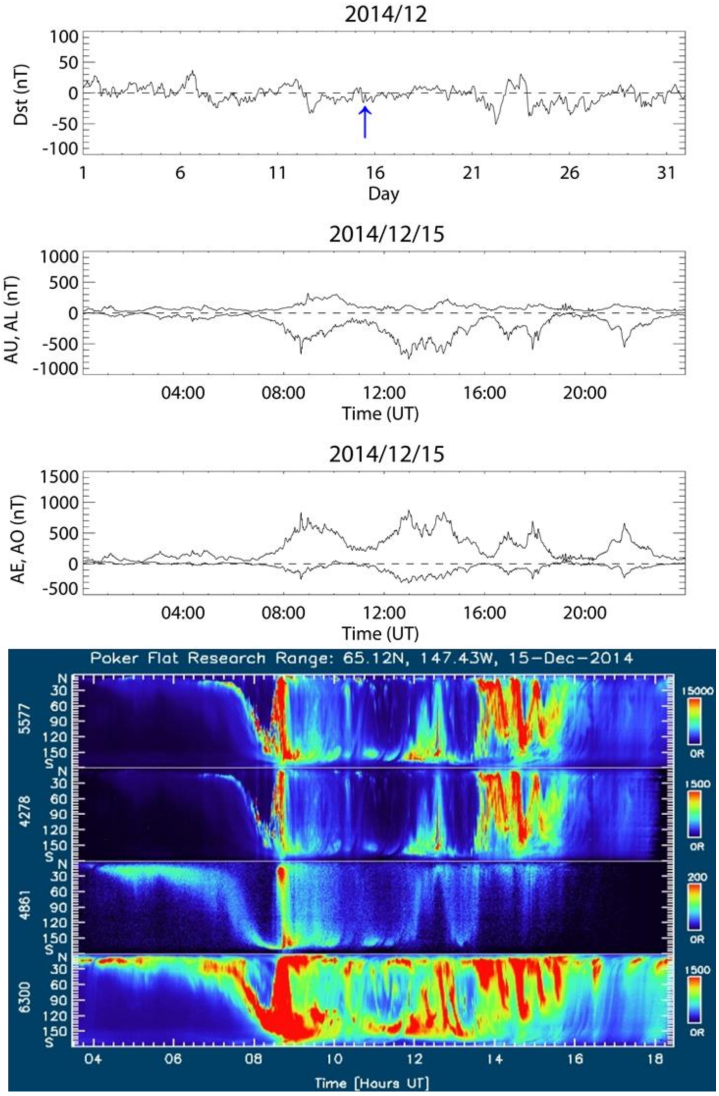

Figure 3.5: *Dst* index, *AE* index, and auroral activities along a north-south meridian line over PFRR observed on December 15, 2014.

Figure 3.6 shows some detail time profiles for 1-h time period from 0750 UT when the auto-detection was conducted, and red dots represent the time when the flickering aurora was identified. **Figure 3.6a** shows the *AE* index. **Figure 3.6b** shows the median intensity values for 30-s data of the non-flickering background aurora indicated by black points and the flickering aurora indicated by red points, and the error bars show their minimum and maximum values. It is found that the flickering aurora tends to occur within a bright aurora. **Figure 3.6c** indicates median values of the peak flickering frequency for 30-s data, and the error bar indicates 1σ. It is found that the peak flickering frequency is gradually increased during the time period before the breakup onset from <10 Hz to 20 Hz. The peak frequency variation appears to increase after 08:20 UT, although we cannot discuss the variation in more detail because the flickering aurora is intermittently detected after that time. **Figure 3.6d** shows the occurrence rate of the flickering aurora for 30-s time period, which is calculated from the results of the flickering auto-detection. If the flickering aurora was continuously detected all over the FOV for 30 s, the occurrence rate is corresponding to 100%.

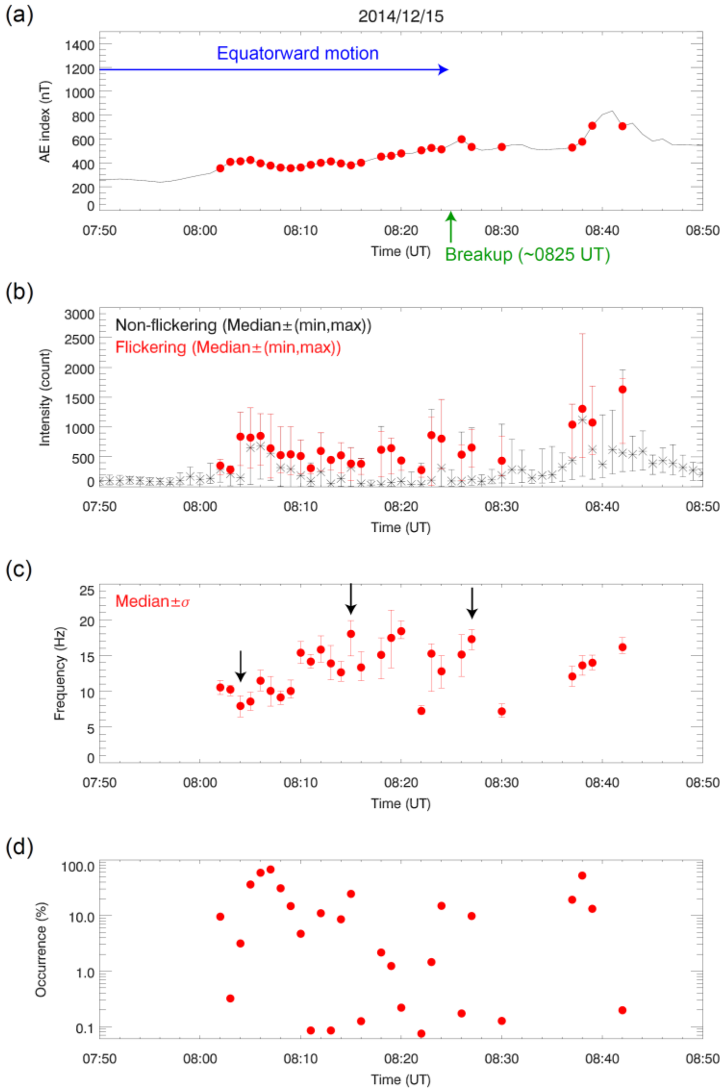

Figure 3.6: Detailed time profiles of (a) *AE* index, (b) auroral intensity of the non-flickering background and the flickering aurora, (c) flickering frequency, and (d) occurrence rate where flickering aurora was detected. The red dots are only plotted at the times when the flickering aurora appeared.

In order to show the property of the flickering frequency in more detail, three examples of the time profiles with 0.2-s value of the peak frequency and the flickering width for 30-s are demonstrated in **Figure 3.7**. Top panel of each figure indicates the spatial median values of the flickering intensity with the error bar of the minimum and maximum intensities. Middle and bottom panels show spatial median values of the flickering frequency and the frequency width with the error bar of 1σ, respectively. In this study, the frequency width is defined as a spectrum width between two frequencies, which correspond to the two nearest valleys of the power spectrum density from the peak frequency. **Figure 3.7a** represents the time period of 20 min before the breakup onset and shows that the peak frequency stays at around ~ 10 Hz. After ~10 min later of that time, the peak flickering frequency is up to 20 Hz and gradually decreases to ~10 Hz for 30 s as shown in **Figure 3.7b**. **Figure 3.7c** represents the time after a few min of the breakup, the peak frequency varies within 15–20 Hz. It is also found that the frequency width is often narrow and is approximately constant at ~5 Hz as shown each figure during the time interval of this event.

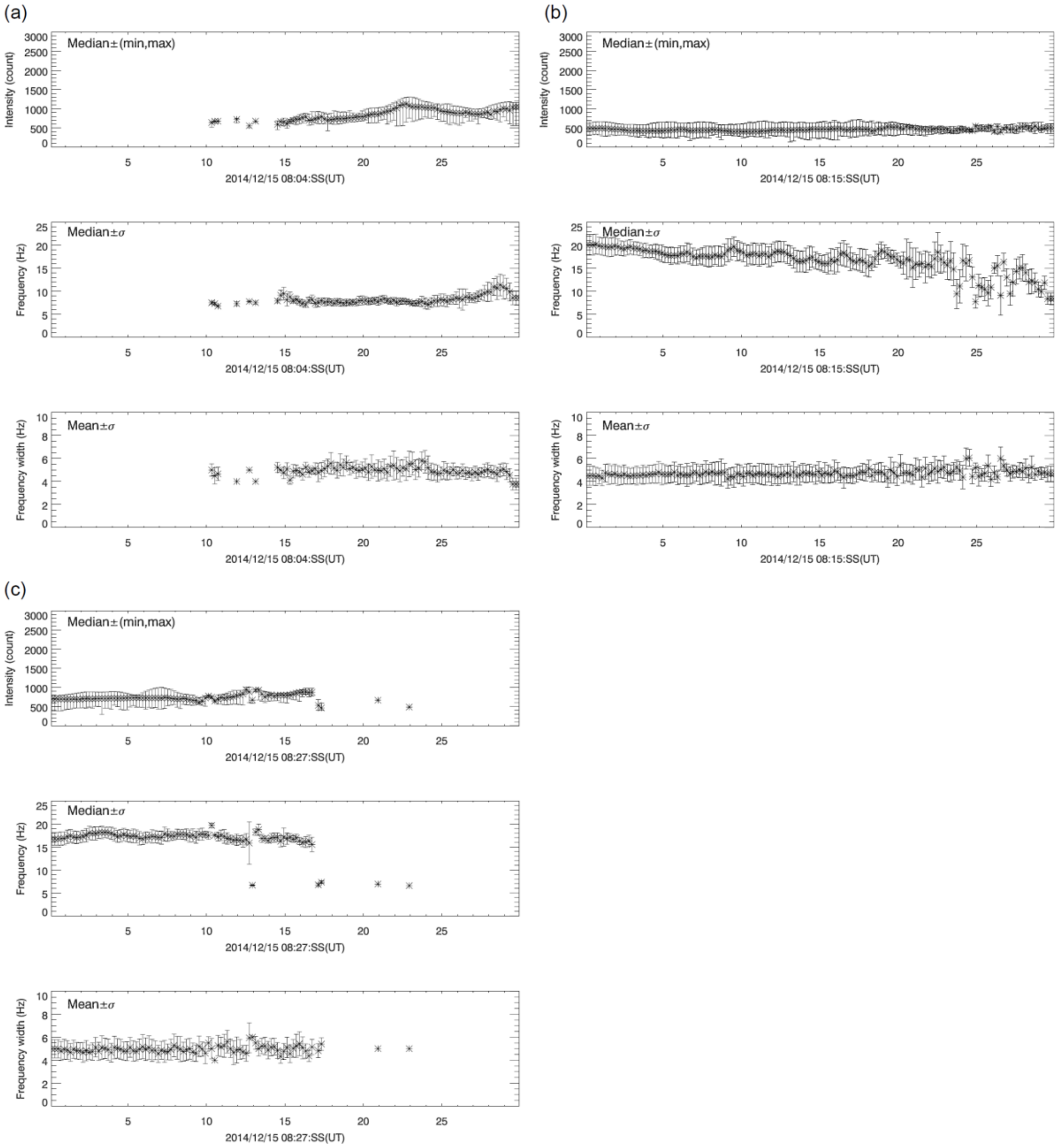

Figure 3.7: Time profiles of the flickering intensity (top), the flickering frequency (middle), and the frequency width (bottom) for 30-s from 08:04 UT (a), 08:15 UT (b), and 08:27 UT (c), respectively.

Figure 3.8 shows that the occurrence rate of the flickering aurora calculated from the auto detection using 70-min data. The occurrence rate tends to simply increase as the background aurora intensity increases, although it flattens at the intensity range of 1000–2000 count. The flatted occurrence rate is caused by the bright band aurora without the flickering modulation, which is listed in **Table 3.2** as mentioned later. The auroral structures with the flickering modulation were almost multiple arcs in this event.

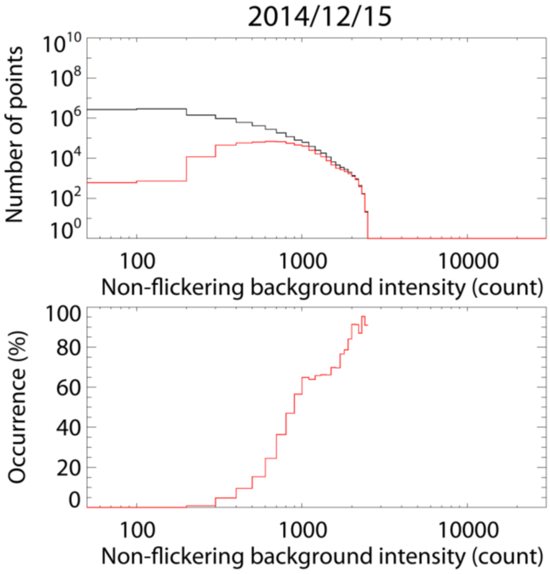

Figure 3.8: Occurrence rate of flickering aurora during 0750–0859 UT on December 15, 2014.

The second example was observed during the recovery phase of a storm that occurred on December 22, 2014, which had a *Dst* index value of –51 nT. On this day, although no typical substorm occurred, abrupt auroral brightening repeatedly appeared at intervals of approximately 3 hours, as shown in the middle panel of **Figure 3.9**. The auto-detection of the flickering aurora was conducted from 0300 to 1420 UT. The pulsating auroras began to appear after approximately 1100 UT, and the auto-detection often mistook the spatial variations of a pulsating patch for flickering modulations, as shown in Chapter 5 in more detail.

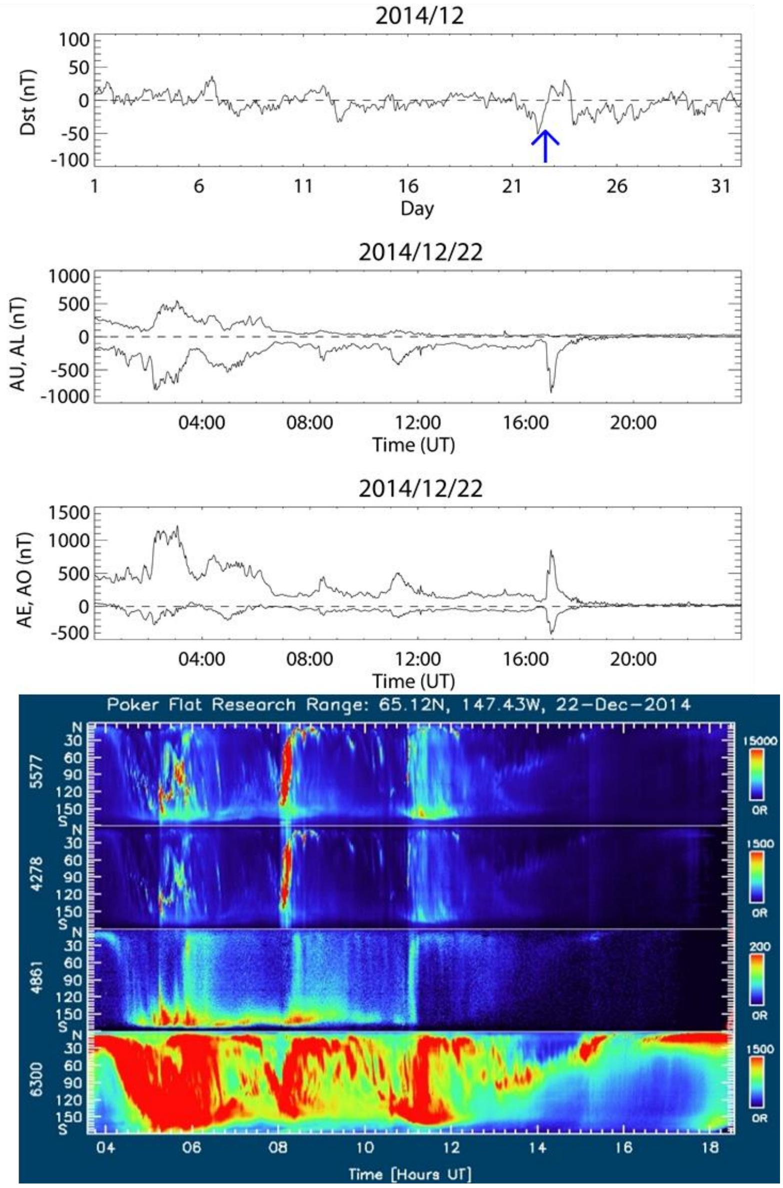

Figure 3.9: *Dst* index, *AE* index, and auroral activities along north-south meridian line over PFRR observed on December 22, 2014.

Figure 3.10 presents the auto-detection results for the flickering aurora over a 1 hour period from 0445 UT. There were a few events where the maximum intensity was larger than a count of 1000, although they did not have the flickering structure.

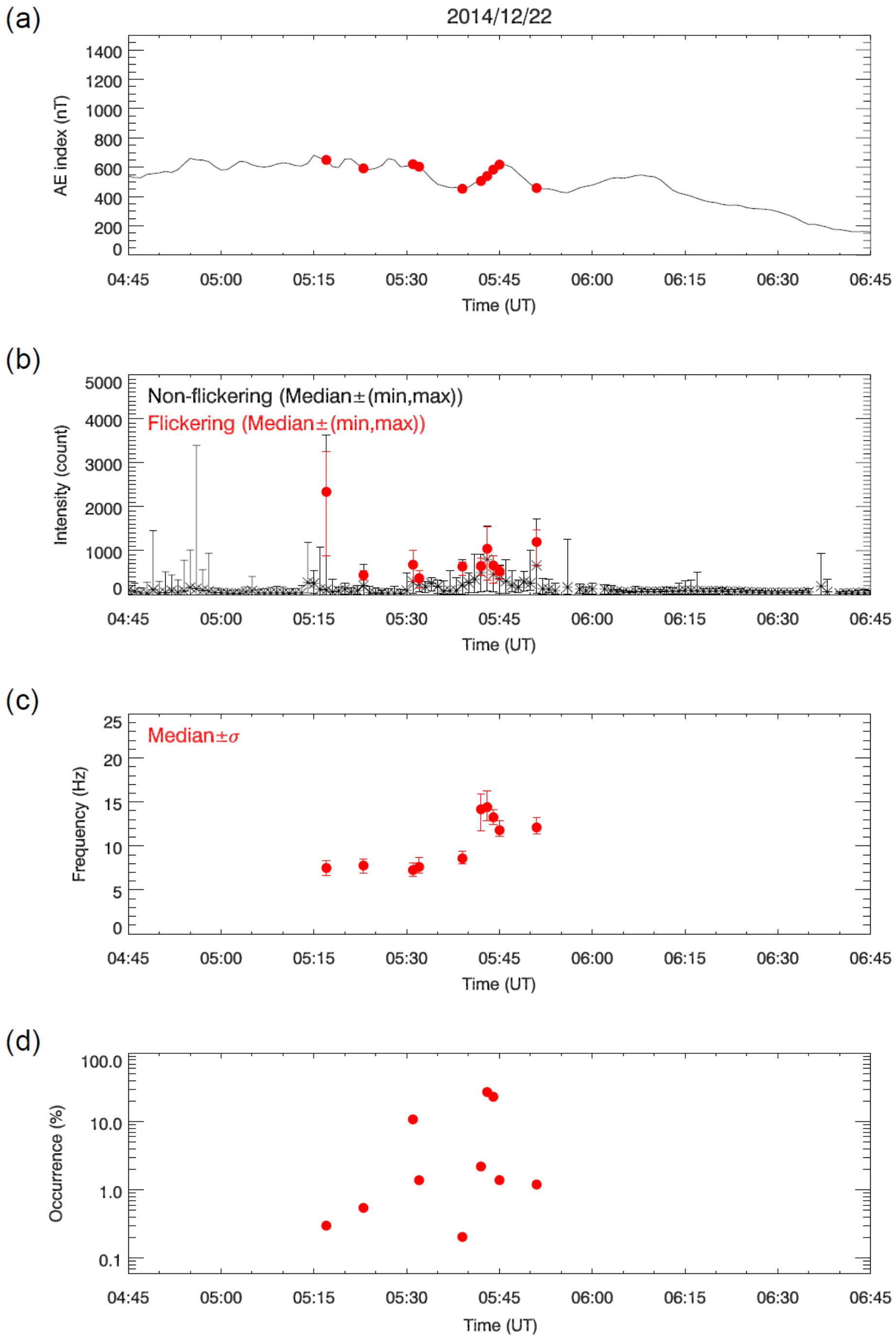

Figure 3.10: Detailed time profiles of *AE* index, non-flickering background auroral intensity, flickering frequency, and total number of points where flickering aurora was detected. The format is the same as that of **Figure 3.6**.

Figure 3.11 shows the occurrence rate of the flickering aurora during 0300–1420 UT on December 22, 2014. Although the occurrence rate increases up to approximately 70% with the non-flickering background auroral intensity, it decreases at a count greater than 3000 because of the existence of bright non-flickering auroras.

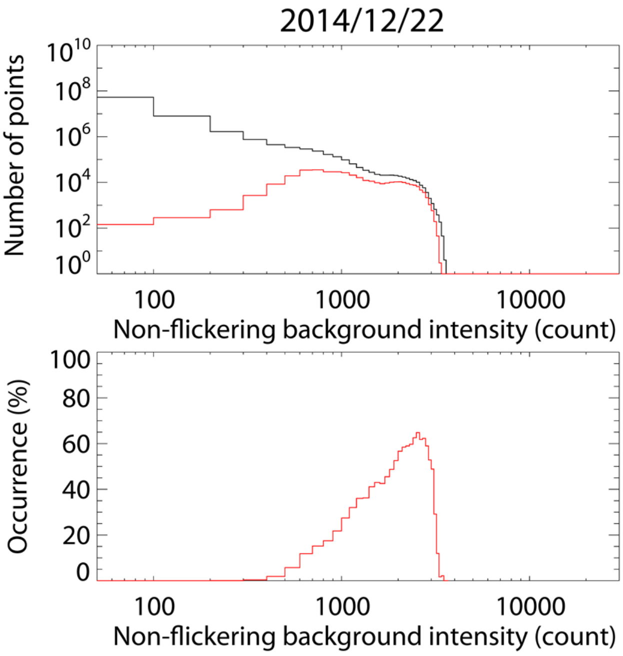

Figure 3.11: Occurrence rates of flickering aurora during 0300–1420 UT on December 22, 2014.

Figure 3.12 presents two events where bright auroras without the flickering structure were observed at 0456 UT and 0556 UT. The upper panels show snapshots, and the bottom panels show stack plots of the auroral arc intensities and time variations of the arc widths in directions normal to the arcs. When the arc width is defined by the half maximum full-width, both arc widths are less than 10 km, and their median values for 30 s are 4.5 km and 3.7 km, respectively. These events are characterized by bright isolated arcs, and the left event shown in **Figure 3.12** especially causes the depletion of the occurrence rate of the flickering aurora at a count greater than 3000 as shown in **Figure 3.11**.

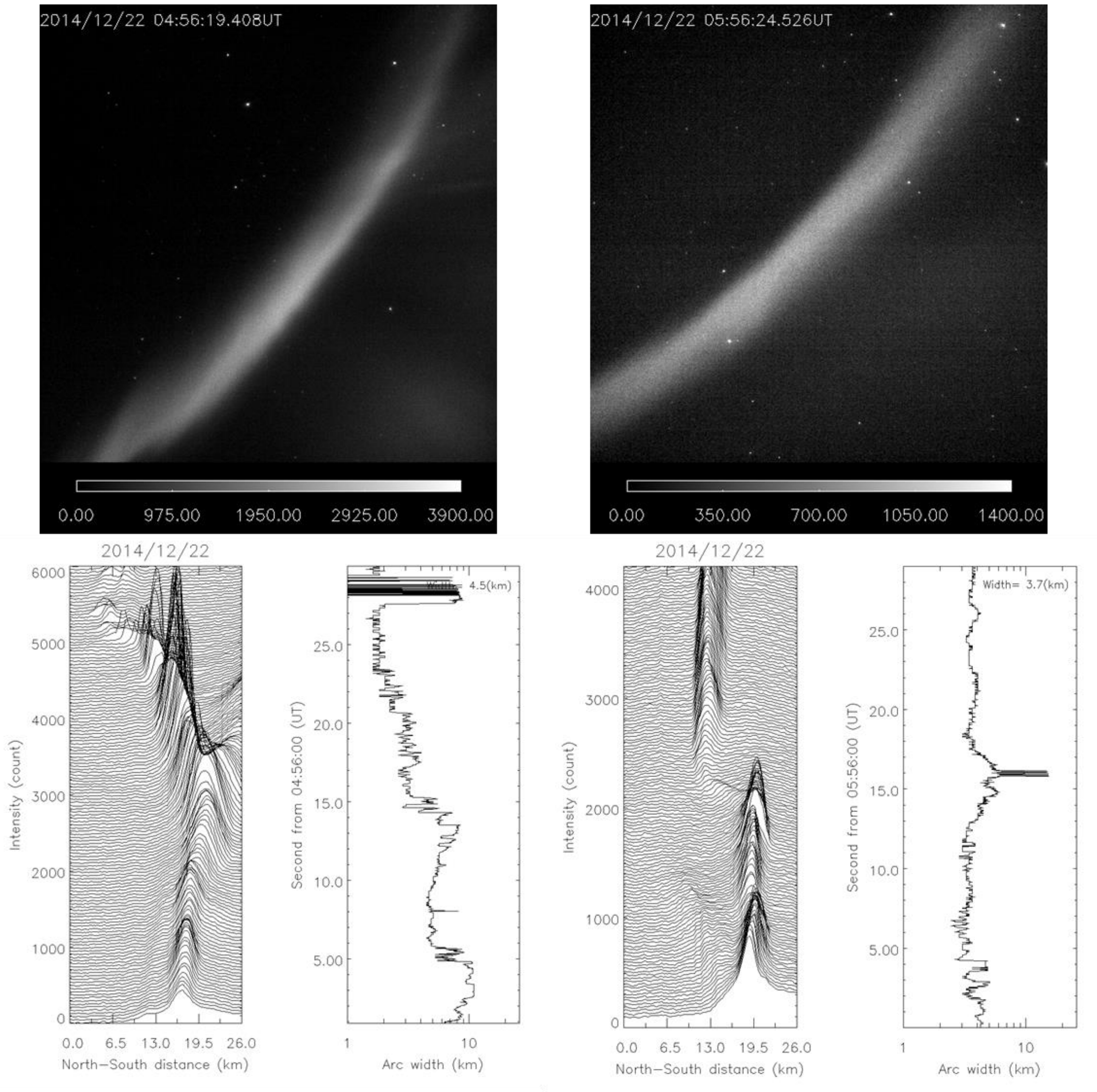

Figure 3.12: Two examples of non-flickering bright auroras. The upper panels are snapshots of the arcs. The bottom panels are stack plots of the arc intensities and the time variations of the arc widths normal to the arcs.

The third event was observed during a quiet time with a minimum *Dst* index of –29 nT on December 25, 2014, and a breakup, which occurred at 1335 UT but did not continue for a long time, as shown in **Figure 3.13**.

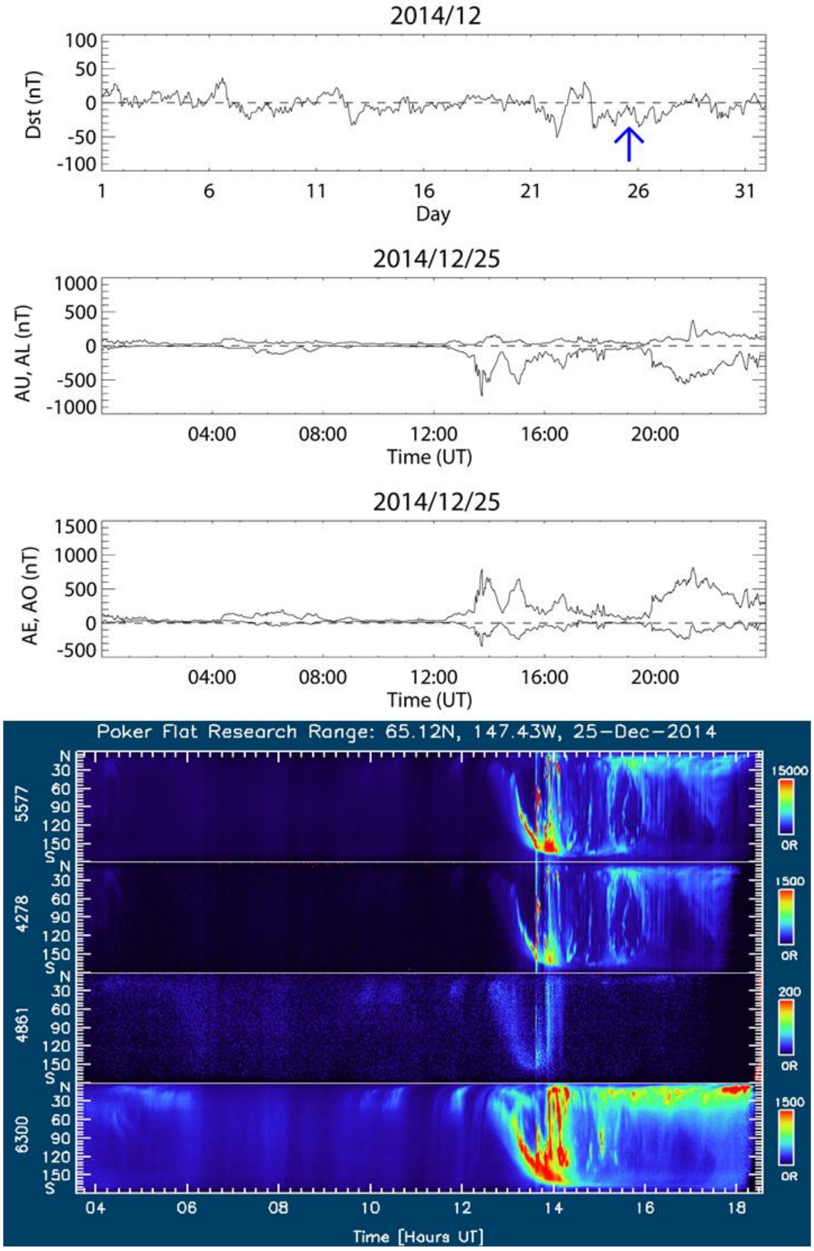

Figure 3.13: *Dst* index, *AE* index, and auroral activities along north-south meridian line over PFRR observed on December 25, 2014.

Figure 3.14 shows the time profile of the background auroral intensity. This event is characterized by the abrupt brightening which was observed at 1337 UT with the maximum intensity of >6000 count. The aurora was the brightest in six nights used for the statistical study, and such a bright aurora did not appear after that time during the night.

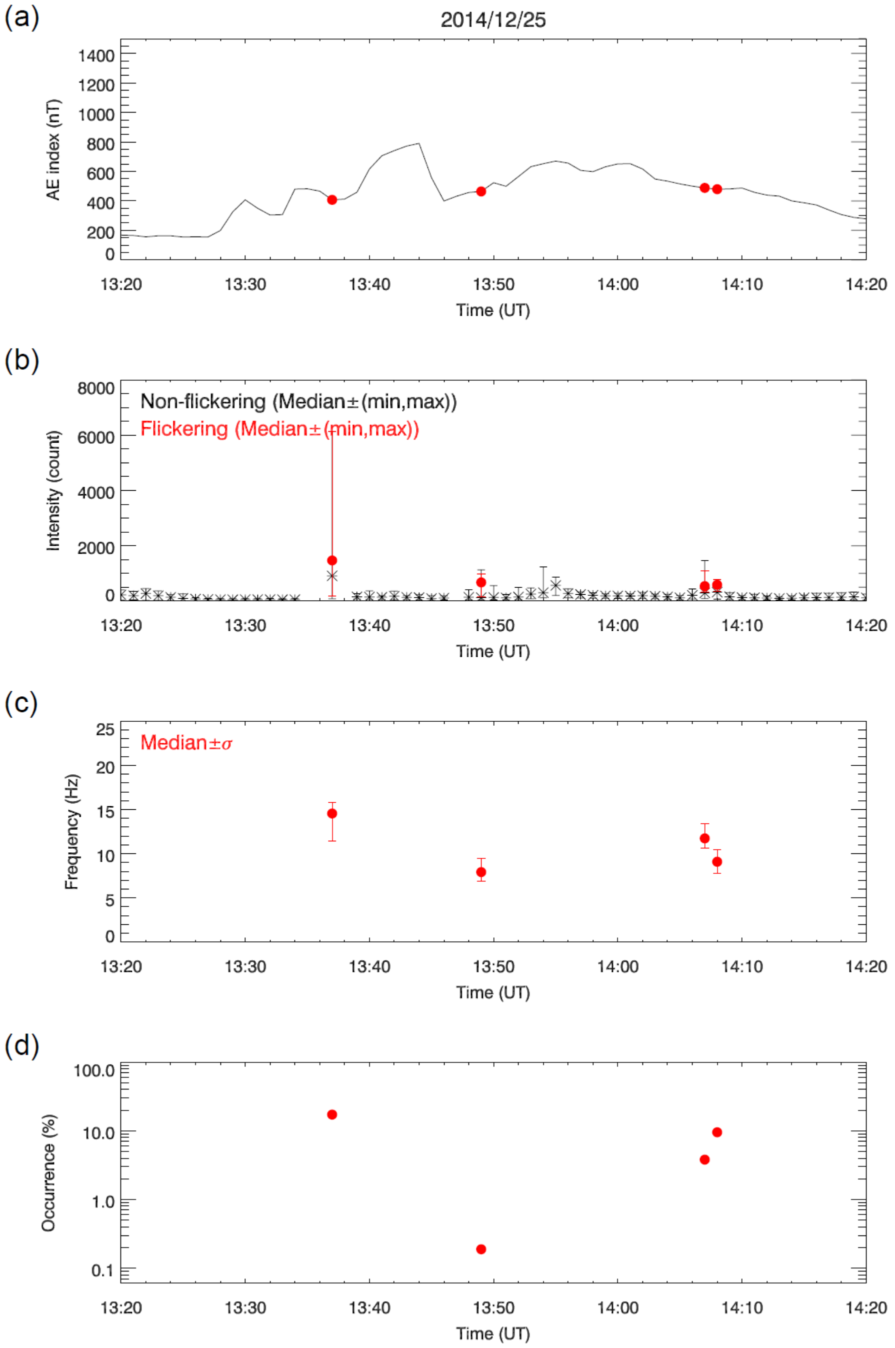

Figure 3.14: Detailed time profiles of *AE* index, non-flickering background auroral intensity, flickering frequency, and total number of points where flickering aurora was detected. The format is the same as that of **Figure 3.6**.

The detailed structure of the bright aurora appeared at 1337 UT are shown in **Figure 3.15**, which has the same format as that of **Figure 3.2**. At this time, two auroras with different intensities were captured within the FOV as shown in the top left panel. One was an active aurora with an intensity of >4000 count which was judged as the non-flickering aurora, and the other was judged as the flickering aurora with an intensity less than 4000 count, which was located equatorward of the bright aurora. It is found that the bright aurora showed rapid spatial variations.

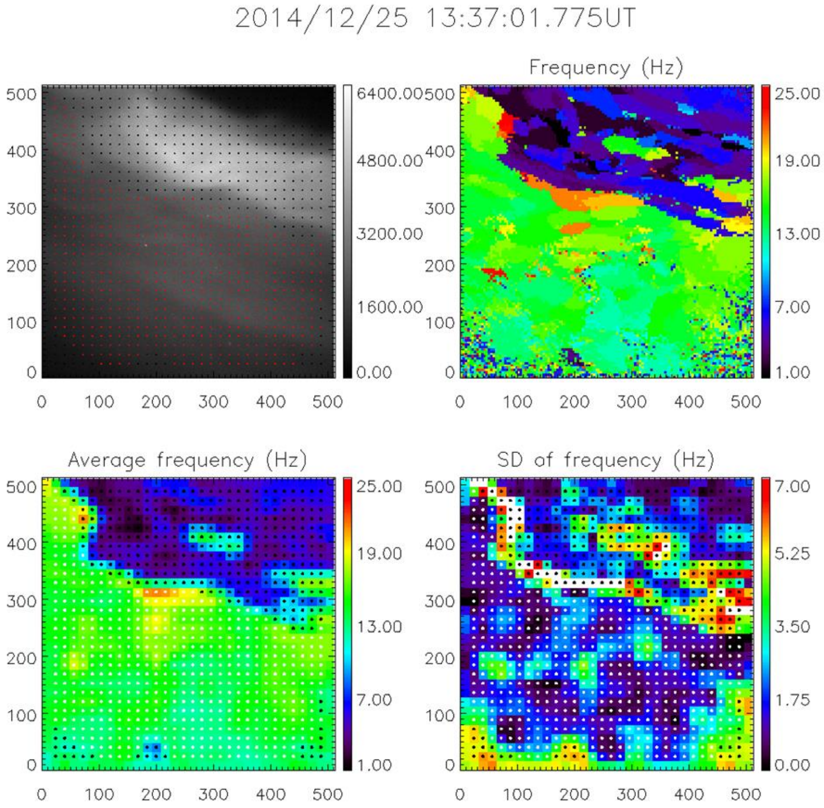

Figure 3.15: Snapshot of automatic detection results for flickering aurora at 13:37:01 UT on December 25, 2014. The format is the same as that of **Figure 3.2**.

Figure 3.16 shows the north-south keogram at x = 256 and the east-west keogram at y = 400 for 20 s from the 13:37:00 UT. Although, for the first 5 s, the bright aurora without the flickering structure was located on the north side of the flickering aurora, the flickering region become so complicated due to the active spatial motion of the bright auroral arc from 13:37:12 UT. After that time, the spatial motion was too active for the auto detection to accurately identify the flickering modulation. The result actually showed that the bright active flow motions was judged as the flickering aurora. That’s why the brightest aurora shown here can be regarded as an erroneous detection.

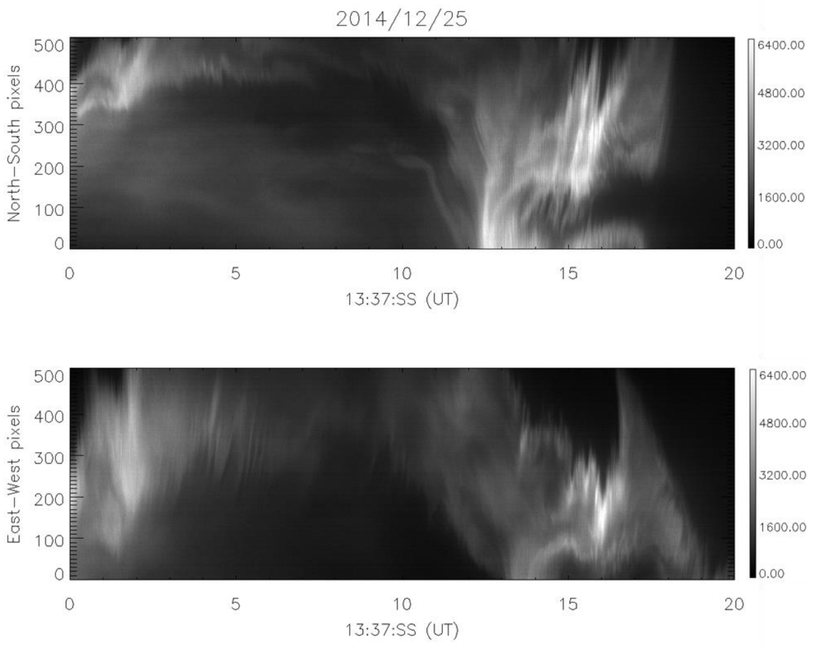

Figure 3.16: North-south keogram at x = 256 and east-west keogram at y = 400 for 20 s from the 13:37:00 UT on December 25, 2014.

Figure 3.17 shows the occurrence rate of the flickering aurora during 1300–1716 UT. It can be seen that the occurrence variation was quite different from the other two examples and that there is a significant increase of the occurrence rate over 4000 count. The increase, which is also shown in **Figure 3.14,** is caused by the brightest active aurora, although the brightest aurora was faultily judged as the flickering aurora by the auto detection. The depletion of the occurrence between 1500 and 4000 count is also caused by the flow motion without the flickering structures, which was accurately judged, accompanied with the brightest aurora.

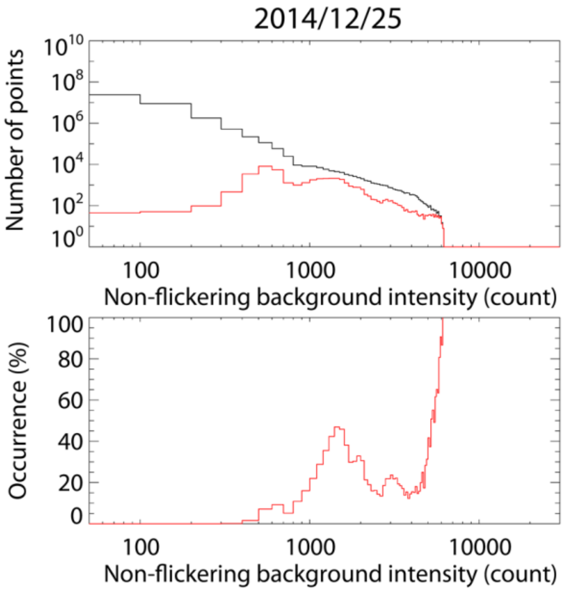

Figure 3.17: Occurrence rates of flickering aurora during 1300–1716 UT on December 25, 2014.

Figure 3.18a-3.18f show the correlations between the flickering frequency and the non-flickering background auroral intensity for each night. Red dots indicate the median value of the flickering frequency for 1 sec. Each panel shows weak correlation, and the correlation coefficients are generally low. **Figure 3.18g** shows the results summed up for six-night data, and the color indicates the total number of the point calculated from each panel. There is not clear correlation between the flickering frequency and the background auroral intensity. It is noted that the cutoff frequency indicates the threshold of the frequency to detect the flickering aurora which corresponds to 6.5 Hz. The peak frequency shown in **Figure 3.18g** is caused by the event observed on February 18, 2015.

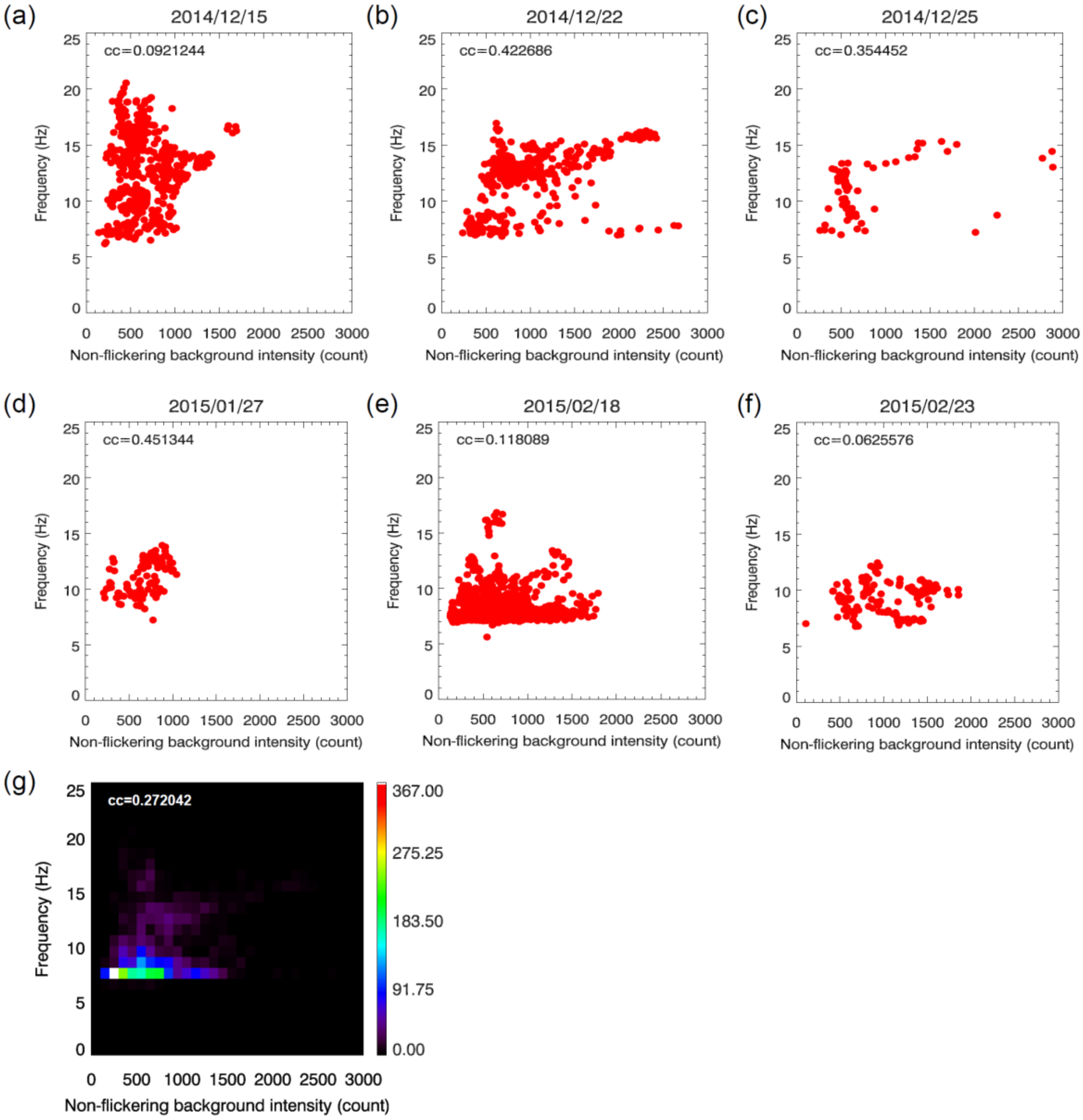

Figure 3.18: Correlations between the flickering frequency and the non-flickering background auroral intensity of each event (a-f), and summed up for 6 nigh data (g). The color shows the total number of red points.

In order to investigate the characteristics of the bright aurora without the flickering structure, other examples, which was judged as the non-flickering aurora and their intensity is over ~1200 count, are summarized in **Table 3.2**. As typical parameters, the intensity, the arc width at the altitude of 100 km, and the shape were listed. The arc widths are calculated by using the stack plot as shown in **Figure 3.11**. Some arc widths could not be estimated, which are shown by hyphens, since the spatial variation was so active (*1), or the edge of the arc was out of the FOV (*2). Some widths are affected by the perspective effect (*3), and thus the shape or the width are not entirely correct. The results show that the bright aurora without the flickering structure is not necessarily the isolated arc. Although some auroras form the multiple arc or the auroral band structure, they do not modulate their intensity. Some cases show the active spatial structures.

Date, Time	Intensity (count)	Arc width (km)	Description
2014/12/15			
0841 UT	1669.0	—— (*2)	Multiple arc, Band
2014/12/22			
0449 UT	1549.0	4.3	Isolated arc (*3)
0456 UT	4464.0	4.5	Isolated arc
0556 UT	1302.0	3.7	Isolated arc
1059 UT	1247.0	—— (*2)	Isolated arc (*3)
2014/12/25			
1354 UT	1400.0	8.5	N-S arc
2015/01/27			
1050 UT	6095.0	—— (*1)	Active, Fine-structure (*3)
1051 UT	9533.0	—— (*1,*2)	Isolated arc
1052 UT	3076.0	—— (*2)	Multiple arc, Band
2015/02/18			
0939 UT	1298.0	—— (*1)	Active -> Unstructured
1051 UT	1260.0	9.3	Multiple arc
1052 UT	1139.0	10.5	Multiple arc
2015/02/23			
0831 UT	1782.0	8.1	Multiple arc
0832 UT	1979.0	—— (*1)	Diffuse -> Wavy

Table 3.2: List of the bright aurora without the flickering structure. The intensity, the arc width, and the shape are summarized (*1: spatial motion, *2: out of FOV, *3: perspective effect).

3.2 Flickering Amplitude

The flickering amplitude to the background auroral intensity has been reported to be 10%–20% by many previous studies [*Berkey et al.*, 1980; *Kunitake and Oguti*, 1984; *Sakanoi and Fukunishi*, 2004; *Gustavsson et al.*, 2008; *Grydeland et al.*, 2008; *Whiter et al.*, 2010]. However, the origin of this ratio is not yet understood. In this study, we statistically investigate the flickering amplitude and aim to clarify the meaning of the flickering amplitude.

3.2.1 Observations

We investigated the relationship between the auroral intensity and the flickering amplitude. **Figure 3.19a** shows snapshots of the flickering aurora captured by the all-sky camera and the sCMOS camera. At this time, the flickering aurora was especially active within the northward bright arc, and a blue cross mark was manually selected to investigate the flickering amplitude. **Figure 3.19b** shows the north-south and east-west keograms across the blue cross, which are created by the subtraction of the running averaged images with a 0.2-s time window. The location of the blue cross is marked by black horizontal dashed lines. It is found that the flickering aurora only appeared within the poleward arc.

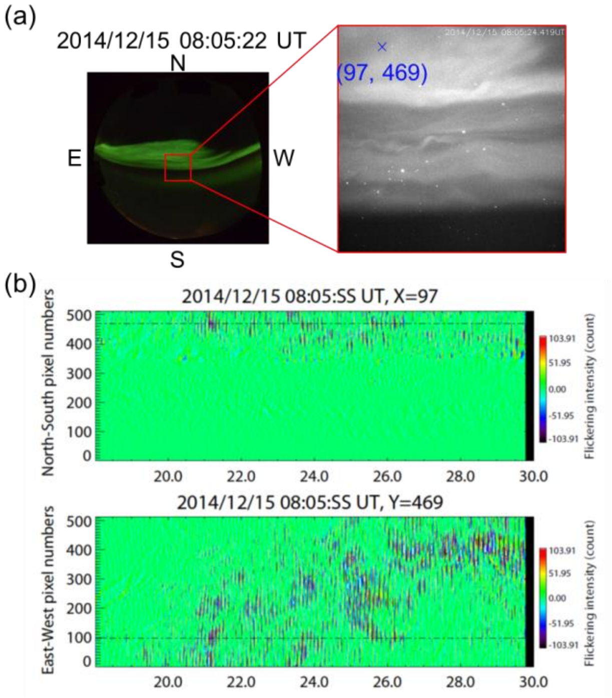

Figure 3.19: (a) Snapshots of flickering aurora observed by the all-sky camera (left) and the sCMOS camera (right). A blue cross marked in the sCMOS image shows the active region of the intensity modulation. (b) North-south and east-west keograms across the blue cross, which are created by the subtraction of the running averaged images (bottom two panels).

Figure 3.20a shows a time profile of the auroral intensity averaged over a 4 × 4 pixel region centered at the blue cross during the 5-s time interval from 08:05:21 UT, which corresponds to the time when the flickering modulation around the blue cross was clearly identified on the keograms. The black line in **Figure 3.20a** represents the intensity modulation, and the red line shows the running average of the back line with a 0.2-s time window, which indicates the intensity of the background non-flickering aurora. **Figure 3.20b** shows the flickering intensity modulation calculated by subtracting the background non-flickering auroral intensity shown by the red line in **Figure 3.20a**. From two values, the flickering amplitude can be calculated, which is the ratio of the flickering intensity to the background non-flickering auroral intensity, as shown in **Figure 3.20c**.

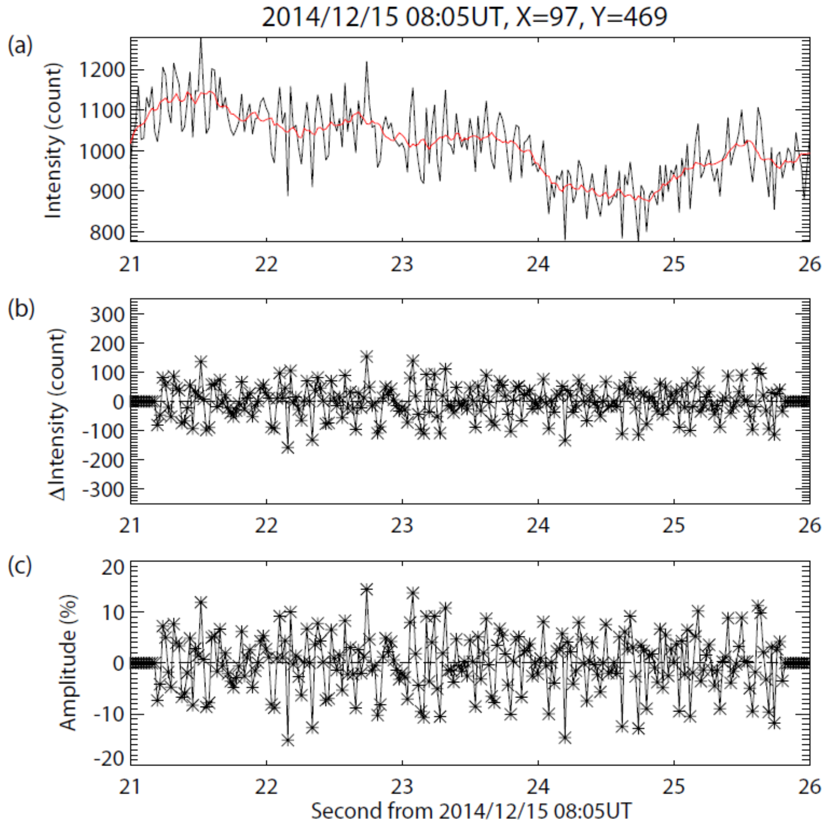

Figure 3.20: (a) Time profile of auroral intensity averaged over 4 × 4 pixel region centered at the blue cross. (b) Flickering intensity modulation calculated by subtracting the background non-flickering auroral intensity. (c) Flickering amplitude calculated by the ratio of the flickering intensity to the background non-flickering auroral intensity.

In order to obtain the flickering intensity, shown by the unit of count, and the flickering amplitude, shown by the unit of %, during this 5-s period, their occurrence distributions were plotted as shown in

Figure 3.21. It is clear that the distribution has a Gaussian profile. Thus, in this study, 2σ is regarded as the typical parameter during this 5-s event, where σ is the standard deviation. In this case, the typical flickering intensity and the flickering amplitude were 112 count and 11%, respectively.

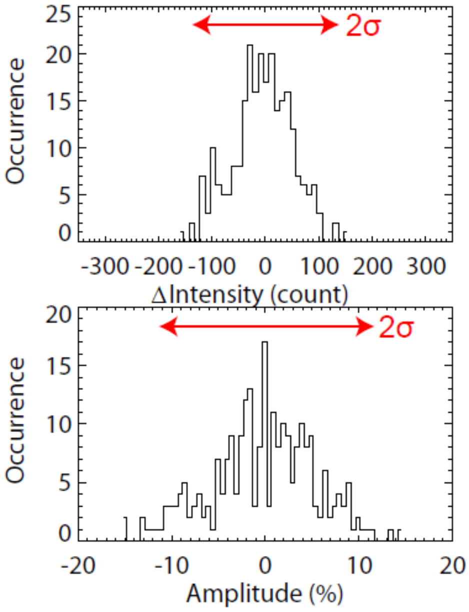

Figure 3.21: Occurrence distributions of flickering intensity and amplitude during the 5-s period shown by **Figure 3.20**.

The same calculations were statistically conducted only for the flickering aurora with the duration >10 s from the same dataset shown in **Table 3.1** by using the automatic detection of the flickering aurora. **Figure 3.22** shows the flickering intensity and the flickering amplitude as a function of the background non-flickering auroral intensity. The color indicates the number of events displayed by the logarithmic scale. It is found that the flickering amplitude decreases with the increase of the background non-flickering auroral intensity as shown in the right panel. This signature comes from the linear relationship with an intercept between the flickering intensity and the background intensity shown in the left panel.

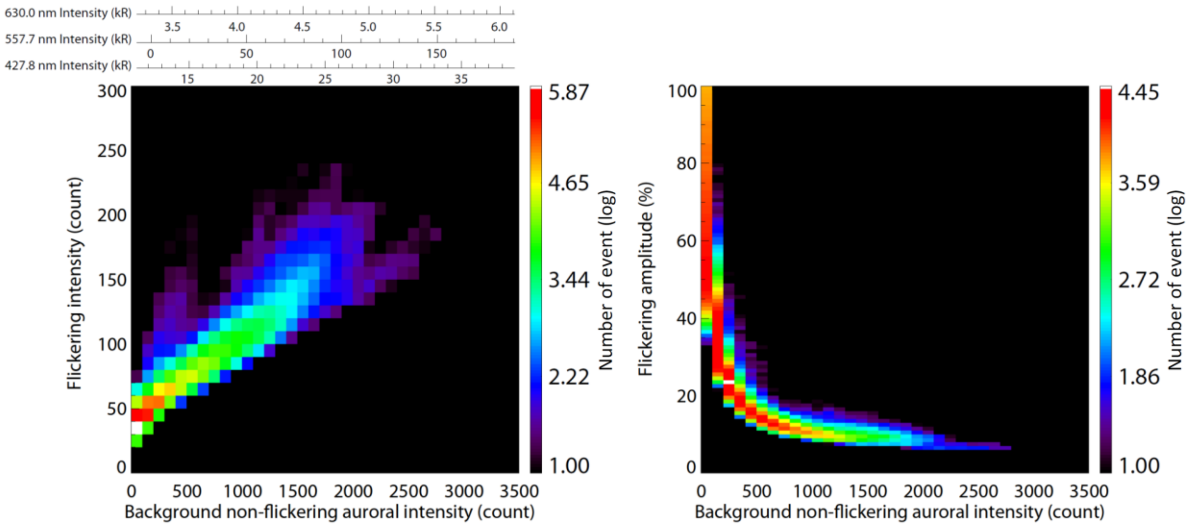

Figure 3.22: Results of correlation between flickering amplitude and background non-flickering auroral intensity. The color indicates the number of events displayed by the logarithmic scale.

3.3 Discussion and Conclusions

From the statistical study on the occurrence property of the flickering aurora, it is found that the occurrence rate is basically proportional to the background non-flickering auroral intensity. Assuming that the auroral intensity is enhanced by a large parallel potential drop, this result is consistent with EMIC waves being easily exited within the auroral acceleration region. This result is inconsistent with the previous study shown by *Sakanoi* and *Fukunishi* [2004], which pointed out that the flickering occurrence rate is not necessarily proportional to the auroral luminosities. The bright aurora without the flickering variation have a tendency of isolated auroral arcs. The result suggests that it is hard to excite EMIC waves inside a narrow acceleration region, because the arc width corresponds to the spatial scale of the acceleration region. Since *Sakanoi* and *Fukunishi* [2004] discuss only one event of the bright omega-band aurora without the flickering modulation, the auroral structure may have been an isolated arc, although we could not compare the result in detail. Many numerical studies show the typical spatial distance to grow EMIC waves. The distance is, however, up to several thousand km, especially for O^+-band EMIC waves, and is not consistent with the realistic conditions due to the homogeneous linear theory [e.g., *Lund and Labelle*, 1997]. Detailed investigations of the threshold of the arc width using the ground-based imaging observation would give new insights into the wave growth process of EMIC waves.

When the auto-detection of the flickering aurora is conducted, the high-pass filtered image is applied to FFT analysis to avoid the effect of the background intensity. In addition, we used the peak frequency of the power spectrum density, as one of threshold to detect the flickering aurora. This method is also unaffected from the background intensity. The most unavoidable effect is the auroral spatial motion, such as flow or drift motions. These motions cannot be removed even if the high-pass filtered image is used. As a result of FFT analysis, the spatial variation appears as the temporal variation and causes wrong determinations.

It is found that the frequency width of the power spectrum density is very narrow. This result is consistent with the satellite and the sounding rocket observations, which show that EMIC waves are narrowband with well-defined spectral peaks [e.g., *Gustafsson et al.*, 1990; *Erlandson and Zanetti*, 1988] and with the ground-based high-speed photometer [*McHarg et al.*, 1998] which shows that the narrowband modulation of ~10 Hz is identified with the typical flickering aurora. However, it is not consistent with the previous study using the ground-based high-speed imaging observation shown by *Yaegashi et al.* [2011], that reports many flickering auroras with the frequency over 15 Hz as the broadband events, although the narrow events are often observed as the typical flickering aurora with the frequency less than 15 Hz. Our results are likely to be similar to the latter case. The narrow band signature of the flickering frequency indicates that the resonance altitude is vertically confined at a particular altitude.

It is also found that the peak frequency gradually increases before the substorm onset. When the flickering frequency corresponds to the local gyrofrequency at the altitude where the resonance interaction with the electron and EMIC waves occurs, the increase in the frequency means the decrease in the resonance altitude. It also means that the auroral acceleration region decreases before the substorm onset. According to the previous study on the source region of AKR [e.g., *Morioka et al.*, 2007], which has been used for the estimation of the auroral acceleration region, the acceleration region shows the two-step vertical evolution at the substorm. The first step is intensification of the low-latitude acceleration region in the altitude range of 3000–5000 km, which induces the initial brightening. The second step is the breakout of the high-latitude acceleration region in the altitude range of 8000–16000 km above the preexisting low-altitude acceleration region, which results in the auroral breakup. This results imply that the flickering frequency decreases at the substorm onset. Our results, however, are inconsistent with this two-step evolution of the acceleration region. Our results also show that the variation of the peak flickering frequency is from <10 to ~20 Hz, and this variation can be estimated as the altitude change from >5000 km to ~2500 km. This altitude range corresponds to the low-latitude acceleration region in the two-step acceleration model.

The signatures of the peak frequency variation and the frequency width suggest that the flickering aurora occurs at the low-latitude acceleration region regardless the substorm phase. This result shows that the low-latitude acceleration region would play an important role in the excitation of the EIMC wave. The frequency variation is likely to be affected by the small-scale vertical structure of the low-latitude acceleration region.

It is found that the flickering frequency is independent of the background non-flickering auroral intensity. The auroral intensity generally tends to increase just after the auroral breakup. At that time, the high-latitude acceleration region is enhanced according to the two-step accelerations as mentioned above. However, the resonant altitude is likely to be located at the low-latitude acceleration region independent of the substorm phase from the analysis of the flickering frequency. The reason why the flickering frequency has no correlation with the auroral intensity is consistent with the possibility that the resonant altitude is confined at the low-latitude acceleration region.

Next, we discuss the origins of the flickering amplitude. Since the auroral intensity is proportional to the total energy flux, we should consider both effects of the electron energy variation and the electron flux variation. Assuming that the Landau resonance interaction between EMIC waves and electrons occurs, the electron energy depends on the parallel phase velocity of EMIC waves. When the linear relation between the flickering amplitude and the background intensity is caused only by the electron energy, the background auroral intensity should control the parallel phase velocity. The minimum amplitude of the flickering aurora shown in the left pane of **Figure 3.22** is ~3 times greater than the noise level shown in Chapter 2. The minimum amplitude is possibly caused by the minimum phase velocity to resonate the electrons. The relation between the auroral activity and the parallel phase velocity of EMIC waves seems to be important for the excitation mechanisms of the EMIC wave. However, we do not have the plausible candidates to explain the relation. When the linear relation is caused only by the electron flux, the precipitating electrons to produce the bright aurora contains the larger amount of electron flux with a particular energy to satisfy the resonance condition. This situation is likely to be reasonable. The minimum flickering amplitude is likely to show the minimum flux number to produce the flickering aurora.

In fact, however, both the electron energy and the electron flux cause the more complicated variation of the auroral intensity. One of the possibilities to cause the variation of the flickering amplitude is shown in the observational results presented in **Figure 1.15** [*Arnoldy et al.*, 1999]. The result demonstrates the time variation of the peak energy of the FABs, which have been thought to form the flickering aurora. Although a few keV electron is the main component to form the discrete aurora, the modulation of the electron count rate was clearly weak at the energy range, since the peak energies of the FAB was less than 1 keV. We think that the peak energy variation is likely to produces the flickering amplitude variation.

In order to investigate the peak energy variation of the FABs, *Chen et al.* [2005] conducted simulation studies. They form the inverted-V flux modulation by a DC potential drop and resonant acceleration due to the parallel electric field of an inertial Alfvén wave pulse. Since the inertial Alfvén wave is derived from EMIC waves under the approximation of $\omega \ll \omega_{ci}$, this situation gives similar results that produced by the Landau resonance interaction with the EIMC wave, when the consecutive Alfvén wave is applied. By using two different strengths of the DC potential drop, 5 kV and 1 kV, they showed that the differential energy flux of the inverted-V electrons was strongly modified by the wave effect in a case with the 1 kV potential drop. They concluded that the inverted-V electron flux is efficiently modified when the velocity of the inverted-V electrons is comparable to or smaller than the peak Alfvén speed. Assuming that the energy of the inverted-V electrons is proportional to the auroral intensity, the flux modulation becomes weaken with the auroral intensity. This tendency is qualitatively consistent with the results shown in the right panel of **Figure 3.22**.

4 Fastest Flickering Aurora

A high-speed imaging observation is an innovative and unique strategy to elucidate the generation mechanism of the flickering aurora. As reported by previous studies, EMIC waves with the frequency ranges below the local f_{O+} and up to the local f_{H+} have often been identified by the satellite and sounding rocket observations [e.g., *Erlandson et al.*, 1994]. These observations imply the possibility that not only O^+-band EMIC waves but also both He^+-band and H^+-band EMIC waves contribute to produce high-frequency flickering auroras.

The purpose of this chapter is to test the hypothesis that flickering auroras are generated by multi-ion EMIC waves by realizing the ground-based high-speed imaging observation with a sampling rate of 160 fps. The spatiotemporal analysis method of flickering auroras is shown in Section 4.1. Section 4.2 provides an event description of the fastest flickering aurora and the results of the spatiotemporal analyses. The possibility of H^+-band EMIC waves as a source of the fastest ever observed flickering modulation is discussed in Section 4.3. Conclusions are provided in Section 4.4.

4.1 Method of Analysis

In order to investigate the short time-scale variation of the flickering frequency, we apply the S-transform [*Stockwell et al.*, 1996]. The definition and the calculation technique of the S-transform, which is derived from an idea of a continuous wavelet transform, are shown below.

The wavelet transform $W(\tau, d)$, which is often used for the frequency–time analysis, of a function $h(t)$ is given by

$$W(\tau,d)=\int_{-\infty}^{\infty}h(t)w(t-\tau,d)dt,$$

where $w(t-\tau, d)$ is a time-shifted mother wavelet $w(t, d)$ with the width of d which controls a frequency resolution. The S-transform $S(\tau, f, \sigma)$ of a function $h(t)$ is denoted by

$$S(\tau,f,\sigma)=\int_{-\infty}^{\infty}h(t)\,g(t-\tau,\sigma)e^{-i2\pi ft}dt,$$

where mother wavelet $g(t-\tau, \sigma)$ is defined as

$$g(t,\sigma)=\frac{1}{\sigma\sqrt{2\pi}}e^{-\frac{t^2}{2\sigma^2}}.$$

Note that σ is the Gaussian width which can be written as the inverse of the frequency, and thus the S-transform is given by

$$S(\tau,f)=\int_{-\infty}^{\infty}h(t)\,g(t-\tau,f)e^{-i2\pi ft}dt.$$

Using a function *p(t, f)*, the above calculation can be simplified as below:

$$p(t,f)=h(t)e^{-i2\pi ft},$$

$$S(\tau,f)=\int_{-\infty}^{\infty}p(t,f)\,g(t-\tau,f)dt.$$

The Fourier transfer *B(α, f)* of the S-transform is given by the convolution integral as follows:

$$\begin{aligned}B(\alpha,f)&=\int_{-\infty}^{\infty}S(\tau,f)e^{-i2\pi\alpha\tau}d\tau\\&=\int_{-\infty}^{\infty}\int_{-\infty}^{\infty}p(t,f)\,g(t-\tau,f)e^{-i2\pi\alpha\tau}dtd\tau\\&=P(\alpha,f)G(\alpha,f),\end{aligned}$$

where *P(α, f)* is the Fourier transform of *p(t, f)*, and $G(\alpha, f)=exp(-2\pi^2\alpha^2/f^2)$ is the Fourier transform of *g(t,σ)*. *P(α, f)* can be written by *F(f)*, which is the Fourier transform of *h(t)*, as follows:

$$\begin{aligned}P(\alpha,f)&=\int_{-\infty}^{\infty}p(t,f)\,e^{-i2\pi\alpha t}dt\\&=\int_{-\infty}^{\infty}h(t)e^{-i2\pi(\alpha+f)t}\,dt\\&=F(\alpha+f).\end{aligned}$$

Thus, the S-transform can be computed using the Fourier transform as follows:

$$S(\tau,f)=\int_{-\infty}^{\infty}B(\alpha,f)e^{i2\pi\alpha\tau}d\alpha=\int_{-\infty}^{\infty}F(\alpha+f)e^{-2\pi^2\alpha^2/f^2}e^{i2\pi\alpha\tau}d\alpha.$$

An integration of the S-transform over a time period gives the Fourier transform as follows:

$$\begin{aligned}\int_{-\infty}^{\infty}S(\tau,f)\,d\tau&=\int_{-\infty}^{\infty}\int_{-\infty}^{\infty}F(\alpha+f)e^{-\frac{2\pi^2\alpha^2}{f^2}}e^{i2\pi\alpha\tau}d\alpha\,d\tau\\&=\int_{-\infty}^{\infty}F(\alpha+f)e^{-\frac{2\pi^2\alpha^2}{f^2}}\delta(\alpha)d\alpha\\&=H(f)\end{aligned}$$

In this study, we estimate the flickering patch scale with a particular frequency by using two different ways: a high-pass filtered image and a phase difference map. The running average of the high-pass filtered image with a particular time window corresponding to the flickering frequency makes clear the flickering patch shape. The phase difference map that is calculated from the S-transform is more useful to investigate the time variation of the flickering patch scale with a particular frequency. A phase difference, $\theta_{xy}(\omega, t)$, between two points x and y based on the S-transform is defined as follows:

$$\theta_{xy}(\omega, t) = \tan^{-1}\left(\frac{Q_{xy}(\omega, t)}{K_{xy}(\omega, t)}\right),$$

where $K_{xy}(\omega, t)$ and $Q_{xy}(\omega, t)$ are the cospectrum and quadrature spectrum between the two points, respectively. They are defined as the real and the imaginary part of a cross-spectrum $S_{xy}(\omega, t)$ as follows:

$$S_{xy}(\omega, t) = h_x(\omega, t)h_y^*(\omega, t) = K_{xy}(\omega, t) - iQ_{xy}(\omega, t),$$

where $h_x(\omega, t)$ and $h_y(\omega, t)$ denote the S-transform spectra of the intensity time profiles at x and y, and an asterisk indicates the complex conjugate. In this study, x and y are defined by a basis pixel, which is selected among the flickering region, and an arbitrary pixel, respectively. A total of 80 phase maps for 1 to 80 Hz are obtained from a calculation of 1-s time interval. This calculation is applied to the extracted 256 × 256 pixel region covering the appearance region of the flickering aurora.

Assuming that the double spatial scale of the flickering patch corresponds to the wavelength of EMIC waves perpendicular to the ambient magnetic field [e.g., *Sakanoi et al.*, 2005], there are two ways to estimate the wavelength by using the phase difference map. By the first way, the wavelength can be estimated from a length between 2π phase difference [*Yaegashi et al.*, 2011]. By the second way, the wavelength can be estimated from a propagation speed of the phase front of EMIC waves. When the propagation speed of the flickering patch with a certain frequency (f) is $V_{p,\perp}$, a perpendicular wavenumber ($k_\perp$) or a perpendicular wavelength ($\lambda_\perp$) can be obtained from the following equation: $V_{p,\perp} = f\lambda_\perp = \omega/k_\perp$. In this study, the wavelengths, estimated from both the running average image and the 2π phase difference, are projected to a resonance altitude of electrons and EMIC waves under the assumption that the emission layer of the flickering aurora corresponds to the altitude of 100 km.

4.2 Observational Results

4.2.1 Event Description

Flickering aurora was observed in the pre-midnight sector (~21.5 MLT) during the auroral breakup at the expansion phase of a substorm with a peak *AE* index of 1266 nT at 0906 UT on 19 March 2016. Ground-based magnetometer data recorded at PFRR are shown in **Figure 4.1a**. H, D, and Z indicate the north–south, east–west, and vertical geomagnetic field components, respectively. **Figure 4.1b** shows the approximate magnetic north–south keogram for 20 min that is created from the data obtained from sCMOS 2 which recorded 512 × 512 pixel images at 40 fps from 0 to 60 s every minute. The location of the magnetic zenith at PFRR is marked by a white horizontal dashed line. An intensity time profile at the magnetic zenith is shown in **Figure 4.1c**. Flickering auroras were detected at particular time when the extremely bright aurora exceeding a few hundred kR at 557.7 nm (not shown) appeared around the magnetic zenith, which is denoted by a white vertical dashed line in **Figure 4.1b**. Flickering auroras were observed within active auroras for a time period of approximately 1 min from 09:05:55 UT by sCMOS 1 which recorded 512 × 256 pixel images at 160 fps from 0 to 60 s every minute. The active auroras including flickering auroras appeared simultaneously with a rapid change in the horizontal component of the geomagnetic field of approximately 300 nT as shown by a black vertical line in **Figure 4.1a**. The geomagnetic field variation corresponds to the field-aligned current density of ~50 μA/m^2 based on the vortex current assumption demonstrated in a study by *Glassmeier et al.* [1992].

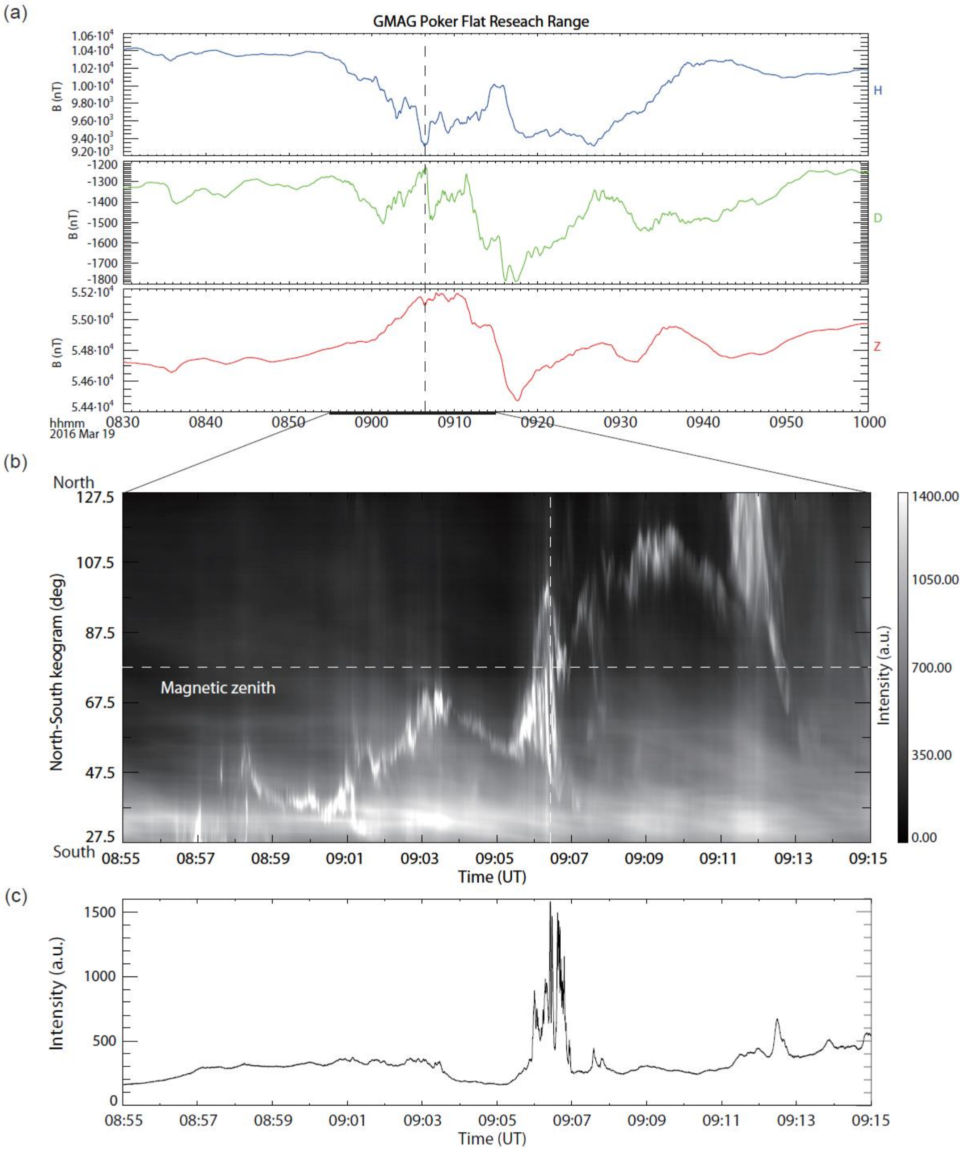

Figure 4.1: (a) Ground-based magnetometer data at PFRR. North–south, east–west, and vertical components are shown as H, D, and Z, respectively. (b) North–south keogram for 20 min created from the data obtained from sCMOS 2 installed at PFRR. (c) Time variation of the auroral intensity around the magnetic zenith shown by a white horizontal dashed line in **Figure 4.1b**.

The active aurora consisting of the fine-scale turbulent motions was detected by sCMOS 1. The flickering aurora was observed at 09:06:26–09:06:29 UT, and the complicated auroral motions began at 09:06:35 UT. Bright arc elements with rapid movements were observed at 09:06:38 and 09:06:40 UT, and flickering auroras sporadically appeared again from 09:06:38 UT. A few "arc packets", which were similar to what was previously reported in a study by *Semeter et al.* [2008], were detected at time intervals of 09:06:35.5 UT and 09:06:43.0 UT.

4.2.2 Spatiotemporal Variations

The fastest flickering aurora discussed in this study sporadically appeared inside the eastward (leftward) drifting arc system for only 1 s at around 09:06:26.600 UT. **Figure 4.2a** shows a snapshot of the flickering aurora observed at 09:06:26.612 UT. A white cross marks the magnetic zenith at PFRR, and a black X and a black diamond denote the selected locations of the fastest flickering aurora and the flickering aurora with a typical frequency, respectively. We assume in this study that the temporal variation is dominant, and the flickering frequency was estimated using the S-transform method. In order to determine the location of the fastest flickering aurora accurately, the 2D-maps of the power spectrum from 1 to 80 Hz for each frame were calculated from the S-transform, and the point X was selected from pixels in which the power spectral density at 75 Hz at 09:06:612 UT was the highest (not shown). **Figure 4.2b** shows the approximate magnetic north–south keogram of the data obtained from sCMOS 1 with higher frequency components exceeding 10 Hz (hereafter referred to as high-pass filtered images) across point X and the diamond for 0.5 s from 09:06:26.355 UT, which is created from the subtraction of running averaged images with a 0.1-s time window at each frame. The time intervals labeled as A and B indicate the time periods of flickering auroras, which are indicated by red arrows, focused on in this study. Flickering modulations at a frequency of approximately 10 Hz were also observed, which corresponds to three black and white pairs around the x = 70–150 pixel region.

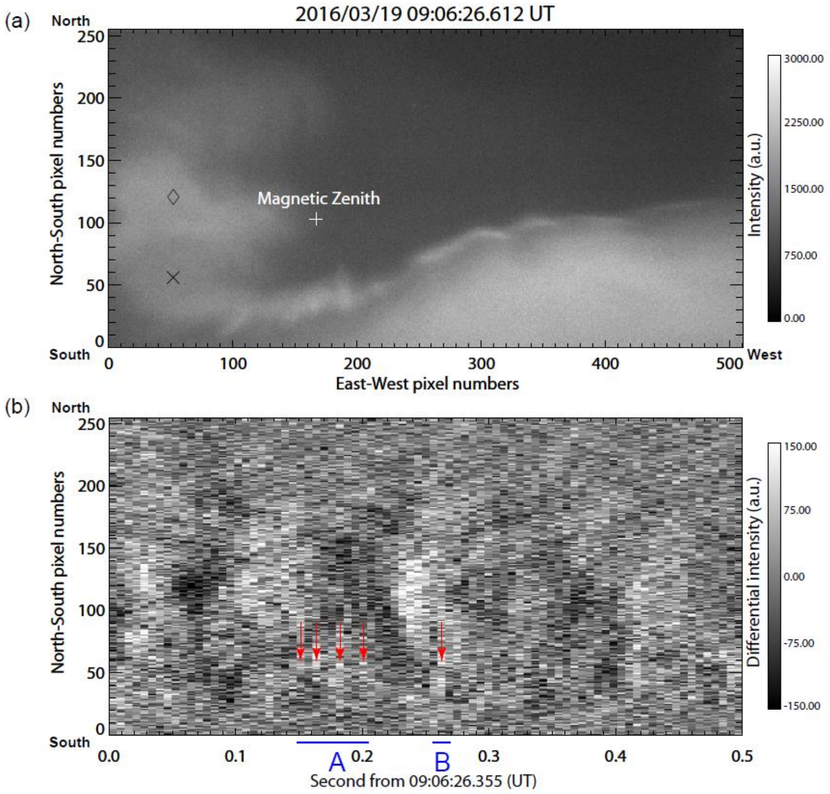

Figure 4.2: (a) Snapshot captured by sCMOS 1 when the fastest flickering aurora appeared around a black X (x = 52, y = 56). A white cross indicates the magnetic zenith at PFRR, and a black diamond (x = 52, y = 120) shows the appearance location of the flickering aurora with a typical frequency. North corresponds to the top, and east corresponds to the left. (b) North–south keogram of the high-frequency components exceeding 10 Hz for 0.5 s from 09:06:26.355 UT across the point X and the diamond. Flickering auroras focused on in this study are indicated by red arrows.

Top panels of **Figure 4.3a** and **4.3b** depict the intensity time profiles averaged over a 5 × 5 pixel area centered at the diamond and the point X as shown in **Figure 4.2a**, respectively. Bottom panels show the frequency–time representations corresponding to 5–80 Hz, which is calculated from the S-transform using each intensity profile to investigate the short time-scale variation of the flickering frequency. The color indicates the logarithmic power spectrum normalized by the square root of each frequency. The result shows that the peak frequency of the typical flickering aurora, appeared around the diamond, is approximately 10 Hz as shown in **Figure 4.3a**. The results also indicate that sporadic intensifications of spectral power over 20 Hz were observed for 0.4 s from 09:06:26.3 UT around the point X. Four bipolar waveforms and a waveform that was especially observed during the time intervals A and B covered frequency ranges of approximately 50–60 Hz and to a maximum corresponding to the Nyquist frequency of 80 Hz, respectively. Each flickering amplitude was approximately 1.6% and 3.2% of the background aurora and was significant, >3σ and >6σ, respectively, where σ is a noise level corresponding to ~14 count. These amplitudes were 6–7 times lower than the typical flickering aurora, which is reported as 10%–20% of the background aurora [e.g., *Berkey et al.*, 1980; *Kunitake and Oguti*, 1984; *Sakanoi and Fukunishi*, 2004].

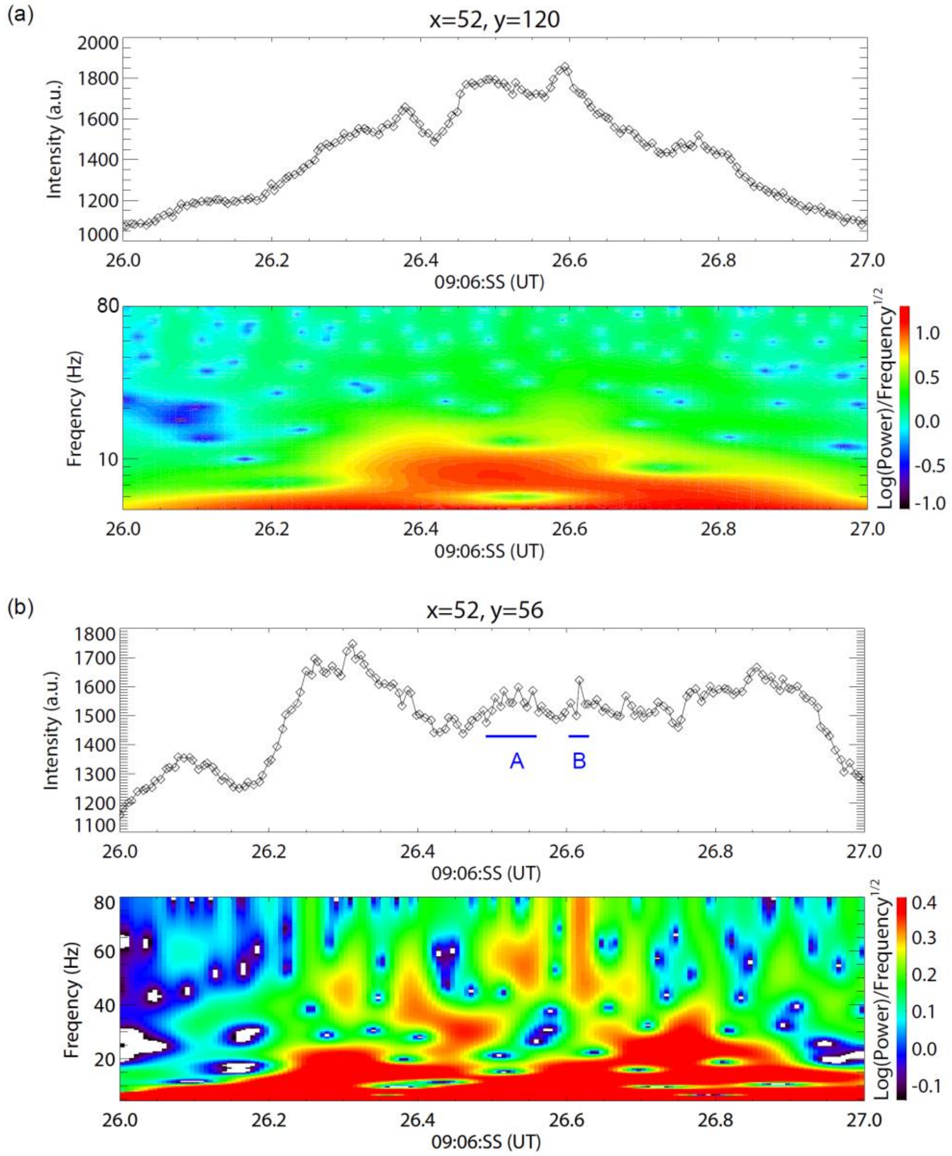

Figure 4.3: Intensity time profiles spatially averaged over a 5 × 5 pixel area centered at the diamond (a) and the point X (b) shown in **Figure 4.2a** and frequency–time representation calculated from the S-transform using each intensity profile for 1 s from 09:06:000 UT. The color shows a logarithm power spectrum normalized by the square root of each frequency.

Figure 4.4 shows the time variation of flickering patch structures that appear within an extracted 256 × 256 pixel region. The running average of the high-pass filtered images with a 0.05-s time window was calculated to investigate the patch scale of the typical 10-Hz flickering aurora. **Figure 4.4a** shows the running average images of a 0.05-s time interval for 0.15 s from 09:06:26.449 UT. It was observed that the flickering patch is roughly circular in shape with an approximately 100 × 100 pixel scale. **Figure 4.4d** represents the patch shape at 09:06:26.499 UT, which corresponds to the second panel of **Figure 4.4a**, and the patch scale is estimated to be 7.0 km × 7.8 km in the approximate magnetic north–south and east–west directions based on a cyan contour under the assumption that the emission layer of the flickering aurora is at an altitude of 100 km. **Figure 4.4b** and **4.4c** show the time variations in differential images that are created by subtracting the high-pass filtered image from a previous frame during time intervals A and B. It is found that clear on–off modulations that corresponds to the frequency range of approximately 50–60 Hz and to the frequency of 80 Hz in **Figure 4.4b** and **4.4c**, respectively. **Figure 4.4e** and **4.4f** show the flickering patch shapes with the frequencies of 50–60 Hz and 80 Hz. The patch shape of the fastest flickering aurora is highly aligned in the east–west direction, and the scale is approximately 1.9 km × 5.9 km in the north–south and east–west directions. These modulations appeared at approximately 5 km equatorward from the center of the typical flickering aurora. It is also found that the patch scale of the fastest flickering aurora is smaller than that of the typical flickering aurora.

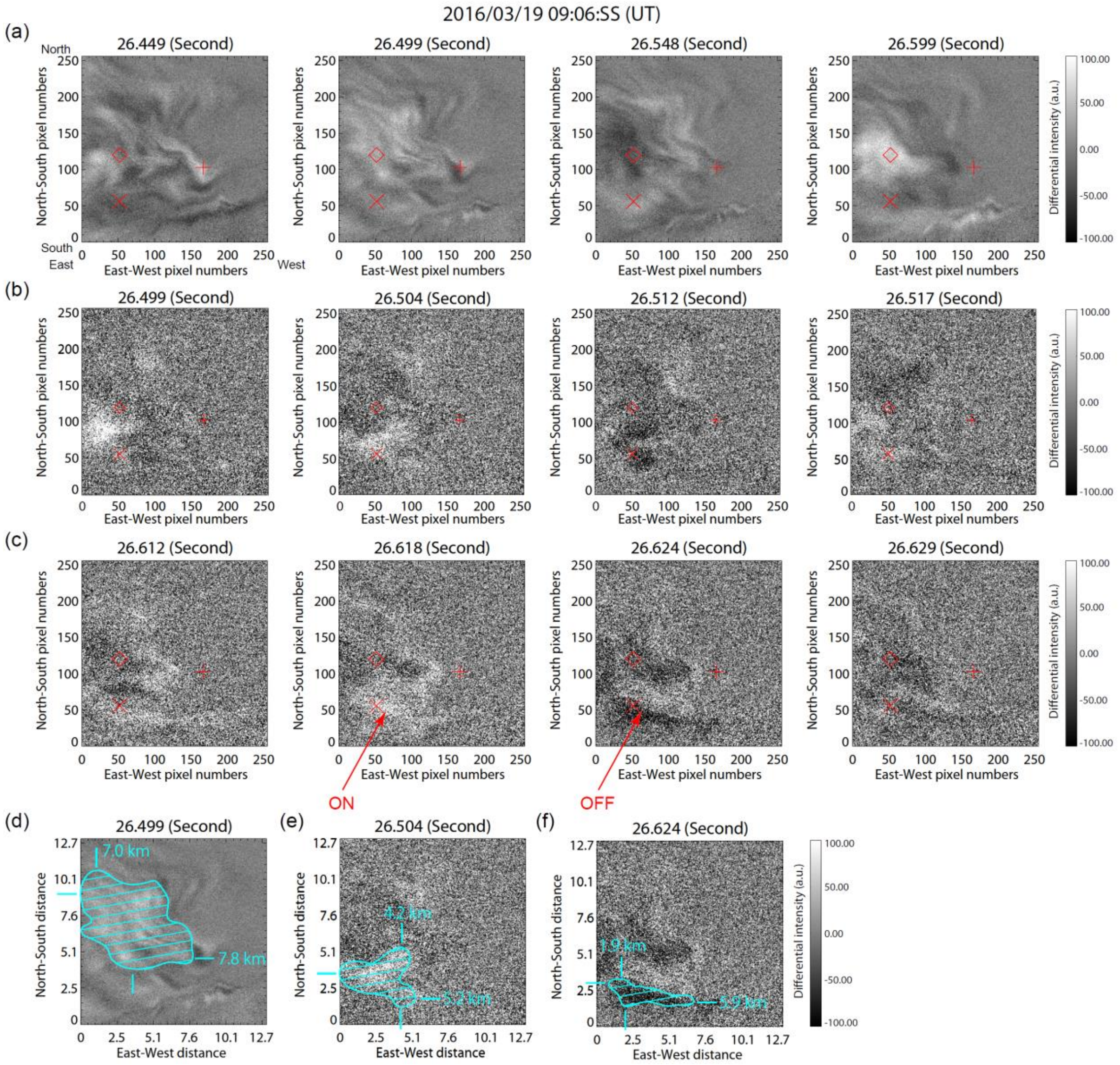

Figure 4.4: Time variations of the flickering patch structures that appear in an extracted 256 × 256 pixel region. (a) Typical 10-Hz flickering aurora represented by the running average of high-pass filtered images with a time window of 0.05 s during a 0.15-s time interval. (b) Flickering aurora with a frequency range of 50–60 Hz and (c) temporal variations of the patch structure varying every 1/160 s represented by subtracting high-pass filtered images from a previous frame during the time intervals A and B. The patch shapes and scales with the frequency equal to (d) 10 Hz, (e) 50–60 Hz, and (f) the fast variations varying every 1/160 s at the altitude of 100 km, respectively.

The estimation of the flickering patch scale by using the phase difference map was also conducted for confirmation of the results obtained from the high-pass filtered image shown in **Figure 4.4**. Top panels of **Figure 4.5** show the snapshots of the phase difference map for the same region as that shown in **Figure 4.4** at frequencies of 10 Hz, 50 Hz, and 75 Hz, respectively, when the modulations with each frequency were significant. For the 10-Hz phase map, the diamond shown in **Figure 4.2a** was adopted as the basis pixel so as to investigate the patch scale of the typical flickering aurora. For the other two phase maps, the point X shown in **Figure 4.2a** was adopted as the basis pixel so as to investigate the patch scale of the flickering aurora with the frequencies >50 Hz. It is found that in-phase regions are distributed centering around the basis pixels at each frequency, although the wavy structure of the phase difference is complicated and the patch shape becomes unclear as frequency increases. For 10 Hz and 50 Hz, the patch sizes with the phase difference from $-\pi/2$ to $\pi/2$ in the north–south and the east–west directions across the basis pixel were manually calculated as accurately as possible, although the patch structure in the phase difference of 75 Hz was obscure. It is found that the patch size of the typical 10 Hz flickering aurora is approximately 5.0 km × 5.3 km in the north–south and east–west directions and is larger than that of 50-Hz flickering aurora with the patch scale of 1.0 km × 4.3 km as also shown in **Figure 4.4**. The estimated values are written in **Figure 4.5a** and are summarized in **Table 4.1** together with the results estimated from the high-pass filtered images shown in **Figure 4.4**. The numbers shown in parentheses are the results estimated from the phase difference map. Due to the ambiguity of the edge of the patch structure shown by the phase difference, there is a tendency that the patch scales estimated from the high-pass filtered image are larger than those estimated from the phase difference map.

Bottom two panels of **Figure 4.5** are time variations of the phase map extracted in the approximate magnetic north–south and east–west directions across each basis pixel. White horizontal dashed lines mark the location of each basis pixel, and white vertical lines represent the time when the phase map are shown. It is found that there is no outstanding propagation of the wave front, which can be used for the estimation from the perpendicular phase speed, around the basis pixel.

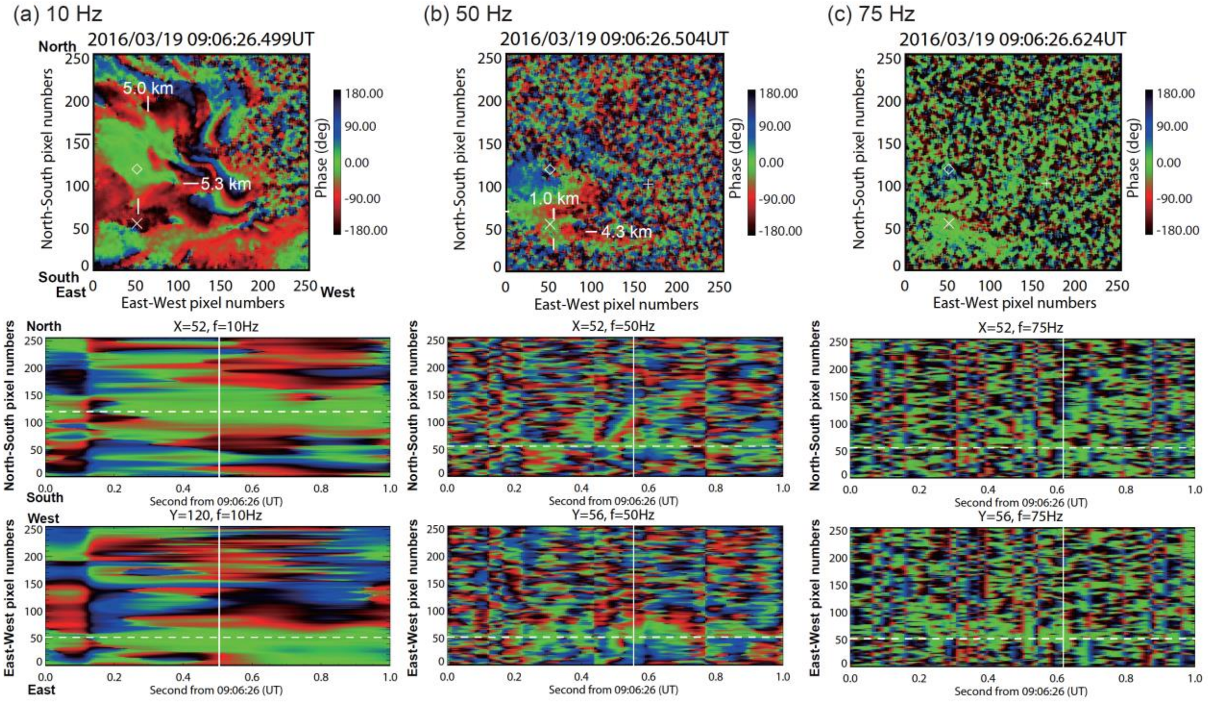

Figure 4.5: Phase maps (top) colored by the phase difference with frequencies of (a) 10 Hz, (b) 50 Hz, and (c) 75 Hz, respectively. Time variations of the phase map in the magnetic north–south and east–west directions across the basis pixel for one second (bottom). White horizontal lines mark the location of the basis pixel, and white vertical lines mark the time when the phase maps were represented.

	f = 10 (Hz)	**f = 50 (Hz)**	**f = 75 (Hz)**
Patch size (N–S) (km)	7.0 (5.0)	4.2 (1.0)	1.9 (—)
Patch size (E–W) (km)	7.8 (5.3)	5.2 (4.3)	5.9 (—)

Table 4.1: Patch sizes in the north–south and east–west directions estimated from the two different ways under the assumption that the emission layer of the flickering aurora is the 100-km altitude. The numbers shown in parentheses are the results estimated from the phase difference map.

4.3 Discussion

In this study, 2D images of the fastest ever observed flickering aurora with the temporal variation of the patchy structure varying every 1/160 s were obtained from ground-based high-speed observations. The flickering aurora with frequencies >20 Hz sporadically appeared within the bright breakup arc of more than a few hundred kR, and the peak frequency intermittently changed on a time scale of 0.1 s during a 0.4-s period from 09:06:26.3 UT. The durations of the time intervals A and B corresponded to

0.05 s and <0.02 s, respectively. The fast flickering aurora was located equatorward of the typical flickering aurora with a frequency of 10 Hz and the spatial distance between the centers of each patch approximately corresponded to 5 km at an altitude of 100 km. The patch was aligned in the east–west direction on the spatial scale of 1.9 km × 5.9 km, which were smaller than those of the roughly circular 10-Hz flickering aurora on the scale of 7.0 km × 7.8 km in the north–south and east–west directions. *McHarg et al.* [1998] used a high-speed 1D photometer to acquire temporal variations of aurora up to 20 kHz. They found that intensity fluctuations were primarily below 80 Hz, and frequencies up to 180 Hz were also detected. As far as we know, the 2D-structure of such a fast-varying flickering aurora have not been reported until now.

We now discuss the origin of the fastest flickering aurora with the temporal variation of the patchy structure varying every 1/160 s. There are two possible source regions to generate such a flickering aurora: magnetosphere region and M–I coupling region. *Kataoka et al.* [2012] found the pulsating aurora with the quasi-periodic modulation at a frequency of 54 Hz. They discussed that short bursts of whistler mode chorus waves, occurring near the magnetic equator [*Trakhtengerts et al.*, 2004], could be one of the possible generation mechanisms. In addition, *Kataoka et al.*, [2015] found a “compound” auroral event comprising the flickering aurora and the pulsating aurora which were simultaneously observed within the narrow FOV of 14.8° × 14.8° during the expansion phase of an intense substorm. If the fastest auroral modulation we showed here was caused by the wave-particle interaction of the whistler chorus wave in the magnetosphere, it is the fast record of “compound” auroral event. However, such an ad-hoc interpretation may not be necessary, since pulsating auroras were not observed and somewhat coherent appearance of the fastest flickering aurora with standard flickering aurora at the same time at an overlapped position.

One of the possibilities in the M–I coupling region is the frequency modulation effect due to the interference wave, as shown in Section 1.5.2, consisting of the O^+-band EMIC waves with slightly different frequencies. If two frequencies of the O^+-band waves were 10 Hz and 20 Hz, respectively, the high-frequency component of the interference wave does not exceed 15 Hz. By the same reason, the interference wave consisting the two He^+-band EMIC waves or the O^+-band and He^+-band EMIC waves cannot generate the flickering aurora with the frequency 80 Hz.

Another possibility, or probably the most plausible generation mechanism in the M–I coupling region, is H^+-band EMIC waves. The observational results show that the typical flickering frequency was approximately 10 Hz. Consequently, the resonance altitude between electrons and O^+-EMIC waves can be estimated as 6000 km. Multi-ion EMIC waves in O^+, He^+, and H^+ generally have the frequency depending on the propagation angle. Given the assumption that all multi-ion EMIC waves resonate electrons at the same altitude of 6000 km, the frequency range of H^+-EMIC waves with the propagate angle of 0–90° is 40–160 Hz. It is found that the frequency of the observed fastest flickering aurora possibly corresponds to the lower frequency range of H^+-EMIC waves. If the proposed hypothesis was true, much faster flickering aurora with the higher frequency range can also be detected in future by a higher speed imaging than that of the observations in the present study.

In order to diagnose the validity of multi-ion EMIC waves, we compare the theoretical dispersion relations of EMIC waves in the multi-ion component plasma with the observational results of the flickering frequency and the wavenumber obtained from the spatiotemporal analysis. **Figure 4.6** shows two cases of the dispersion relations of EMIC waves with perpendicular propagation angles from 85° to 89° [e.g., *Sakanoi et al.*, 2005; *Yaegashi et al.*, 2011; *Michell et al.*, 2012] in the different two multi-ion plasma conditions in consideration of different occurrence locations and resonance altitudes of each flickering aurora. Black points indicate the observational results of the flickering frequency and the wavenumber estimated from the S-transform and the high-pass filtered image shown in **Figure 4.4**. The wavenumber is projected to the resonance altitude from the emission layer of the flickering aurora corresponding to the altitude of 100 km. The error bars indicate the minimum and maximum values of each parameter. The theoretical dispersion relations shown by colored solid lines can be calculated by assuming the propagation angle of EMIC waves, the total electron density, and the ion composition ratio at the resonance altitude, and are fitted so as to cover the observational results by choosing the total electron density and the ion composition ratio. Vertical dashed lines shown in **Figure 4.6** indicate the lower limit of the perpendicular wavenumber, which are determined by the FOV and the resonance altitude.

Figure 4.6a indicates the case that the fast flickering aurora with the frequency range of 50–60 Hz and up to 80 Hz appears at the same spatial location of the typical 10-Hz flickering aurora as shown in **Figure 4.3a**. The resonance altitude between electrons and the 10-Hz O^+-EMIC wave can be estimated as 6000 km. In this case, it is assumed that all multi-ion EMIC waves resonate the electron at the same altitude of 6000 km. By fitting the theoretical relation to the observational results of the frequency range and the wavenumber range, the total electron density and the ion composition ratio can be obtained as 20 cm^{-3} and $H^+ : He^+ : O^+ = 70 : 10 : 20$, respectively. Although the modulation of 50–60 Hz is interpreted as H^+-band EMIC waves in this case, the estimated electron density is not reasonable, since the density is two order of magnitude greater than the typical density in the cavity region and is one order of magnitude lower than the ambient density at the altitude.

Figure 4.6b indicates the case that the typical flickering aurora appears at the same spatial location of the fast flickering aurora with the upper limit of the typical frequency corresponding to 15 Hz during the time intervals A and B as shown in **Figure 4.3b**. The resonance altitude between electrons and the 15-Hz O^+-EMIC wave can be assumed as the 3500-km altitude. In this case, all multi-ion EMIC waves are assumed to resonate the electron at the same altitude of 3500 km within the same spatial region of the fastest flickering aurora. The estimated total electron density and the ion composition ratio are 0.2

cm^{-3} and $H^+ : He^+ : O^+ = 70 : 10 : 20$, respectively. These results are consistent with the parameters at the proton-rich density cavity inside the auroral acceleration region [e.g., *McFadden et al.*, 1999]. In this case, the origin of the modulation of 50–60 Hz can be interpreted as the He^+-band wave. It is also found that both cases show that the origin of the fastest flickering aurora with the frequency >80 Hz can be interpreted as H^+-band EMIC waves.

Since the cavity region is actually dominated by plasma sheet electrons with temperatures over 100 eV, the hot plasma treatment is needed to consider for the wave propagation property. According to the hot plasma theory, the effect of the cyclotron damping cannot be ignored when $k\lambda_D \geq 1$ where λ_D is Debye length. In consideration of the auroral cavity region, λ_D is approximately 330 m for 1 keV electrons in the plasma density of 0.5 cm^{-3}, which corresponds to the wavenumber of $\sim 20 \times 10^{-3}$/m and is an order of magnitude greater than our observational results. We also consider finite gyroradius effects, which confine the wave-particle interaction at the small spatial scale as shown by *Michell et al.* [2012]. At the altitude of 3500 km, the gyroradius of O^+, He^+, and H^+ with a temperature of 1 keV are 840 m, 420 m, and 210 m, respectively. From these values, the wavenumbers of O^+, He^+, and H^+ are 7.5×10^{-3}/m, 15×10^{-3}/m, and 30×10^{-3}/m, respectively. These results indicate that the cyclotron damping or the finite gyroradius effect do not affect the Landau resonance interaction on the scale of our observational results. In other words, if we found the flickering patch with the scale less than ~100 m, we can test the damping and finite gyroradius effects.

The resonance energy of the electron to satisfy the Landau resonance condition can be estimated by using the frequency, the propagation angle, and the perpendicular wave number, although the energy strongly depend on the propagation angle. In case of **Figure 4.6a**, the resonance energies of the electron to interact EMIC waves with the frequency of 8.0 Hz, 55.0 Hz, and 72.5 Hz are <900 eV, >4.2 keV, and >2.8 keV, respectively. In case of **Figure 4.6b**, these energies are estimated as >460 eV, >8.6 keV, and >5.7 keV, respectively. *Whiter et al.* [2010] reported that the electron energy to cause the flickering aurora is up to approximately 40 keV, which exceeds the peak energy of the inverted-V electrons, by using ground-based multispectral imaging observations. Although our estimations of the resonance energy associated with EMIC waves are lower than the previous study shown by *Whiter et al.* [2010], especially for EMIC waves with the frequency >55 Hz, they are comparable to the typical energy range of the inverted-V electrons. These results indicate that the Landau resonance condition was possibly satisfied at the auroral acceleration altitude.

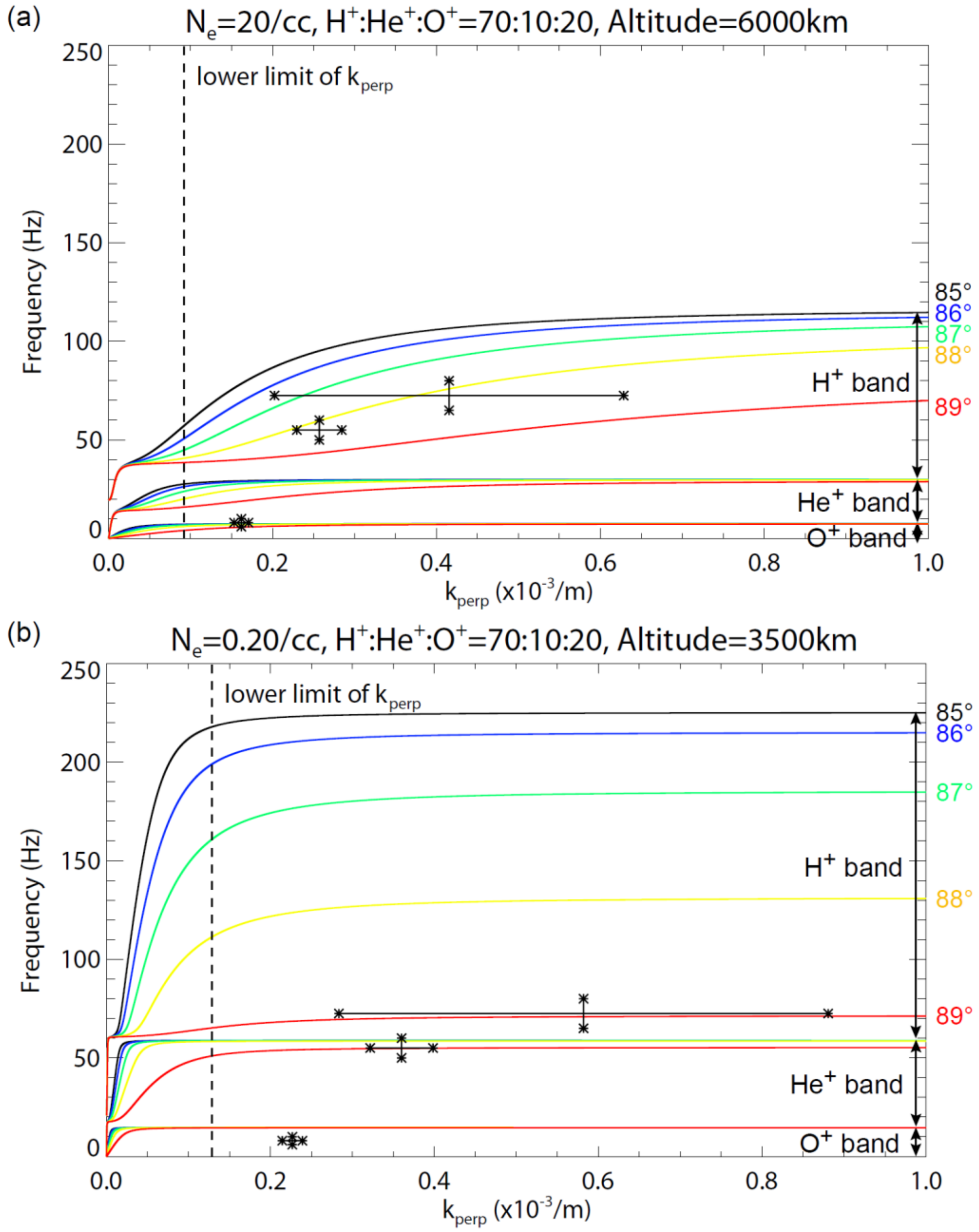

Figure 4.6: Two cases of dispersion relations of EMIC waves with the perpendicular propagation angles (black, blue, green, yellow, and red lines) in different two multi-ion plasma conditions and observational results of the flickering frequency and the wavenumber (black points).

One may consider that our results are helpful to diagnose the plasma condition at the resonance altitude using the comparison between the observational results and theoretical dispersion relation. The fastest flickering aurora was, however, actually complicated by a sporadic appearance relative to the typical flickering aurora, and the resonance altitude or the total electron density cannot be uniquely decided as shown in **Figure 4.6**. These results potentially indicate that the generation mechanism is beyond the linear theory of multi-ion EMIC waves, and that it is necessary to consider nonlinear wave emission in the inhomogeneous plasma.

We consider two aspects of the reasons for the first-time detection of possible H^+-band flickering aurora, namely, technical and theoretical aspects. The technical reason is that the high-speed imaging observation enabled the detection of the sporadic appearance of the fast flickering aurora on a time scale of 0.1 s with a limited horizontal scale of 1.9 km × 5.9 km. Satellite and sounding rocket observations cannot resolve such fast and fine-scale variations.

With respect to the theoretical aspect, the detectability of H^+-band EMIC waves was demonstrated by previous studies using ray tracing calculations [*Lund and LaBelle*, 1997]. The results indicated that H^+-band EMIC waves with a normal wave angle <10° can propagate to lower ionospheric altitudes as the source altitude decreases without reflection at bi-ion hybrid resonance frequencies, although H^+-band EMIC waves were significantly attenuated when compared with O^+-band EMIC waves. The propagation properties are consistent with the observational result that the flickering aurora associated with H^+-band EMIC waves was rarely observed when compared with that of the traditional O^+-band EMIC wave. Thus, in order the resonance interaction of H^+-band EMIC waves to occur, H^+-band EMIC wave resonates electrons at a higher altitude prior to the wave attenuation or the source altitude of H^+-band EMIC waves is lower than usual to propagate the lower altitudes.

We now discuss the formation mechanisms for the spatiotemporal behavior of the fastest flickering aurora. The fine-scale flickering structure with a frequency of 80 Hz was east–west aligned and is consistent with the spatial asymmetric property demonstrated in a study by *Michell et al.* [2012]. A possible reason for the result is the interference pattern composed of multiple EMIC waves with different wavenumbers. In addition, the fast-varying patchy structure appeared at ~5 km equatorward from the center of the typical flickering aurora. The spatial gap between these appearances is likely to be associated with the propagation property of multi-ion EMIC waves. *Lund and LaBelle* [1997] showed that H^+-band EMIC waves are more spread over a wide latitude range than the O^+-band EMIC waves and consequently have a lower power spectral density. Although our result showed that the H^+-band flickering aurora has smaller scale structure than that of typical flickering auroras, further investigations of the spatial distribution and the patch scale of flickering auroras generated by multi-ion EMIC waves are important to clarify the wave property in a multi-ion species plasma.

The temporal variation of the fastest flickering aurora was actually complicated by a sporadic appearance on a time scale of 0.1 s. This feature is likely to be caused by the rapid appearance and disappearance of multi-ion EMIC waves and indicates that the generation mechanisms are beyond the linear theory due to nonlinear effects as discussed in the inner magnetosphere [*Omura et al.*, 2010].

Although another possibility is a temporal variation of the acceleration region associated with the wave excitation, it is not likely to be reasonable, because the parallel potential drops appear to be stable on time scales corresponding to tens of seconds [*Ergun et al.*, 1998].

Our study could not explain the excitation mechanism of the sporadic multi-ion EMIC waves based solely on the high-speed imaging observations. In order to improve our understanding of the formation mechanisms discussed above, simulation studies of the generation and propagation properties of multi-ion EMIC waves are needed. It is important to consider non-linear and inhomogeneous effects in order to reproduce observations of complicated spatiotemporal variations.

4.4 Conclusions

We found 2D images of the fastest ever observed patchy flickering aurora varying every 1/160 s by the ground-based high-speed observation. The flickering aurora with frequencies >20 Hz sporadically appeared within the bright breakup arc, and the peak frequency intermittently changed on a time scale of 0.1 s during 0.4-s period. The fast-varying patch was aligned in the east–west direction and was smaller than the roughly circular 10-Hz flickering auroral patch. These results are consistent with the hypothesis that flickering auroras are generated by multi-ion EMIC waves in the inhomogeneous plasma.

5 Application of High-speed Imaging Observations

The high-speed imaging observation have been used not only for the investigation of the flickering aurora but also for the other auroras with quasi-periodic modulations. In this chapter, rapid spatial motions of the pulsating aurora are presented as one of the applications for the high-speed observation.

5.1 Introduction

Pulsating aurora is a phenomenon defined by the repetition of irregular ON–OFF switching of auroral intensity. The typical repetition period is a few to 20 s [*Yamamoto*, 1988]. The pulsating aurora is typically observed during the recovery phase of substorms in both auroral and subauroral zones over a wide range of magnetic local times [e.g., *Cresswell*, 1972; *Royrvik and Davis*, 1977]. A quasi-periodic intensity modulation of 3 ± 1 Hz is often observed during the ON-phase [e.g., *Nishiyama et al.*, 2014; *Sandahl et al.*, 1980; *Sato et al.*, 2004]. From sounding rockets and satellite observations, flux modulations of precipitating electrons with energies of a few to tens of keV were shown to be present at 3 ± 1 Hz [e.g., *Miyoshi et al.*, 2010, 2015; *Nishiyama et al.*, 2011; *Sandahl et al.*, 1980; *Sato et al.*, 2004].

Two source regions for the pulsating aurora have been considered. The first is placed far from the earth, around the magnetic equator. *Nishimura et al.* [2010] indicated a one-to-one correspondence between chorus waves and auroral intensity modulation from a conjunction event of THEMIS satellites located at the magnetic equator and ground auroral imagers. *Miyoshi et al.* [2010] proposed a new model for the TOF effect of the precipitating electrons by considering the propagation of chorus waves. *Miyoshi et al.* [2010] and *Nishiyama et al.* [2011] conducted TOF analyses assuming wave–particle interactions of electrons with propagating chorus waves from the equator and showed that the region is covered up to approximately 15° MLAT at the off-equator. Another possible source region is located much closer to the earth. *Sato et al.* [2004] showed that the aurora of Syowa–Iceland pair observations were not conjugate in shape and the FAST satellites detected an anti-correlation between electrons and ions, suggesting that the field-aligned potential drop contributes to the modulations. Their study indicated that the source region was ~2 to 6 R_E above the FAST satellite [*Sato et al.*, 2004].

Miyoshi et al. [2015] elucidated the origin of the internal modulations including the 3 ± 1 Hz of the pulsating aurora by a comparative study of the Reimei observations and a computer simulation. They concluded that the main modulations with a few seconds are caused by lower-band chorus bursts and the 3 Hz modulations are caused by a repetition of rising tone chorus elements embedded in the chorus bursts. *Katoh* [2014] showed that the propagation of chorus elements from the magnetic equator is dependent on the background density distribution by a simulation study. In cases of density enhancement or decrease to form a wave duct, chorus elements can propagate well along the magnetic field; in cases without such a duct, they obliquely propagate and gradually depart from the initial magnetic field.

It is well known that horizontal patches move with speeds in the order of km s^{-1} at ionospheric altitudes by E × B drift [*Nakamura and Oguti*, 1987]. In addition, complicated spatial and temporal motions of pulsating patches have been observed and classified into several types according to their shapes, sizes, and propagating features [e.g., *Oguti*, 1978; *Yamamoto and Oguti*, 1982]. The fastest motions that have been reported are fast auroral waves [*Boyd et al.*, 1972; *Cresswell*, 1968; *Cresswell and Belon*, 1966; *Scourfield and Parsons*, 1971] and superfast auroral waves [*Hough et al.*, 1992]. Fast auroral waves are east–west aligned in an arc-like form and travel equatorward at a speed of up to 300 km s^{-1} over a distance exceeding 250 km. Their repetition rate is typically 1 Hz. Superfast auroral waves also propagate equatorward over a distance exceeding 1400 km with a typical speed of 700 km s^{-1} and a maximum speed of 1200 km s^{-1}. Although the generation mechanisms of these fast auroral waves are currently an open question, earthward-propagating magnetohydrodynamics waves, i.e. the most basic waves here are fast-mode waves propagating across the field line in the equatorial plane, are considered to be a possible candidate.

Spatial variation in pulsating patches associated with the 3 ± 1 Hz intensity modulation has rarely been reported, except for *Nishiyama et al.* [2016]. They investigated the spatial and temporal characteristics of the pulsating aurora by using principal component analysis and FFT analysis. They showed that substructures of the patch with the 3 Hz modulation oscillated back and forth, which may be closely related to the propagation process of chorus waves.

The purpose of this chapter is to report the rapid spatial-temporal motions of the pulsating aurora, including variations accompanying the 3 ± 1 Hz modulation. In Section 5.2, we show the fundamental properties of the pulsating aurora, such as the velocity and direction of motion. In Section 5.3, we discuss the formation mechanism considering the velocity of the chorus elements' propagation from the magnetic equator. Concluding remarks are provided in Section 5.4.

5.2 Observations

We focus on the pulsating aurora that appeared in the post-midnight sector during the recovery phase of a particular magnetic storm with a minimum *Dst* index of −112 nT at 0900 UT on 19 February 2014, because the motions of the pulsating aurora were bright enough to be clearly identified. This was the largest storm to have occurred during the two-month observational period of the first-winter season;

additionally, large substorms with a peak *AL* index of −1713 nT took place on the same day. When the bright pulsating aurora covered the whole sky over the Poker Flat Research Range, the *AE* index decreased from approximately 650 nT to 100 nT during the 45-min time interval from 1414 UT to 1459 UT (around 3.0 MLT). For those 45 min, we identified many characteristic expansions at the edges or over the entirety of patches. Some events show directional expansion, while some show self-similar expansion in all directions. The expansion appears not just once, but repetitively, during an ON-phase.

Figure 5.1 shows an example of the pulsating aurora as observed by the all-sky camera and the sCMOS camera which recorded 512 × 512 pixel images at 50 fps from 0 s to 10 s every minute. **Figure 5.1a** is an all-sky image captured at 14:14:01 UT. The pulsating patches slowly drifted over approximately 4 km at 100-km altitude toward the east side for 20 s. The estimated drift speed, 0.2 km s^{-1}, is in the range of typical speeds of the E × B drift as reported by *Foster and Vo* [2002]. The red square represents the FOV of the sCMOS camera. **Figure 5.1b** shows a snapshot of an elongated patch with the repetitive expansions at the edge captured by the sCMOS camera. **Figure 5.1c** is a keogram along the black line across the elongated patch shown in 5.1b. Repetitive expansions of the pulsating patch were observed for the ON-phase time intervals from 14:14:01.5 to 14:14:02.5 UT and from 14:14:05.0 to 14:14:07.5 UT. **Figure 5.1e** shows the time series of averaged auroral intensity of a 5 × 5 pixel region centered at the light blue dot (x = 195, y = 91) in **Figure 5.1b**. There are two clear ON-phases, and quasi-periodic intensity modulations caused by the repetitive expansions appear during the ON-phases. **Figure 5.1d** shows an extended plot for the time interval from 14:14:06.5 to 14:14:07.5 UT. In this event, outward motions, represented by a black arrow from the main patch, are prominent, and the inward motions toward the main patch can rarely be identified.

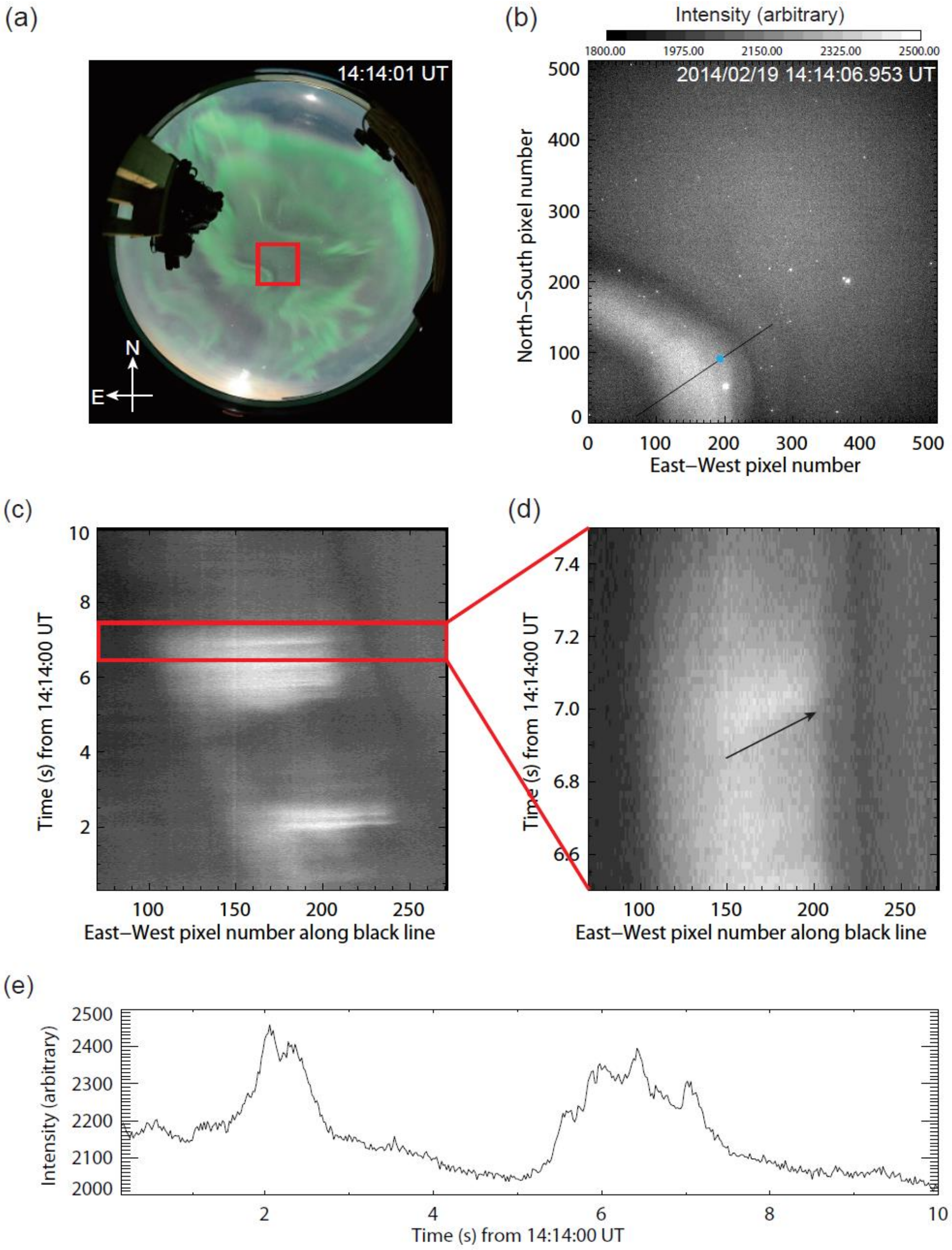

Figure 5.1: (a) All-sky image captured at 14:14:01 UT on 19 February 2014. Top is north, and right is west. The red square is the field-of-view of the sCMOS camera. (b) Example of repetitive expansions at the edge of a pulsating patch. Intensity is shown by gray scale in arbitrary unit. (c) Keogram aligned at the black line shown in **Figure 5.1b** for 10 s. (d) Extended keogram between 14:14:06.5 and 14:14:07.5 UT. (e) Averaged auroral intensity of the 5 × 5 pixels region centered at x = 195 and y = 91.

To study the complicated rapid motion in more detail, a differential image between 14:14:06.953 and 14:14:07.053 UT was constructed as shown in **Figure 5.2**. The displacement of the edge between the two images is indicated by red arrows. The edge moves toward the northwest direction, and the distance of the displacement is 1.4 km in 0.1 s, corresponding to a speed of 14 km s^{-1} assuming that the auroral emission is located at an altitude of 100 km. In this study, we used the differential image technique to investigate the speed and direction of the patch motions for the 45-min period of interest. For the repetitive motions, we estimated the speeds for each expansion and used the speed as one sample data point. For the observation period of 10 s, the pulsating features look clearly different from those captured 1 min before. Almost all the patches move outside of the FOV by E × B drift motion, and some patches may drastically change their shapes before the next observation period of 10 s starts. In this study, we regard different features for every 1-min interval to investigate if the patch feature is universal or not on the assumption that the slowly drift motion continues for the rest of 50 s.

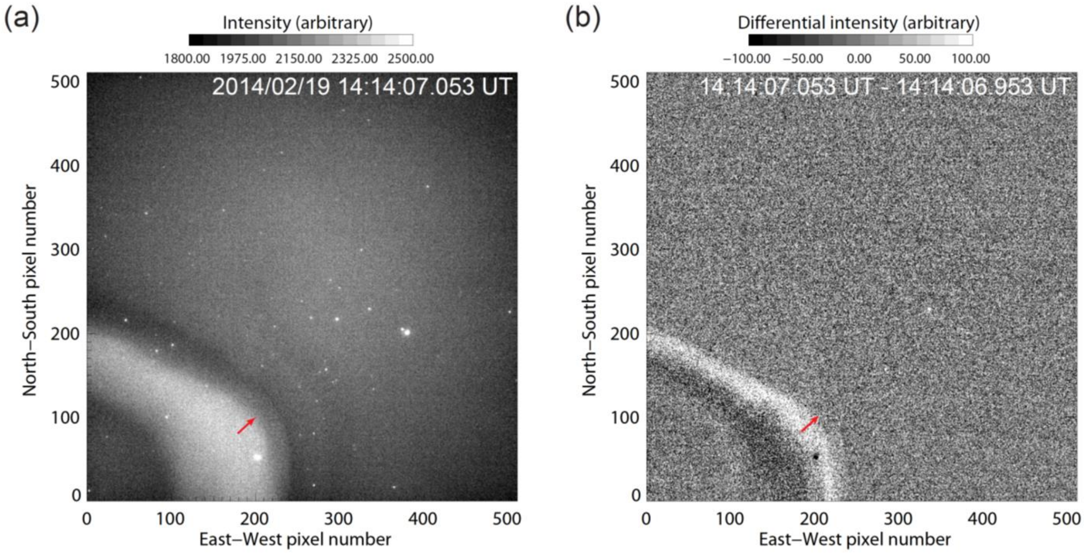

Figure 5.2: (a) High-speed image recorded at 14:14:07.053 UT, and (b) differential image between 14:14:06.953 and 14:14:07.053 UT.

Figure 5.3 shows the velocity distribution estimated from the 120 differential images. To allow later discussion of the formation mechanisms of the expanding motion considering compressional Alfvén waves, red circles indicate the projected Alfvén speed from the magnetosphere to the ionosphere. To estimate the "typical" Alfvén speed, we used an empirical model of electron density [*Sheeley et al.*, 2001], which is estimated as 4.9 cm^{-3} at 3.0 MLT in the magnetic equatorial plane at $L = 5.9$. It is found that approximately 80% of the propagation speeds are comparable to or less than the typical Alfvén speed. A few events have very fast motions of more than 150 km s^{-1}; some of these were observed at the onset of the ON-phase. **Figure 5.4** shows a snapshot of the non-repetitive expansion, which is one of the fastest examples with a speed of more than 200 km s^{-1}, keograms, and intensity variation around a center point (x = 420 and y = 91). The figure format is the same as in **Figure 5.1**. The fastest motion of the patch expansion appeared toward the southwest direction all over the FOV at ~14:21:03.4 UT, corresponding to the onset of the ON-phase as shown in **Figure 5.4c** to **5.4e**; this expansion is classified as non-repetitive expansion.

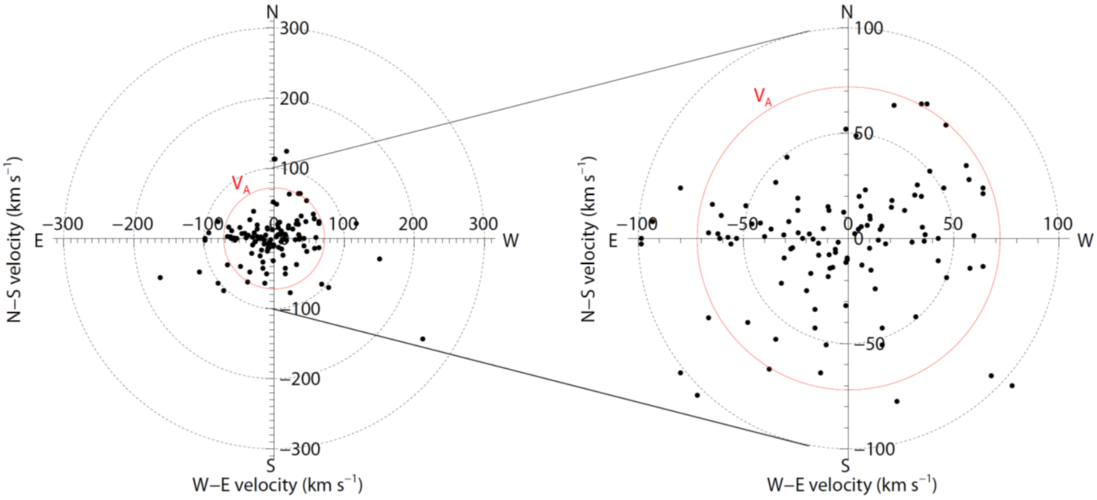

Figure 5.3: Velocity distribution and expanded plot only for speeds less than 100 km s^{-1}. The red circles indicate the projected Alfvén speed from the magnetosphere to the ionosphere at $L = 5.9$.

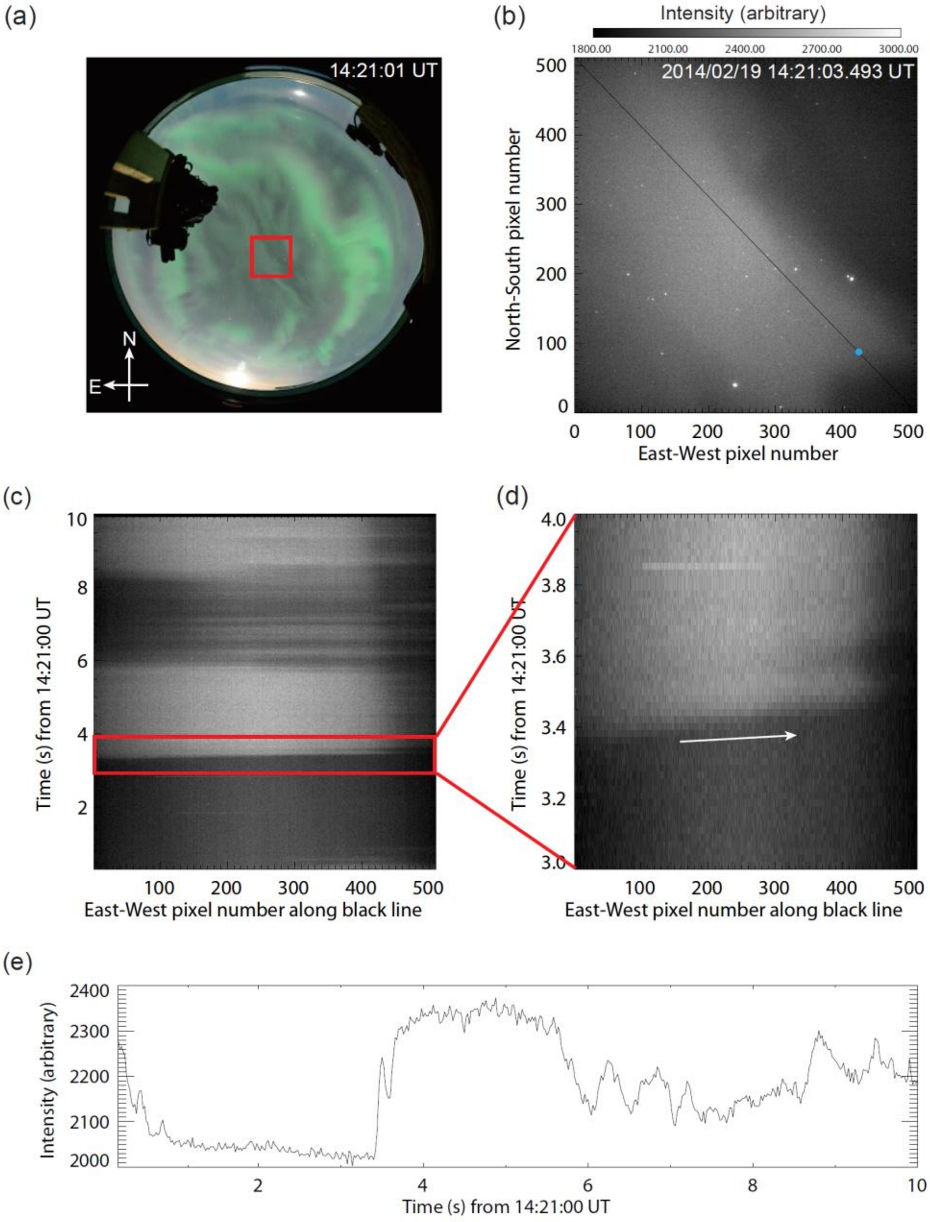

Figure 5.4: (a) All-sky image captured at 14:21:01 UT on 19 February 2014. (b) Example of fastest motion of non-repetitive expansions in the ON-phase. (c) Keogram aligned at the black line shown in **Figure 5.4b** for 10 s. (d) Extended keogram between 14:21:03 and 14:21:04 UT. (e) Averaged auroral intensity of the 5 × 5 pixels region centered at x = 420 and y = 91.

Interestingly, some expansions are obviously detached from the deformed main patches as shown in **Figure 5.5**. Both edges of an oblique north–south band repetitively expand, and some expansions are occasionally detached from the eastern edge of the deformed band from 14:56:04.5 to 14:56:05.5 UT, at around 14:56:06.5UT and after 14:56:08 UT. The frequencies are approximately 2 to 4 Hz, as shown by arrows in **Figure 5.5e**. An eastward detached expansion is represented by a white arrow in **Figure 5.5d**. The average speed is approximately 40 km s^{-1}, which is also less than the typical Alfvén speed.

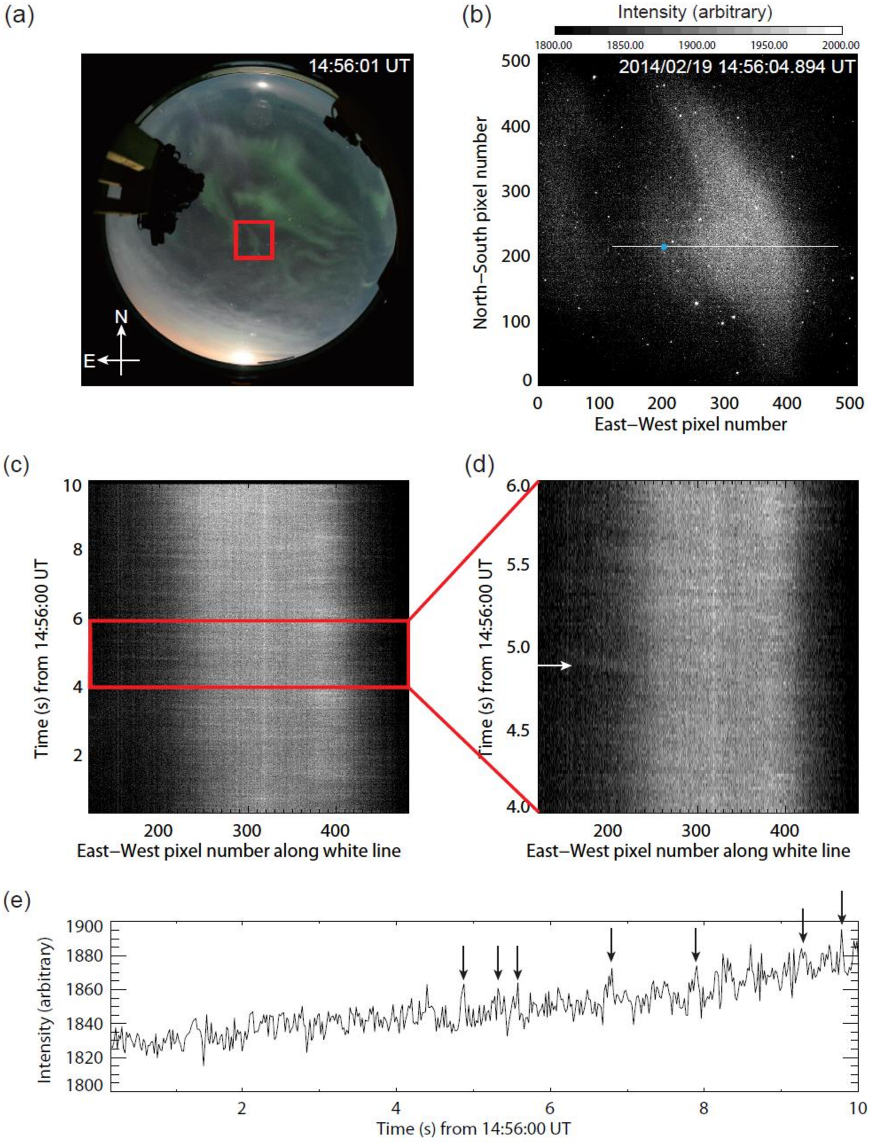

Figure 5.5: (a) All-sky image captured at 14:56:01 UT on 19 February 2014. (b) Example of detached expansions from the main deformed pulsating patch. (c) Keogram aligned at the black line shown in **Figure 5.5b** for 10 s. (d) Extended keogram between 14:56:04 and 14:56:06 UT. (e) Averaged auroral intensity of the 5 × 5 pixels region centered at x = 208 and y = 214.

Figure 5.6 shows the numbers of occurrences of directions of patch motion. If a patch expands self-similarly, we cannot determine a particular direction. We do not include such data in **Figure 5.6**. The expansions along the east–west direction and the northwest–southeast direction are dominant.

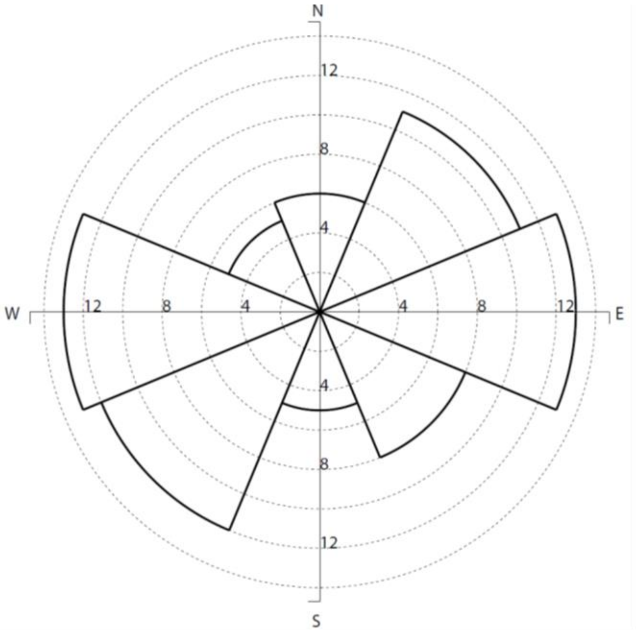

Figure 5.6: Numbers of occurrences of the directions of patch expansions.

5.3 Discussion

Our observational results showed that most of the propagation speeds of the pulsating aurora are tens of km s^{-1}, comparable to or less than the typical Alfvén speed, and that the expansions are predominantly along the east–west direction. The propagation velocities of the pulsating aurora have been quantitatively studied for approximately 40 years. For instance, *Yamamoto and Oguti* [1982] reported that the typical speeds of auroral patches are 20–50 km s^{-1} in the north–south direction and 30–100 km s^{-1} in the east–west direction. The typical propagation velocities are generally consistent with our results, although previous studies using all-sky TV cameras focused on global-scale and mesoscale movements on spatial scales from several tens to 2000 km and time scales of a few seconds.

We now discuss the meaning of the expansion speed of the patch associated with the 3 ± 1 Hz modulation. We assume that the resonant interaction of electrons with chorus elements produces both the expanding motion and the quasi-periodic 3 ± 1 Hz modulation of the pulsating patches. In this case, the speed of obliquely propagating chorus elements perpendicular to the magnetic field is projected as the expansion speed of a patch in the ionosphere. Although the chorus elements propagate along the magnetic field line with an angle of approximately 10° in the vicinity of the geomagnetic equator [*Santolík et al.*, 2003], they deviate from the magnetic field with increasing magnetic latitude to become nearly perpendicular at approximately 20° MLAT [*Agapitov et al.*, 2011]. *Li et al.* [2010] presented statistical global distributions of the characteristics of chorus waves and the conditions of background plasmas. From figure 1 of their statistical results, we can read that the ratio between the electron plasma frequency and the gyrofrequency, f_{pe}/f_{ce}, is approximately 3.0 in our observational situation with an *AE* index decrease from 650 nT to 100 nT at $L = 5.9$ in the nightside. According to the Appleton-Hartree equation [e. g., *Stix*, 1992], the group velocity of the parallel propagating chorus waves has the maximum at $f = 0.25f_{ce}$. The maximum group velocity at $f = 0.25f_{ce}$ is 0.21 c, where c is the speed of light, when f_{pe}/f_{ce} is 3.0, which is approximately 45 times faster than the local Alfvén wave at the equator. The perpendicular speed of the oblique chorus wave with a wave vector angle of 10° is more than eight times larger than the local Alfvén speed at the equator. The projected speed at the ionosphere is faster than 500 km s^{-1}. Therefore, the expanding motions are not likely to be the projection of obliquely propagating chorus elements. It should be noted, however, that there is no doubt that the chorus element contributes to cause the quasi-periodic modulation of 3 ± 1 Hz.

As another candidate explanation for the expanding motions, we discuss the possibility of projected compressional Alfvén waves, because the origin of the pulsating aurora is considered to be located near the magnetic equator and they are one of general plasma waves in the region. We consider that the compressional wave possibly changes the density spatial distribution of electrons, which undergo the pitch angle scattering by the chorus wave, and controls the spatial motion of the pulsating patch by the wave propagation [*Cresswell*, 1968]. Both slow-mode and fast-mode Alfvén waves can be excited by the hot plasma injections associated with substorms at the localized high-β region [e.g., *Jaynes et al.*, 2015; *Li et al.*, 2005; 2011]. Considering a margin of error of the estimated electron density of 4.9 ± 3.5 cm^{-3}, the range of projected Alfvén speeds is between 55 and 132 km s^{-1} at the ionosphere.

As approximately 80% of all expansion speeds are equal to or less than the local Alfvén speed, there are two possibilities to explain the rapid motions of pulsating features by compressional Alfvén waves. If the expansion is formed by slow mode, the propagation speed is less than the local Alfvén waves. Here, we examine the perpendicular wavelengths of the oblique slow-mode waves using the assumption that the wave frequency is 3 Hz in the region of plasma $\beta \sim 1$. If the slow-mode wave forms fine-scale structures less than 10 km, such as the expanding motion, the propagation angle to the local magnetic field must be larger than 60°, which is consistent with the observed values. At the given propagation angle, the higher the frequency of a wave, the smaller a structure the wave can produce in the perpendicular direction. To confirm the existence of high-frequency slow-mode Alfvén waves, capturing the density and magnetic field variations at high time cadence will be necessary; however, this is still challenging.

If the expansion is formed by fast mode, the propagation speed is greater than that of the local Alfvén waves. Some events show rapid motion faster than the local Alfvén speed, especially over 150 km s^{-1}.

Although the speeds are similar to the fast auroral waves already mentioned in Section 5.1, the equatorward propagation that is reported to be a property of fast auroral waves is very rare as shown in **Figure 5.3**. The generation mechanism of such fast motions with long displacement appears to be different from that of the expanding motions with speeds of tens of km s^{-1}. On the basis of the observed speeds, a possible cause of the fast motions is fast-mode Alfvén waves propagating across the field line, as suggested by *Cresswell* [1968].

The expansion motions, particularly the motions accompanied with the detached structure as shown in **Figure 5.5**, sporadically appeared. The sporadic signature is consistent with the possibility that the 3-Hz modulation with the rapid spatial motion is formed not only by the chorus elements but also by the compressional Alfvén wave in the magnetic equator. The reason why the expansions are dominant along the east–west direction is unsolved. However, it possibly shows that our ground-based observation visualizes the compressional waves propagating along a longitudinal direction in the magnetic equator. If the mechanism associated with the Alfvén waves is established, monitoring the rapid motion around pulsating features may be useful to diagnose the complex Alfvén wave activity in the magnetosphere.

Our camera system can capture rapid motions with frequencies of up to 25 Hz due to the Nyquist frequency. **Figure 5.7** shows an example of a spectral intensity map derived for the second event from FFT analysis at each pixel, as described by *Kataoka et al.* [2012; 2015]. The spectral amplitudes are normalized at each frequency from 1 to 24 Hz. The quasi-periodic modulation of the pulsating aurora is present at 2 to 6 Hz, and the rapid motions associated with the modulation, which are “apparent” patterns, appear at up to 20 Hz. The “apparent” patterns are mostly related to the rapid motion at the edges of pulsating patches, and are probably not due to a pure temporal intensity modulation.

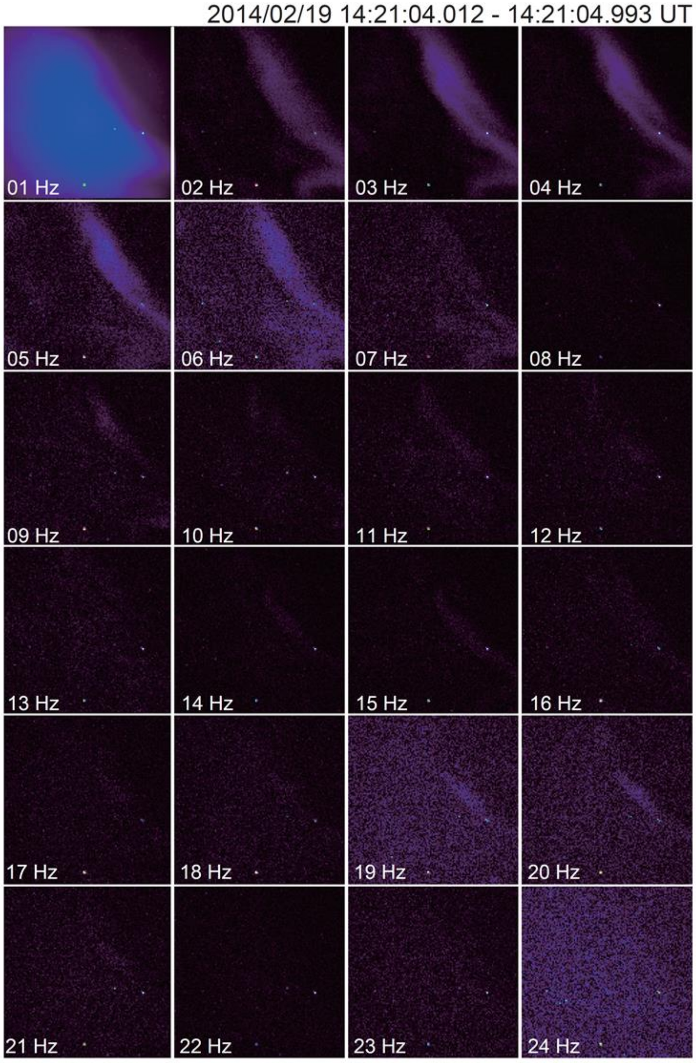

Figure 5.7: Fourier spectral intensity map at 14:21:04 to 14:21:05 UT on 19 February 2014.

From a 500 fps observation, a pulsating aurora with much faster (up to 54 Hz) intensity modulation has been reported [*Kataoka et al.,* 2012], which was caused by pure temporal variation. Their study suggested that the time scale of the faster temporal variation is close to a repetitive frequency of subpackets inside a chorus element. In contrast to their study, our results indicate that the rapid intensity modulation is caused by the spatiotemporal variation. The mimicking intensity modulation that is much faster than the 3 ± 1 Hz modulation is a faulty result of the FFT analysis, since the intensity modulation is possibly caused by the rapid spatial variations. It is therefore important to distinguish between rapid spatial motions and temporal intensity variations to associate the different morphologies with their respective generation mechanisms.

As another approach to extract the spatial structures and temporal variations, *Nishiyama et al.* [2016] applied principal component analysis and FFT analysis to the rapidly varying pulsating aurora. They showed that the pulsating patch consisted of two components: the whole patch structure with ON–OFF switching toward equatorward and sub-structures with the back and forth motion at 3 Hz during the ON-phase. These spatial motions are similar with what we focused in this study, although they concluded that the spatiotemporal property with two components is closely related to the generation and propagation process of the chorus waves.

As an interesting example, event 3 shows peeling structures propagating away from the patch, which may resemble to the splitting/bifurcating arc phenomenon previously reported by *Semeter et al.* [2006; 2008]. They interpreted the splitting of fine structured auroras to be due to dispersive Alfvén waves, and they reported similar frequencies and expansion speeds as we do. It would be interesting to see somewhat similar auroral appearance in both diffuse auroras and in discrete auroras, which may be connected by Alfvén waves.

Our observation was conducted only for the first 10 s of every minute because of the acquirable data amount during the winter season. There is a limitation which we only investigate one or two ON-phases since the observations period is not so long to identify the repetitive ON–OFF switching of the main patch. Even though a continuous observation is possible, we think our conclusions do not change, because the expanding features were continuously observed at least for 45 minutes in this study. In addition, each expanding is rapid feature than the 10-s observational period. Nevertheless, continuous observations may provide new insight into the transition of the expanding motions of the pulsating features during several ON-phases.

In this study, we focused on an active storm-time substorm event in which the rapid motions of the pulsating aurora were bright enough to be clearly identified. It is still an open question whether fainter pulsating patches during typical conditions have similar characteristics. More studies are necessary to understand the varieties of the pulsating aurora that appear at different conditions of magnetic local times, substorm phases, and auroral intensities.

5.4 Conclusions

During a storm-time substorm, rapid motions of pulsating features had typical speeds of tens of km s^{-1} at ionospheric altitudes, which are comparable to or less than the projected Alfvén speed from the magnetosphere to the ionosphere. The expansions are dominant along the east–west direction. The fastest non-repetitive events show expansion speeds of more than 150 km s^{-1}. These results suggest that the possible formation mechanism for the rapid motions associated with the 3 ± 1 Hz modulation of the pulsating aurora can explained not by the projection of the oblique propagating chorus elements but by both slow- and fast-mode Alfvén waves, although the chorus wave is needed to generate the quasi-periodic 3 ± 1 Hz modulation.

6 General Discussion

In this chapter, we comprehensively discuss the observational results obtained from Chapter 3 to 5.

In Chapter 3, in order to elucidate the generation mechanisms of the flickering aurora, we statistically investigate the occurrence property by using the ground-based high-speed imager designed for the continuous observation. As a basic property of the flickering aurora, it is found that the occurrence rate is basically proportional to the background non-flickering auroral intensity. This result is consistent with the excitation mechanisms by EMIC waves which have been thought to be driven by beam electrons within the acceleration region. The bright auroras without the flickering modulation occasionally appears as the isolated arc. Since the arc width corresponds to the horizontal scale of the acceleration region, the results suggest that it is hard to excite EMIC waves within a narrow acceleration region. Although the previous numerical studies [e.g., *Lund and Labelle*, 1997] could not explain the realistic wave excitation model due to the low growth rate in the linear homogeneous plasma, the ground-based imaging observation is probably possible to determine the threshold of the arc width to growth EMIC waves.

It is found that the flickering frequency is narrowband. This result is consistent with the satellite and the sounding rocket observations [e.g., *Gustafsson et al.*, 1990; *Erlandson and Zanetti*, 1988]. The signature of narrowband waves indicates that the resonance region is restricted at a particular altitude. Our result shows the increase in the peak frequency from <10 to ~20 Hz, which corresponds to the altitude variation from >5000 km to ~2500 km, before the substorm onset. These signatures of the peak frequency and the frequency width suggest that the flickering aurora occurs at the low-altitude acceleration region regardless the substorm phase, based on the two-step evolution of the acceleration region investigated by AKR [e.g., *Morioka et al.*, 2007]. This result shows that the low-altitude acceleration region would play an important role in the excitation of EIMC waves. The flickering frequency has no correlation with the background auroral intensity. This result is also consistent with the possibility that the resonant altitude is confined at the low-latitude acceleration region, because the auroral intensity generally tends to increase after the auroral breakup, as discussed above.

We also found that the flickering amplitude and the background auroral intensity is approximately the linear relation. Assuming that the Landau resonance interaction between EMIC waves and electrons occurs, the minimum flickering amplitude is possibly caused by the minimum phase velocity to resonate the electrons or caused by the minimum flux number to produce the flickering aurora, since the auroral intensity varies by the electron energy variation and by the electron flux variation. One of the possibilities to cause the variation of the flickering amplitude is the time variation of the peak energy of the FABs [*Arnoldy et al.*, 1999]. The signature of the peak energy variation of the FABs was investigated by using simulation studies to produce the inverted-V flux modulation by a DC potential drop and resonant acceleration due to the inertial Alfvén wave pulse [*Chen et al.*, 2005]. They concluded that the inverted-V electron flux is efficiently modified when the velocity of the inverted-V electrons is comparable to or smaller than the peak Alfvén speed. Assuming that the energy of the inverted-V electrons is proportional to the auroral intensity, the flux modulation becomes weaken with the auroral intensity. This tendency is qualitatively consistent with the inverse variation of the flickering amplitude ratio and the background auroral intensity.

Figure 6.1 represents a schematic illustration of the necessary condition to generate the flickering aurora depending on the width of the horizontal potential structures.

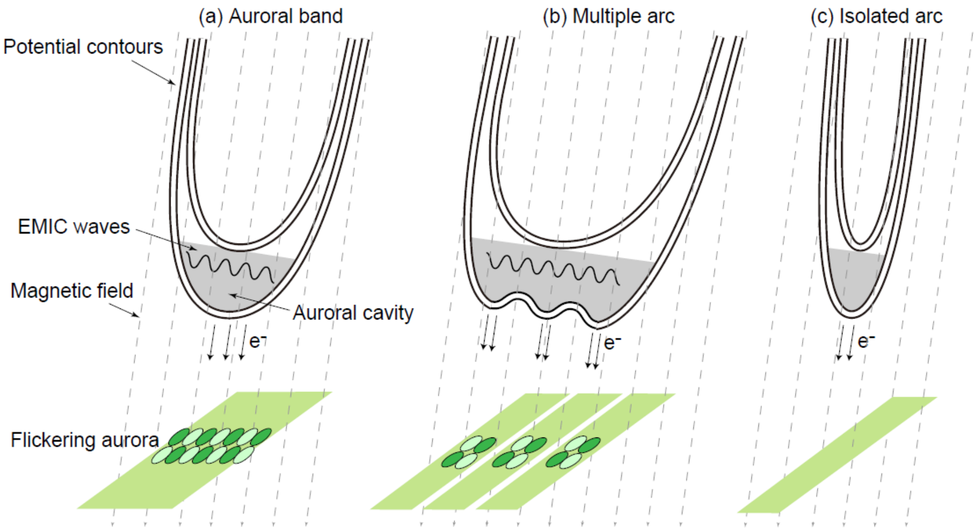

Figure 6.1: Schematic illustration of necessary conditions to occur the flickering aurora. Each case represents an auroral band (a), a multiple arc (b), and an isolated arc (c), respectively.

In Chapter 4, in order to investigate the frequency property, 2D images of the fastest ever observed flickering aurora with frequencies exceeding 80 Hz were obtained from ground-based high-speed observations. The most plausible generation mechanism in the M–I coupling region, is H^+-band EMIC waves. The observational results show that the typical flickering frequency was approximately 10 Hz, and thus, the resonance altitude between electrons and O^+-EMIC waves can be estimated as 6000 km. Therefore, the frequency range of H^+-EMIC waves with propagation angles of 0–90° is 40–160 Hz given the assumption that all the multi-ion EMIC waves resonate electrons at the same altitude of 6000 km. It is observed that the frequency of the observed fastest flickering aurora corresponds to the lower frequency range of H^+-EMIC waves. If the proposed hypothesis was true, much faster flickering aurora with the higher frequency range can also be detected in future by a higher speed imaging than that of the observations in the present study.

We also showed that the resonance energy to satisfy the Landau resonance condition estimated from the frequency and the wavenumbers is consistent with the energy range of the inverted-V electrons. *Whiter et al.* [2010] reported that the electron energy to cause the flickering aurora exceeds the peak energy of the inverted-V electrons. They discussed the acceleration mechanism of flickering auroras by EMIC waves above auroral acceleration regions as one of the possible reasons. Our estimations of the resonance energy associated with EMIC waves, however, are lower than the previous study shown by *Whiter et al.* [2010]. These results indicate that the Landau resonance condition was possibly satisfied at the auroral acceleration altitude.

Previous studies demonstrated the detectability of H^+-band EMIC waves by using ray tracing calculations [*Lund and LaBelle*, 1997]. The results indicated that H^+-band EMIC waves with a normal wave angle <10° can propagate to lower ionospheric altitudes as the source altitude decreases, though EMIC waves were significantly attenuated when compared with O^+-band EMIC waves. The propagation properties are consistent with the observational result that the flickering aurora associated with H^+-band EMIC waves was rarely observed when compared with that of the traditional O^+-band EMIC wave.

The temporal variation such as the sporadic appearance of the flickering aurora on a time scale of 0.1 s is likely to originate from the rapid appearance and disappearance of the multi-ion EMIC waves. Due to such a sporadic appearance, the resonance altitude or the total electron density cannot be uniquely decided. These results potentially indicate that the generation mechanism is beyond the linear theory of multi-ion EMIC waves, and that it is necessary to consider nonlinear wave emission in the inhomogeneous plasma. Our results demonstrated in this study nonetheless are consistent with the hypothesis that flickering auroras are produced by multi-ion EMIC waves considering nonlinear theory as shown in **Figure 6.2**. However, our study could not explain the excitation mechanism of the sporadic multi-ion EMIC waves based solely on the high-speed imaging observation. A future study should include the high-speed imaging observation as well as the simulation study to reproduce observational evidence with a complicated spatiotemporal variation.

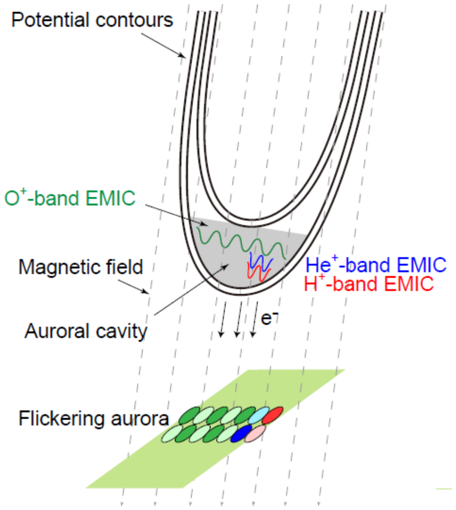

Figure 6.2: Schematic illustration of generation mechanisms of the fastest flickering aurora by multi-ion EMIC waves.

Our results obtained from Chapter 3 to Chapter 4 suggest that flickering auroras are caused by the Landau resonance interaction with multi-ion EMIC waves at the low-altitude acceleration region with the broad horizontal scale. The generation mechanisms of the flickering aurora can be represented as shown in **Figure 6.3**.

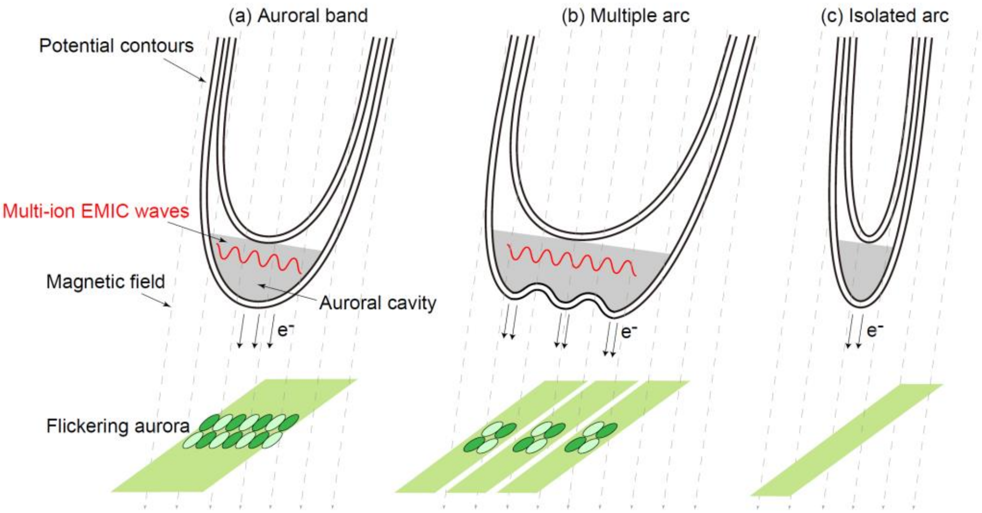

Figure 6.3: Schematic illustration of generation mechanisms of the flickering aurora by multi-ion EMIC waves.

In Chapter 5, we investigate the rapid moving features of the pulsating aurora as an application of the high-speed imaging observation, since spatial variation in pulsating patches associated with the 3 Hz intensity modulation has rarely been reported, except by *Nishiyama et al.* [2016]. During a pulsation ON-phase, repetitive expansions are often observed around the edges of pulsating patches. Approximately 80% of all the deduced expansion speeds were less than 70 km s^{-1} at ionospheric altitudes, which is less than the projected Alfvén speed from the magnetospheric equator to the ionosphere. Rapid motions with speeds of tens of kilometers per second are unlikely to be explained by obliquely propagating chorus elements, which are known to cause 3 Hz modulation, as a result of the calculation of the perpendicular speed of the oblique chorus waves.

We discussed two possibilities to explain the rapid spatial motions of pulsating features by compressional Alfvén waves, which possibly changes the spatial distribution of electron density. The electron is scattered by the chorus wave, and then is changed their density distribution by the propagation of slow-mode waves and fast-mode waves [*Cresswell*, 1968]. The density variation can be considered as the spatial motion of the pulsating aurora. Some events showed a few detached expansions traveling away from the main deformed pulsating patch. The differences in the expansion speeds indicated two different formation mechanisms for the patch motions. We showed that ground-based, high-speed, fine-scale observations were also useful for visualizing the wave-particle interaction that occurred near the magnetic equator region.

7 General Conclusions

In this thesis, the generation mechanism for a flickering aurora was studied using ground-based high-speed observations. The most important results of this thesis and future works are summarized below.

7.1 Summary of this thesis

- Development of continuous ground-based high-speed imaging system

Continuous high-speed fine-scale observations have previously been thought to be difficult because of the need to store extremely large quantities of data. In order to resolve this problem, I designed a new observational system that is automatically controlled by a real-time auroral auto-detection based on a machine learning technique. The auroral auto-detection performance was 80% in comparison with the results determined by eye, and it could decrease the data amount by 75%. We finally enabled a continuous observational system with a spatial resolution of ~50 m at an altitude of 100 km and a temporal resolution of 320 fps over three winter seasons.

- Basic property of flickering aurora

In order to elucidate the generation mechanisms of a flickering aurora, we statistically investigate the occurrence property for the first time by using the auto-detection of the flickering aurora. The flickering appearance is approximately proportional to the background non-flickering auroral intensity. The peak frequency gradually increases during the time period before the substorm onset. The flickering frequency is narrowband and independent with the background auroral intensity. A bright aurora without the flickering structure had a property of the isolated arc. These results suggest that EMIC waves are consistent with the excitation mechanisms which has been thought to be driven within the acceleration region, and that the flickering aurora is generated at the low-latitude acceleration region with the broad horizontal scale. Although the results of numerical studies on the wave growth process of EMIC waves within the auroral acceleration region have been inconsistent in realistic conditions, these observational results may provide insight into the generation mechanisms of EMIC waves.

We also showed, for the first time, that the flickering amplitude (count) is proportional to the background non-flickering intensity, and that the flickering amplitude (%) varies inversely with the background non-flickering auroral intensity. This result suggests that there is likely to be exist the minimum phase velocity to resonate the electrons or the minimum flux number to produce the flickering aurora.

- Fastest flickering frequency

For the first time, the high-speed imaging observation at 160 fps simultaneously detected the fastest flickering modulation that can be generated by an H^+-band EMIC wave and the traditional flickering modulation at the O^+ gyrofrequency. These results exactly support the conclusion that the flickering aurora is generated by EMIC waves that is excited in the multi-species plasma. We also showed that the Landau resonance condition is satisfied by using the estimated frequencies and wavenumbers.

- Application of high-speed imaging observations

Rapidly moving features of the pulsating aurora were investigated as an application of the high-speed imaging observation. During a pulsation ON-phase, repetitive expansions are often observed around the edges of pulsating patches. Approximately 80% of all the deduced expansion speeds were less than 70 km s^{-1} at ionospheric altitudes, which is less than the projected Alfvén speed from the magnetospheric equator to the ionosphere. Rapid motions with speeds of tens of kilometers per second are unlikely to be explained by obliquely propagating chorus elements, which are known to cause 3 Hz modulation, because the perpendicular speed of the oblique chorus waves is faster than the Alfvén speed. We suggest that the slow-mode Alfvén wave as a candidate to modulate the electron density distribution to generate these rapid spatial motions. Some events showed the expansion speed over150 km s^{-1}. We showed that ground-based, high-speed observations were also useful for visualizing the wave-particle interaction that occurred near the magnetic equator region.

7.2 Future Work

In this thesis, we could neither statistically investigate the threshold of the flickering appearance nor quantitatively discuss the excitation of EMIC waves. In terms of a comprehensive understanding of the physical process within the acceleration region, we need to research the differences in the occurrence conditions between a flickering aurora and other fine-scale auroral motions, which are both formed by DAWs, as shown by *Semeter et al.* [2006]. In addition, a study of the flickering appearance using broad FOV images may be important to obtain a picture of the excitation of EMIC waves in a mesoscale auroral structure, although only narrow FOV images were used in this thesis. Because 100° × 100° FOV images that show flickering auroras have already been acquired, we can start comparative studies of the auroral morphology on the global scale by using ground-based THEMIS all-sky imagers or DMSP satellites.

The previous studies on the energy property of the precipitated electrons that create a flickering aurora have not been sufficient to understand the interaction between an electron and EMIC waves. To investigate the electron energy based on ground-based observations, multi-spectral cameras with high spatiotemporal resolutions are necessary. In addition, ground-based high-speed stereoscopic observations would also be useful for identifying auroral emission heights, as shown by *Kataoka et al.* [2016]. The most effective method would be simultaneous observations using satellites monitoring waves and particles within or below the acceleration region and ground-based high-speed imagers. More particularly, we need to test the similarity of the frequencies between the electron flux modulation, EMIC waves, and the auroral intensity modulation, to confirm the existence of the TOF effect of the FAB, and to estimate the source altitude of the FAB. We finally check the consistency of the flickering frequency and the local cyclotron frequency at the source altitude of the FAB. These detailed investigations of the one-to-one correspondence between the electron flux modulations, EMIC waves, and auroral intensity modulation is sure to clarify the wave-particle interaction inside or around the acceleration region. Our results of the fastest flickering aurora show that the time resolution of 160 fps was not enough to detect the modulation generated by H^+-band EMIC waves. When the O^+ gyrofrequency is assumed to be 20 Hz, a sampling rate faster than 320 fps is essential. Comparative studies between these high-speed fine-scale imaging and high-resolution radar observations such as EISCAT_3D would provide new insights to comprehend the fine-scale auroral morphology.

Appendix: EMIC wave in Multicomponent Plasma

We consider a cold plasma consisting of electrons and various types of ions with an externally imposed static uniform magnetic field. The quantities of *S*, *D*, and *P* which are component of a dielectric tensor are defined as follows:

$$S = (R + L)/2\,, \qquad D = (R - L)/2$$

$$R = 1 - \sum_{\alpha} \frac{X_\alpha}{1 + \epsilon_\alpha |Y_\alpha|}$$

$$L = 1 - \sum_{\alpha} \frac{X_\alpha}{1 - \epsilon_\alpha |Y_\alpha|}$$

$$P = 1 - \sum_{\alpha} X_\alpha$$

The subscript α stands for the αth particles, and ϵ_α is the sign of the charge. X_α and Y_α are given by

$$X_\alpha = \left(\frac{\omega_{p,\alpha}}{\omega}\right)^2 \text{ and } Y_\alpha = \frac{\omega_{c,\alpha}}{\omega}.$$

Assuming the magnetic field of $\boldsymbol{B_0}$ is parallel to the z-axis and the refraction vector $\boldsymbol{n}$ which is parallel to wave vector $\boldsymbol{k}$ is in the x-z plane at an angle θ relative to $\boldsymbol{B_0}$, $\boldsymbol{k}$ becomes $(k\sin\theta,\ 0,\ k\cos\theta)$. If the determinant of the matrix of the wave equation is zero, the dispersion relation can be written in the form

$$An^4 - Bn^2 + PRL = 0,$$

where

$$A = Ssin^2\theta + Pcos^2\theta$$

$$B = RLsin^2\theta + PS(1 + cos^2\theta).$$

This equation is a quadratic in n^2 and can be solved using the quadratic formula, which gives

$$n^2 = \frac{B \pm F}{2A},$$

where the term *F* can be written in the positive definite form

$$F^2 = (RL - PS)^2 sin^4\theta + 4P^2D^2cos^2\theta.$$

The relation of θ is given by

$$tan^2\,\theta = -\frac{P(n^2 - R)(n^2 - L)}{(Sn^2 - RL)(n^2 - P)}.$$

When the wave propagates parallel to the magnetic field, $\theta=0$, in the three-ion plasma (H^+, He^+, and O^+), the dispersion relation of two modes can be obtained as bellow:

$$n_R^2 = R = 1 - \frac{\omega_{pe}^2}{\omega^2}\frac{1}{1-\omega_{ce}/\omega} - \frac{\omega_{pH^+}^2}{\omega^2}\frac{1}{1+\omega_{cH^+}/\omega} - \frac{\omega_{pHe^+}^2}{\omega^2}\frac{1}{1+\omega_{cHe^+}/\omega} - \frac{\omega_{pO^+}^2}{\omega^2}\frac{1}{1+\omega_{cO^+}/\omega},$$

$$n_L^2 = L = 1 - \frac{\omega_{pe}^2}{\omega^2}\frac{1}{1+\omega_{ce}/\omega} - \frac{\omega_{pH^+}^2}{\omega^2}\frac{1}{1-\omega_{cH^+}/\omega} - \frac{\omega_{pHe^+}^2}{\omega^2}\frac{1}{1-\omega_{cHe^+}/\omega} - \frac{\omega_{pO^+}^2}{\omega^2}\frac{1}{1-\omega_{cO^+}/\omega}.$$

The n_R^2 indicates the index of the refraction of right-hand (R mode) polarized waves, and represents whistler mode waves propagating with the frequency range of $\omega < \omega_{ce}$. The n_L^2 indicates the index of the refraction of left-hand (L mode) polarized waves, and represents EMIC waves propagating with the frequency range of $\omega < \omega_{ci}$. The whistler wave is not relatively affected by the presence of heavier ions; however, EMIC waves in the multi-ion plasma has characteristic frequencies. For finite $k_\perp$, the two modes couple at a crossover frequency ω_{co} ($L = R$), and the L mode branch approaches a cutoff frequency ω_{cut} ($L = 0$) as $k_{/\!/} \rightarrow 0$. For $k_\perp = 0$, the two modes coexist at this frequency, and ion hybrid resonance occurs at an ion hybrid resonance frequency ω_h ($R + L = 0$). These frequencies between two ion gyrofrequencies, ω_{ci1} and ω_{ci2}, represent a magnitude relationship as follow: $\omega_{ci1} < \omega_h < \omega_{cut} < \omega_{co} < \omega_{ci2}$, and are generally depending on the total plasma density and the ion composition ratio.

Figure A.1-3 show the dispersion relations of EMIC waves with the propagation angle of 0°, 45°, 60°, 89° in the three-ion plasma (H^+, He^+, and O^+). **Figure A.1** represents the dependence of the different total electron densities, 0.1, 10, and 1000 cm^{-3}, when the altitude and the ion composition ratio are 3500 km and $H^+ : He^+ : O^+ = 50 : 10 : 40$, respectively. The density variation is assumed to be within and outside the auroral cavity. It can be seen that gradients of the dispersion relations at small perpendicular wavenumbers are significantly modified by the total electron number. **Figure A.2** exhibits the dependence of the altitude, 3500 km, 5000 km, and 6500 km, when the total electron density and the ion composition ratio are 0.1 cm^{-3} and $H^+ : He^+ : O^+ = 50 : 10 : 40$, respectively. The altitude is assumed to be the auroral acceleration region. It is clear that the altitude mainly changes the resonance frequency depending on the magnetic field strength. **Figure A.3** shows the dependence of the ion composition ratio, $H^+ : He^+ : O^+ = 50 : 30 : 20$, $70 : 10 : 20$, and $20 : 40 : 40$, when the total electron density and the altitude are 0.1 cm^{-3} and 3500 km, respectively. Although these ratios also include unrealistic conditions, it can be seen that the ratio variation makes slight changes of the gradient of the dispersion relations.

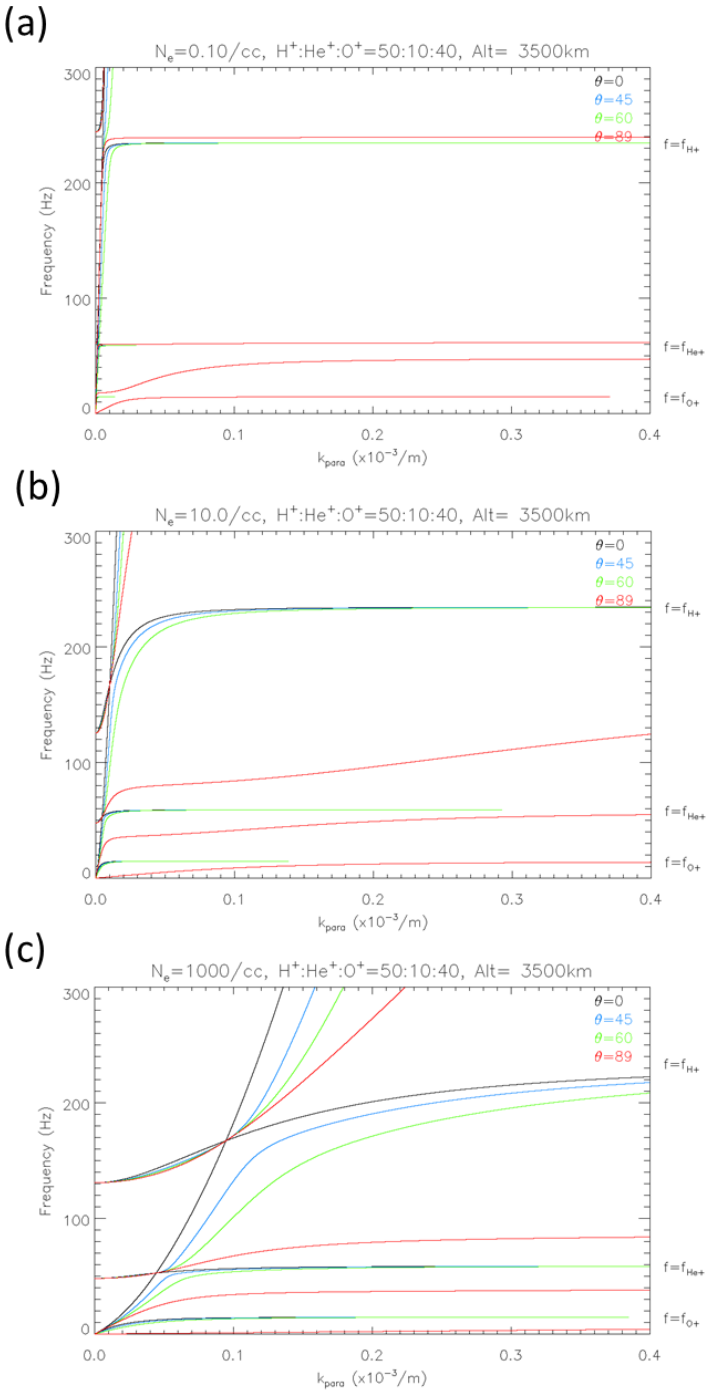

Figure A.1: A dependence of the total electron density ((a) 0.1 cm^{-3}, (b) 10 cm^{-3}, and (c) 1000 cm^{-3}) on the dispersion relations of EMIC waves in the multicomponent plasma, when the ion composition ratio is H$^+$: He$^+$: O$^+$ = 50 : 10 : 40, and the altitude is 3500 km.

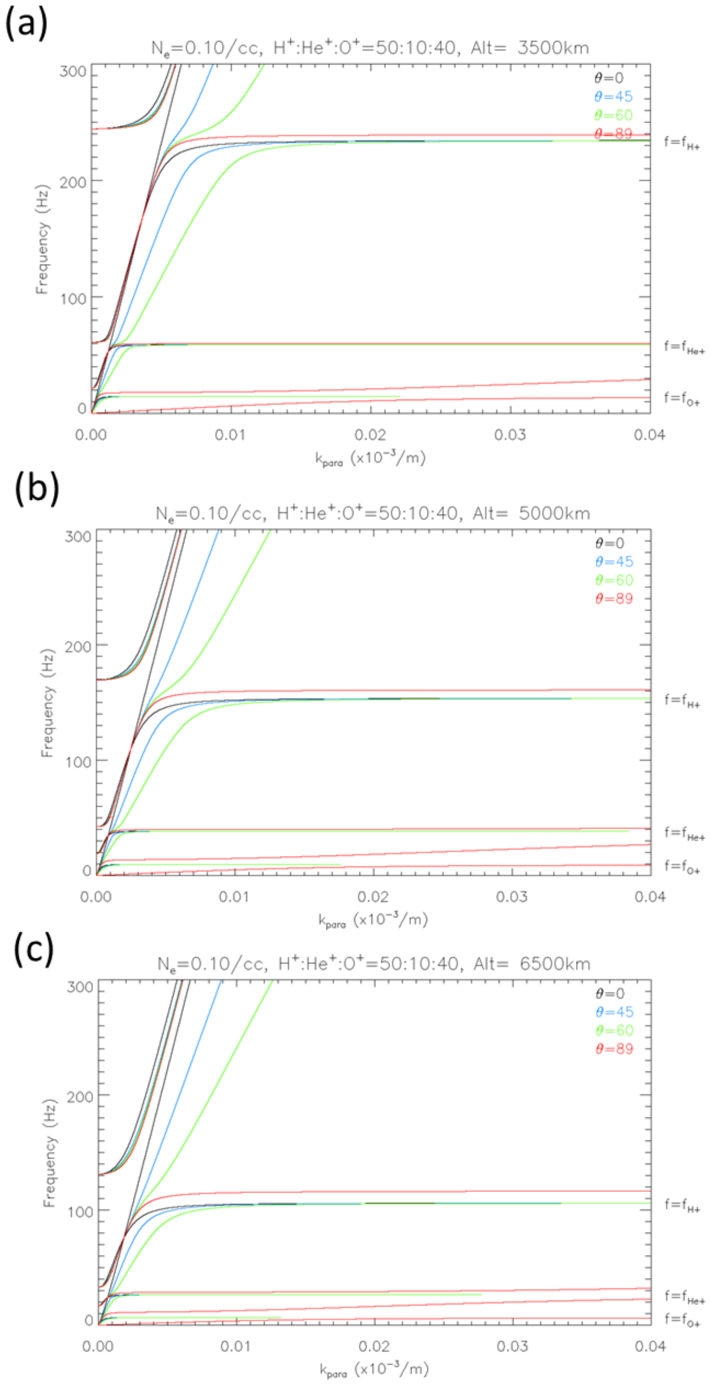

Figure A.2: A dependence of the altitude ((a) 3500 km, (b) 5000 km, and (c) 6500 km) on the dispersion relations of EMIC waves in the multicomponent plasma, when the total density is 0.1 cm^{-3} and the ion composition ratio is H$^+$: He$^+$: O$^+$ = 50 : 10 : 40.

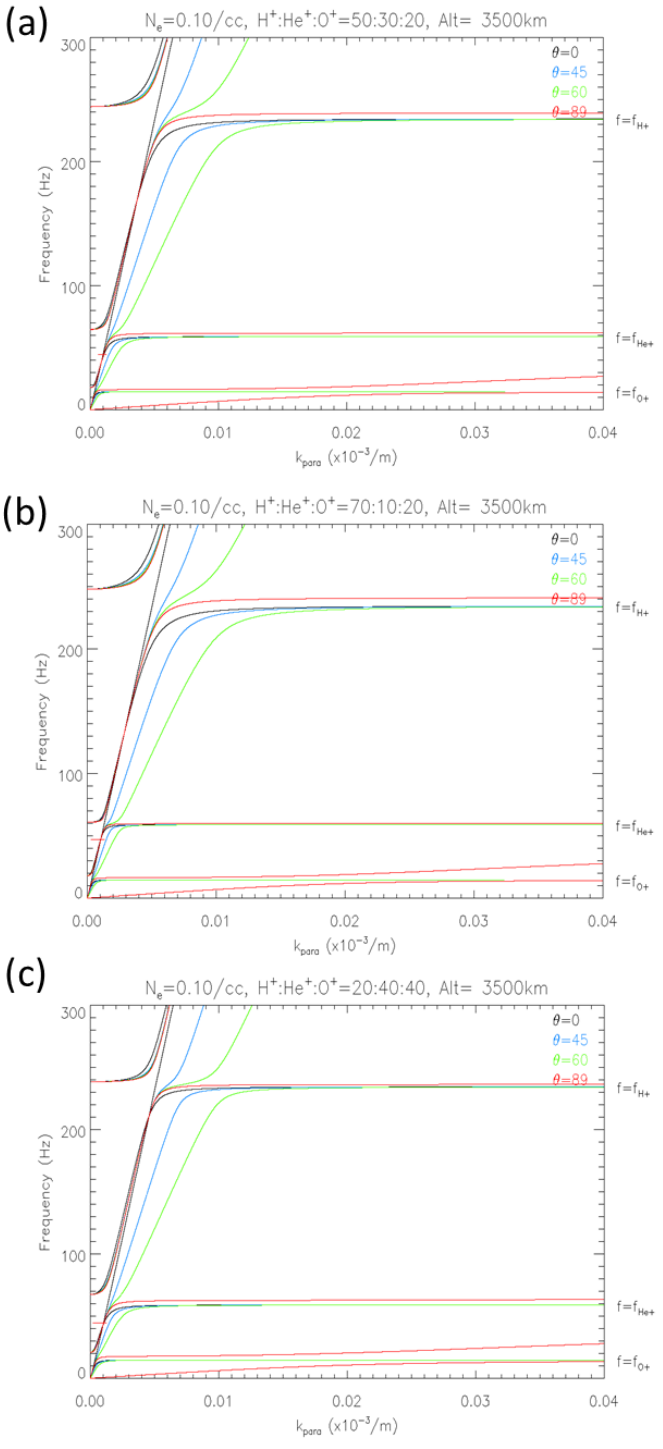

Figure A.3: A dependence of the ion composition ratio ($H^+ : He^+ : O^+$ = (a) 50 : 30 : 20, (b) 70 : 10 : 20, and (c) 20 : 40 : 40) on the dispersion relations of EMIC waves in the multicomponent plasma, when the total density is 0.1 cm^{-3} and the altitude is 3500 km.

References

Agapitov, O., V. Krasnoselskikh, Y. V. Khotyaintsev, and G. Rolland (2011), A statistical study of the propagation characteristics of whistler waves observed by Cluster, *Geophys. Res. Lett.*, 38, L20103.

Akasofu, S.-I. (1964), The development of the auroral substorm, *Planet. Space Sci.*, 12, 273–282.

Akasofu, S.-I. (1976), Recent progress in studies of DMSP auroral photographs, *Space Sci. Rev.*, 19, 169.

Arnoldy, R. L. (1970), Rapid fluctuations of energetic auroral particles, *J. Geophys. Res.*, 75(1), 228–232, doi:10.1029/JA075i001p00228.

Arnoldy, R. L., K. A. Lynch, J. B. Austin, and P. M. Kintner (1999), Energy and pitch angle-dispersed auroral electrons suggesting a time-variable, inverted-V potential structure, *J. Geophys Res.*, 104, 22, 613.

Asamura, K., et al. (2009), Sheared flows and small-scale Alfvén wave generation in the auroral acceleration region, *Geophys. Res. Lett.*, 36, L05105, doi:10.1029/2008GL036803.

Beach, R., G. R. Cresswell, T. N. Davis, T. J. Hallinan, and L. R. Sweet (1968), Flickering, A 10-cps fluctuation within bright auroras, *Planet. Space Sci.*, 16, 1525.

Borovsky, J. E. (1993), Auroral arc thickness as predicted by various theories, *J. Geophys. Res.*, 98, 6101–6138.

Boyd, J. S., and T. N. Davis, N. B. Brown, T. J. Hallinan, and D. D. Wallis (1972), Observations of fast auroral waves, *Planet. Space Sci.*, 20, 437–440, doi:10.1016/0032-0633(72)90041-4.

Berkey, F. T., M. B. Silevitch, and N. R. Parsons (1980), Time sequence analysis of flickering auroras: 1. Application of Fourier analysis, *J. Geophys. Res.*, 85, 6827.

Chang, C. C., and Lin, C. J. (2011), LIBSVM: a library for support vector machines, *ACM Transactions on Intelligent Systems and Technology (TIST)*, 2(3), 27.

Chaston, C. C., and K. Seki (2010), Small-scale auroral current sheet structuring, *J. Geophys. Res.*, 115, A11221, doi:10.1029/2010JA015536.

Chen, L.-J., C. A. Kletzing, S. Hu, and S. R. Bounds (2005), Auroral electron dispersion below inverted-V energies: Resonant deceleration and acceleration by Alfvén waves, *J. Geophys. Res.*, 110, A10S13, doi:10.1029/2005JA011168.

Cresswell, G.R. (1968), Fast auroral waves, *Planet. Space Sci.,* 16, 1453–1464, doi:10.1016/0032-0633(68)90058-5.

Cresswell, G. R. (1972), The morphology of displays of pulsating auroras, *J. Atmos. Terr. Phys.,* 34, 549–554. doi:10.1016/0021-9169(72)90058-X.

Cresswell, G. R. and A. E. Belon (1966), Observations of fast auroral waves, *Planet. Space Sci.,* 14, 299–301, doi:10.1016/0032-0633(66)90129-2.

Dungey, J. W. (1961), Interplanetary magnetic field and the auroral zones, *Phys. Rev. Lett.*, 6, 47.

Ebihara, Y., and T. Tanaka (2015a), Substorm simulation: Insight into the mechanisms of initial brightening, *J. Geophys. Res. Space Physics*, 120, 7270–7288, doi:10.1002/2015JA021516.

Ebihara, Y., and T. Tanaka (2015b), Substorm simulation: Formation of westward traveling surge, *J. Geophys. Res. Space Physics*, 120, 10,466–10,484, doi:10.1002/2015JA021697.

Ebihara, Y., and T. Tanaka (2016), Substorm simulation: Quiet and N-S arcs preceding auroral breakup, *J. Geophys. Res. Space Physics,* 121, 1201–1218, doi:10.1002/2015JA021831.

Ergun, R. E., L. Andersson, D. Main, Y.-J. Su, D. L. Newman, M. V. Goldman, C. W. Carlson, A. J. Hull, J. P. McFadden, and F. S. Moser (2004), Auroral particle acceleration by strong double layers: The upward current region, *J. Geophys. Res.*, 109, A12220, doi:10.1029/2004JA010545.

Ergun, R. E., C. W. Carlson, J. P. McFadden, F. S. Mozer, and R. J. Strangeway (2000), Parallel electric fields in discrete arcs, *Geophys. Res. Lett.*, 27, 4053.

Erlandson, R. E., and L. J. Zanetti (1998), A statistical study of auroral electromagnetic ion cyclotron waves, *J. Geophys. Res.*, 103, 4627.

Evans, D. S. (1967), A 10-cps periodicity in the precipitation of auroral-zone electrons, *J. Geophys. Res.*, 72(17), 4281–4291, doi:10.1029/JZ072i017p04281.

Fisher, G. H., and B. T. Welsch (2008), FLCT: A Fast, Efficient Method for Performing Local Correlation Tracking, *Subsurface and Atmospheric Influences on Solar Activity*, 383, 373–380

Foster, J. C., and H. B. Vo (2002), Average characteristics and activity dependence of the subauroral polarization stream, *J. Geophys. Res.*, 107(A12), 1475, doi:10.1029/2002JA009409.

Frank, L. A., and K. L. Ackerson (1971), Observations of charged particle precipitation into the auroral zone, *J. Geophys. Res.*, 76, 3612.

Fukuda Y., R. Kataoka, Y. Miyoshi, Y. Katoh, T. Nishiyama, K. Shiokawa, Y. Ebihara, D. Hampton, and N. Iwagami (2016), Quasi-periodic rapid motion of pulsating auroras, *Polar Science*, 10, 183–191.

Glassmeier, K.-H., and C. Heppner (1992), Traveling magnetospheric convection twin vortices: Another case study, global characteristics, and a model, *J. Geophys. Res.*, 97(A4), 3977–3992, doi:10.1029/91JA02464.

Goertz, C. K., and R. W. Boswell (1979), Magnetosphere-ionosphere coupling, *J. Geophys. Res.*, 84, 7239.

Grydeland, T., B. Gustavsson, L. Baddeley, J. Lunde, and E. M. Blixt (2008), Conditional integration of Incoherent Scattering in relation to flickering aurora, *J. Geophys. Res.*, 113, A08305, doi:10.1029/2008JA013039.

Gurnett, D. A., and L. A. Frank (1972), ELF noise bands associated with auroral electron precipitation, *J. Geophys. Res.*, 77, 3411.

Gustafsson, G., M. Andre, L. Matson, and H. Koskinen (1990), On waves below the local proton gyrofrequency in auroral acceleration regions, *J. Geophys. Res.*, 95, 5889.

Gustavsson, B., J. Lunde, and E. M. Blixt (2008), Optical observations of flickering aurora and its spatiotemporal characteristics, *J. Geophys. Res.*, 113, A12317, doi:10.1029/2008JA013515.

Hasegawa, A. (1976), Particle acceleration by MHD surface wave and formation of the aurora, *J. Geophys. Res.*, 81, 5083.

Hough, G., M. J. Kosch, and M. J. W. Scourfield (1992), First observations of super fast auroral waves, *Geophys. Res. Lett.*, 12, 2433–2435. doi:10.1029/92GL01110.

Iijima, P., and T. A. Potemra (1976), Field aligned currents in the dayside cusp observed by Triad, *J. Geophys. Res.*, 81, 5971.

Jaynes, A. N., M. R. Lessard, K. Takahashi, A. F. Ali, D. M. Malaspina, R. G. Michell, E. L. Spanswick, D. N. Baker, J. B. Blake, C. Cully, E. F. Donovan, C. A. Kletzing, G. D. Reeves, M. Samara, H. E. Spence, and J. R. Wygant (2015), Correlated Pc4–5 ULF waves, whistler-mode chorus, and pulsating aurora observed by the Van Allen Probes and ground-based systems, *J. Geophys. Res. Space Physics*, 120, 8749–8761, doi:10.1002/2015JA021380.

Kataoka, R., Y. Fukuda, Y. Miyoshi, H. Miyahara, S. Itoya, Y. Ebihara, D. Hampton, H. Dahlgren, D. Whiter, and N. Ivchenko (2015), Compound auroral micromorphology: ground-based high-speed imaging. *Earth, Planets Sp.*, 67, 23. doi:10.1186/s40623-015-0190-6.

Kataoka, R., Y. Fukuda, H. A. Uchida, H. Yamada, Y. Miyoshi, Y. Ebihara, H. Dahlgren, and D. Hampton (2016), High-speed stereoscopy of aurora, *Ann. Geophys.*, 34, 41-44, doi:10.5194/angeo-34-41-2016.

Kataoka, R., Y. Miyoshi, D. Hampton, T. Ishii, and H. Kozako (2012), Pulsating aurora beyond the ultra-low-frequency range, *J. Geophys. Res.*, 117, A08336, doi:10.1029/2012JA017987.

Kataoka, R., Y. Miyoshi, T. Sakanoi, A. Yaegashi, Y. Ebihara, and K. Shiokawa (2011), Ground-based multispectral high-speed imaging of flickering aurora, *Geophys. Res. Lett.*, 38, L14106, doi:10.1029/2011GL048317.

Katoh, Y. (2014), A simulation study of the propagation of whistler-mode chorus in the Earth's inner magnetosphere, *Earth, Planets Sp.*, 66, 6, doi:10.1186/1880-5981-66-6.

Kivelson, M. G., and C. T. Russell (1995), Introduction to space physics, Cambridge university press.

Knight, S. (1973), Parallel electric fields, *Planet. Space Sci.*, 21, 741–750.

Kunitake, M., and T. Oguti (1984), Spatial-temporal characteristics of flickering spots in flickering auroras, *J. Geomagn. Geoelectr.*, 36, 121.

Li, L., J. Cao, and G. Zhou (2005), Combined acceleration of electrons by whistler-mode and compressional ULF turbulences near the geosynchronous orbit, *J. Geophys. Res.*, 110, A03203, doi:10.1029/2004JA010628.

Li, W., R. M. Thorne, J. Bortnik, Y. Nishimura, and V. Angelopoulos (2011), Modulation of whistler mode chorus waves: 1. Role of compressional Pc4–5 pulsations, *J. Geophys. Res.*, 116, A06205, doi:10.1029/2010JA016312.

Li, W., R. M. Thorne, Y. Nishimura, J. Bortnik, V. Angelopoulos, J. P. McFadden, D. E. Larson, J. W. Bonnell, O. Le Contel, A. Roux, and U. Auster (2010), THEMIS analysis of observed equatorial electron distributions responsible for the chorus excitation, *J. Geophys. Res.*, 115, A00F11, doi:10.1029/2009JA014845.

Lin, C. S., and R. A. Hoffman (1979), Fluctuations of the inverted V electron fluxes, *J. Geophys. Res.*, 84, 6547.

Lotko, W. (1986), Diffusive acceleration of auroral primaries, *J. Geophys. Res.*, 91(A1), 191–203, doi:10.1029/JA091iA01p00191.

Lund, E. J., et al. (1995), Observations of electromagnetic oxygen cyclotron waves in a flickering aurora, *Geophys. Res. Lett.*, 22, 2465.

Lund, E. J., and J. LaBelle (1997), On the generation and propagation of auroral electromagnetic ion cyclotron waves, *J. Geophys. Res.*, 102, 17, 241.

Maggs, J. E., and T. N. Davis (1968), Measurements of the thicknesses of auroral structures, *Planet. Space Sci.*, 16, 205.

McFadden, J. P., C. W. Carlson, M. H. Boehm, and T. J. Hallinan (1987), Field-aligned electron flux oscillations that produce flickering aurora, *J. Geophys. Res.*, 92, 11,133.

McFadden, J. P., et al. (1998), Electron modulation and ion cyclotron waves observed by FAST, *Geophys. Res. Lett.*, 25, 2045.

McFadden, J. P., C. W. Carlson, and R. E. Ergun (1999), Microstructure of the auroral acceleration region as observed by FAST, *J. Geophys. Res.*, 104(A7), 14453–14480, doi:10.1029/1998JA900167.

McHarg, M. G., D. L. Hampton, and H. C. Stenbaek-Nielsen (1998), Fast photometry of flickering in discrete auroral arcs, *Geophys. Res. Lett.*, 25, 2637.

Michell, R. G., M. G. McHarg, M. Samara, and D. L. Hampton (2012), Spectral analysis of flickering aurora, *J. Geophys. Res.*, 117, A03321, doi:10.1029/2011JA016703.

Miyoshi, Y., Y. Katoh, T. Nishiyama, T. Sakanoi, K. Asamura, and M. Hirahara (2010), Time of flight analysis of pulsating aurora electrons, considering wave-particle interactions with propagating whistler mode waves, *J. Geophys. Res.*, 115, A10312, doi:10.1029/2009JA015127.

Miyoshi, Y., S. Saito, K. Seki, T. Nishiyama, R. Kataoka, K. Asamura, Y. Katoh, Y. Ebihara, T. Sakanoi, M. Hirahara, S. Oyama, S. Kurita, and O. Santolik (2015), Relation between fine structure of energy spectra for pulsating aurora electrons and frequency spectra of whistler mode chorus waves, *J. Geophys. Res. Space Physics*, 120, 7728–7736, doi:10.1002/2015JA021562.

Morioka, A., Y. Miyoshi, F. Tsuchiya, H. Misawa, T. Sakanoi, K. Yumoto, R. R. Anderson, J. D. Menietti, and E. F. Donovan (2007), Dual structure of auroral acceleration regions at substorm onsets as derived from auroral kilometric radiation spectra, *J. Geophys. Res.*, 112, A06245, doi:10.1029/2006JA012186.

Morooka, M., and T. Mukai (2003), Density as a controlling factor for seasonal and altitudinal variations of the auroral particle acceleration region, *J. Geophys. Res.*, 108(A7), 1306, doi:10.1029/2002JA009786.

Mozer, F. S., C. W. Carlson, R. B. Torbert, B. Parady, J. Yatteau, and M. C. Kelley (1977), Observations of paired electrostatic shocks in the polar magnetosphere, *Phys. Rev. Lett.*, 38, 292.

Nakamura, R., and T. Oguti (1987), Drifts of auroral structures and magnetospheric electric fields, *J. Geophys. Res.*, 92(A10), 11241–11247, doi:10.1029/JA092iA10p11241.

Nishimura, Y, J. Bortnik, W. Li, R. M. Thorne, L. R. Lyons, V. Angelopoulos, S. B. Mende, J. W. Bonnell, O. Le Contel, C. Cully, R. Ergun, and U. Auster (2010), Identifying the driver of pulsating aurora, *Science*, 330, 81–84, doi:10.1126/science.1193186.

Nishiyama, T., Y. Miyoshi, Y. Katoh, T. Sakanoi, R. Kataoka, and S. Okano (2016), Substructures with luminosity modulation and horizontal oscillation in pulsating patch: Principal component analysis application to pulsating aurora, *J. Geophys. Res. Space Physics*, 121, 2360–2373, doi:10.1002/2015JA022288.

Nishiyama, T., T. Sakanoi, Y. Miyoshi, D. L. Hampton, Y. Katoh, R. Kataoka, and S. Okano (2014), Multiscale temporal variations of pulsating auroras: On-off pulsation and a few Hz modulation, *J. Geophys. Res. Space Physics*, 119, 3514–3527, doi:10.1002/2014JA019818.

Nishiyama, T., T. Sakanoi, Y. Miyoshi, Y. Katoh, K. Asamura, S. Okano, and M. Hirahara (2011), The source region and its characteristic of pulsating aurora based on the Reimei observations, *J. Geophys. Res.*, 116, A03226, doi:10.1029/2010JA015507.

Oguti, T (1978), Observations of Rapid Auroral Fluctuations, *J. Geomag. Geoelectr.*, 30, 299-314, doi:10.5636/jgg.30.299.

Omura, Y., J. Pickett, B. Grison, O. Santolik, I. Dandouras, M. Engebretson, P. M. E. Décréau, and A. Masson (2010), Theory and observation of electromagnetic ion cyclotron triggered emissions in the magnetosphere, *J. Geophys. Res.*, 115, A07234, doi:10.1029/2010JA015300.

Paulson, K. V., and G. G. Shepherd (1966), Short-lived brightness oscillations in active auroras, *Can. J. Phys.*, 44, 921–924.

Perkins, F. W. (1968), Plasma-wave instabilities in the ionosphere over the aurora, *J. Geophys. Res.*, 73(21), 6631–6648, doi:10.1029/JA073i021p06631.

Rees, M. H., and D. Luckey (1974), Auroral electron energy derived from ratio of spectroscopic emissions: 1. Model computations, *J. Geophys. Res.*, 79, 5181.

Richmond, A. D., and G. Lu (2000), Upper-atmospheric effects of magnetic storms: A brief tutorial, *J. Atmos. Sol. Terr. Phys.*, 62, 1115–1127.

Royrvik, O., and T. N. Davis (1977), Pulsating aurora: Local and global morphology, *J. Geophys. Res.*, 82(29), 4720–4740, doi:10.1029/JA082i029p04720.

Sakanoi, K., and H. Fukunishi (2004), Temporal and spatial structures of flickering aurora derived from high-speed imaging photometer observations at Syowa Station in the Antarctic, *J. Geophys. Res.*, 109, A01221, doi:10.1029/2003JA010081.

Sakanoi, K., H. Fukunishi, and Y. Kasahara (2005), A possible generation mechanism of temporal and spatial structures of flickering aurora, *J. Geophys. Res.*, 110, A03206, doi:10.1029/2004JA010549.

Sandahl, I., L. Eliasson, and R. Lundin (1980), Rocket observations of precipitating electrons over a pulsating aurora, *Geophys. Res. Lett.*, 7, 309–312, doi: 10.1029/GL007i005p00309.

Santolík, O., D. A. Gurnett, J. S. Pickett, M. Parrot, and N. Cornilleau-Wehrlin (2003), Spatio-temporal structure of storm-time chorus, *J. Geophys. Res.*, 108, 1278, doi:10.1029/2002JA009791, A7.

Sato, N., D. M. Wright, C. W. Carlson, Y. Ebihara, M. Sato, T. Saemundsson, S. Milan, and M. Lester (2004), Generation region of pulsating aurora obtained simultaneously by the FAST satellite and a Syowa-Iceland conjugate pair of observatories, *J. Geophys. Res.*, 109, A10201, doi:10.1029/2004JA010419.

Scourfield, M. W. J., and N. R. Parsons (1971), Television imaging of fast auroral waves, *Planet. Space Sci.*, 19, 437–442, doi:10.1016/0032-0633(71)90159-0.

Semeter, J., and E. M. Blixt (2006), Evidence for Alfvén wave dispersion identified in high-resolution auroral imagery, *Geophys. Res. Lett.*, 33, L13106, doi:10.1029/2006GL026274.

Semeter, J., M. Zettergren, M. Diaz, and S. Mende (2008), Wave dispersion and the discrete aurora: New constraints derived from high-speed imagery, *J. Geophys. Res.*, 113, A12208, doi:10.1029/2008JA013122.

Sheeley, B. W., M. B. Moldwin, H. K. Rassoul, and R. R. Anderson (2001), An empirical plasmasphere and trough density model: CRRES observations, *J. Geophys. Res.*, 106(A11), 25631–25641, doi:10.1029/2000JA000286.

Smith, R.L., and N. Brice (1964), Propagation in multi-component plasmas, *J. Geophys. Res.*, 69, 5029.

Spiger, R. J., and H. R. Anderson (1985), Fluctuations of precipitated electron intensity in flickering auroral arcs, *J. Geophys. Res.*, 90, 6647.

Stasiewicz, K., et al. (2000), Small scale Alfvénic structure in the aurora, *Space Sci. Rev.*, 92, 423.

Stenbaek-Nielsen, H. C., T. J. Hallinan, D. L. Osborne, J. Kimball, C. C. Chaston, J. P. McFadden, G. Delory, M. Temerin, and C. W. Carlson (1998), Aircraft observations conjugate to FAST: Auroral arc thicknesses, *Geophys. Res. Lett.*, 25, 2073.

Stix, T. H. (1992) Waves in Plasmas, *American Institute of Physics*, New York.

Stockwell, R. G., L. Mansinha, and R. P. Lowe (1996), Localization of the complex spectrum: The S transform, *IEEE Trans. Signal Processing*, 44(4), 998–1001, doi:10.1109/78.492555.

田中高史 (2014), サブストームの研究: 第 2 編: 対流の発達によるサブストームの発生, *Antarctic Record*, 58(2), 108-149.

Tanaka, T., A. Nakamizo, A. Yoshikawa, S. Fujita, H. Shinagawa, H. Shimazu, T. Kikuchi, and K. K. Hashimoto (2010), Substorm convection and current system deduced from the global simulation, *J. Geophys. Res.*, 115, A05220, doi:10.1029/2009JA014676.

Temerin, M., C. Carlson, and J. P. McFadden (1993), The acceleration of electrons by electromagnetic ion cyclotron waves, in Auroral Plasma Dynamics, *Geophys. Monogr. Ser.*, 80, 155.

Temerin, M., and R. L. Lysak (1984), Electromagnetic ion cyclotron mode (ELF) waves generated by auroral electron precipitation, *J. Geophys. Res.*, 89, 2849.

Temerin, M., J. McFadden, M. Boehm, C. W. Carlson, and W. Lotko (1986), Production of flickering aurora and field-aligned electron flux by electromagnetic ion cyclotron waves, *J. Geophys. Res.*, 91, 5769–5792.

Torbert, R. B., F. S. Mozer (1978), Electrostatic shocks as the source of discrete auroral arcs, *Geophys. Res. Lett.*, 5, 135.

Trakhtengerts, V. Y., A. G. Demekhov, E. E. Titova, B. V. Kozelov, O. Santolik, D. Gurnett, and M. Parrot (2004), Interpretation of Cluster data on chorus emissions using the backward wave oscillator model, *Phys. Plasmas*, 11, 1345–1351, doi:10.1063/1.1667495.

Tung, Y.-K., G. T. Delory, and C. W. Carlson (2002), Modulation of auroral field-aligned electron fluxes under two inverted-V structures at different altitudes, *Geophys. Res. Lett.*, 29(10), doi:10.1029/2001GL013719.

Turunen, E., P. T. Verronen, A. Seppälä, C. J. Rodger, M. A. Clilverd, J. Tamminen, C. F. Enell, and T. Ulich (2009), Impact of different energies of precipitating particles on NOx generation in the middle and upper atmosphere during geomagnetic storms, *J. Atmos. Sol. Terr. Phys.*, 71, 1176–1189, doi:10.1016/j.jastp.2008.07.005.

Whiter, D. K., B. S. Lanchester, B. Gustavsson, N. Ivchenko, J. M. Sullivan, and H. Dahlgren (2008), Small-scale structures in flickering aurora, *Geophys. Res. Lett.*, 35, L23103, doi:10.1029/2008GL036134.

Whiter, D. K., B. S. Lanchester, B. Gustavsson, N. Ivchenko, and H. Dahlgren (2010), Using multispectral optical observations to identify the acceleration mechanism responsible for flickering aurora, *J. Geophys. Res.*, 115, A12315, doi:10.1029/2010JA015805.

Yaegashi, A., T. Sakanoi, R. Kataoka, K. Asamura, Y. Miyoshi, M. Sato, and S. Okano (2011), Spatial-temporal characteristics of flickering aurora as seen by high-speed EMCCD imaging observations, *J. Geophys. Res.*, 116, A00K04, doi:10.1029/2010JA016333.

Yamamoto, T. (1988), On the temporal fluctuations of pulsating auroral luminosity, *J. Geophys. Res.*, 93(A2), 897–911, doi:10.1029/JA093iA02p00897.

Yamamoto, T., and T. Oguti (1982), Recurrent fast motions of pulsating auroral patches: 1. A case study on optical and quantitative characteristics during a slightly active period, *J. Geophys. Res.*, 87(A9), 7603–7614, doi:10.1029/JA087iA09p07603.